JEOL news
Volume 38 number 1, 2003
ISSN 0385-4426

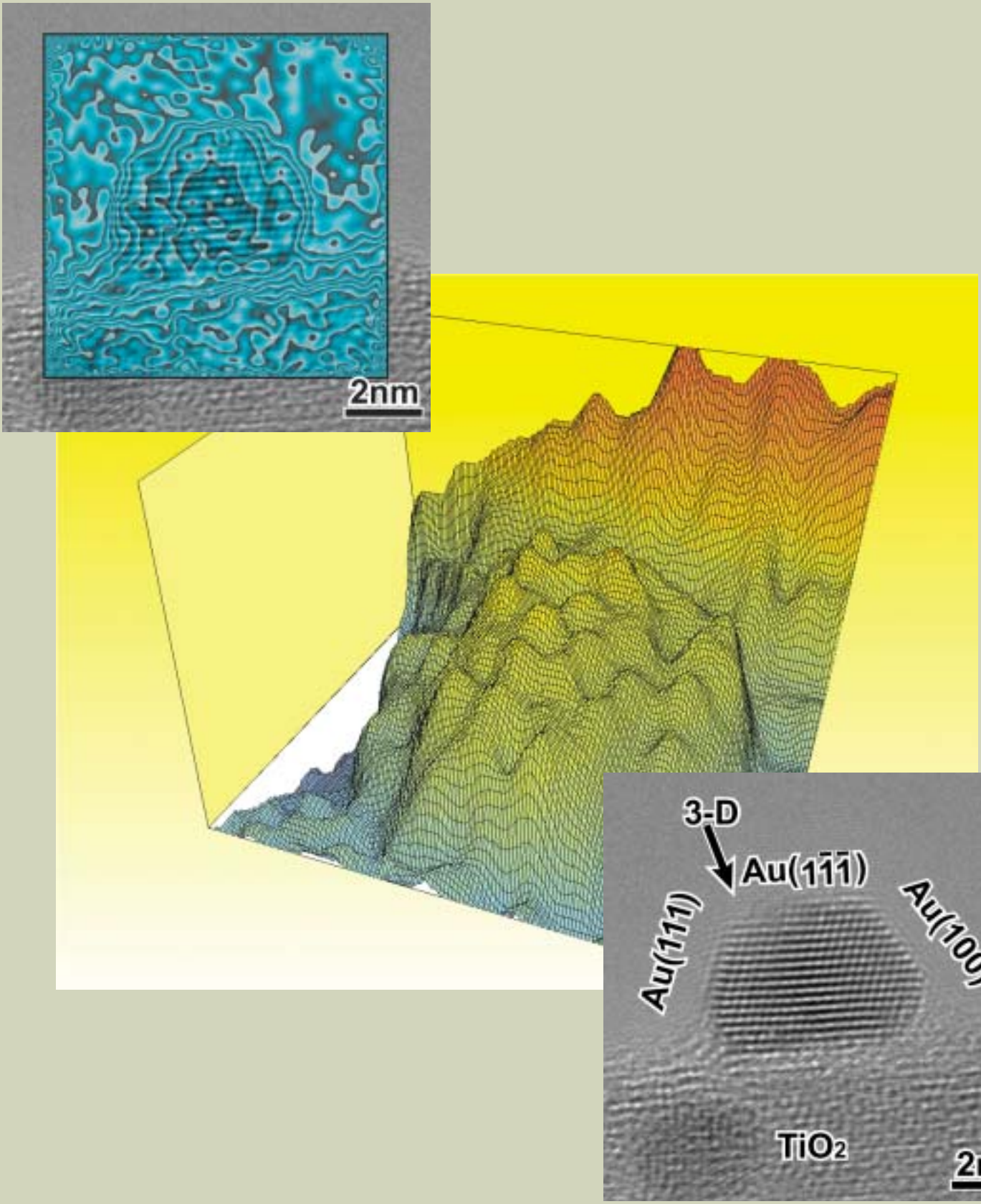

JEOL news

Volume 38 Number 1
Jun 20, 2003

Mapping of sp^2/sp^3 in DLC Thin Film by Signal Processed ESI series Energy Loss Image

Jing-Yi Yan, Fu-Rong Chen and Ji-Jung Kai

Department of Engineering and System Science, National Tsing-Hua University.

A set of signal processing methods consists of FFT interpolation, maximum entropy de-convolution and wavelet transformation has been successfully integrated to improve the quality of the extracted C K-edge spectra from ESI series. FFT interpolation is used to improve the dispersion arising from discrete sampling of ESI series in the energy space. Maximum entropy method is used to dispel convolution effect resulting from the ESI series acquired with finite energy window. Wavelet transformation is applied to de-noise for the extracted ESI spectrum. The post-processed ESI spectrum has quality as good as that of probe-acquired that makes semi-quantitative analysis of 2-dimensional sp^2/sp^3 ratio map in DLC thin film become possible. In general, this method is applicable to reconstruct good quality of core loss EELS spectra from nanometer area, so that 2-dimensional information about electronic structure in materials can possibly be analyzed quantitatively with near nanometer resolution.

Introduction

In the recent years, many techniques for electron energy loss spectrometry (EELS) were proposed to make EELS not only determine the composition of specimen but also analyze the chemical bonding and local electronic structure at sub-nanometer resolution [1-4]. Two kinds of method have been established to acquire the 2-D spectroscopic information. The first technique is called spectrum-image proposed by Jeanguillaume & Colliex in 1989 [3]. The other method is called electron spectroscopic imaging (ESI) or image-spectroscopy which was proposed by Jeanguillaume in 1978 [5] and comprehensively summarized by Reimer in 1995[6]. The ESI method was further developed by many scientists [7-10], which involves building up 2-D spectra from a series of energy loss image at specific area.

These two methods have their own superiorities in terms of acquisition time, spatial resolution and energy resolution. The fundamental difference of these two spectra techniques is that the spectrum-image technique acquires EELS spectrum discretely in the spatial space, while the ESI technique obtains energy loss images discontinuously in the energy space. Neglecting the delocalization effect, the spatial resolution of the spectrum-image depends on the electron probe size and the sampling spacing. For a fixed area, better spatial resolution can be achieved with a finer electron beam and finer sampling spacing by compromising total acquisition time. Until now, the best acquisition time for a 128×64 spectra image (~40×10 nm) with beam size 3Å in low loss region is about 140 seconds [11]. The acquiring time of the ESI technique is dependent on the width of energy window used to collect the energy loss image series. Generally, the typical acquisition time for ESI technique across 100eV in the core loss region is about 100 to 300 seconds with size of 512×512 (~150×150 nm) pixels and a pixel resolution of about 2.5Å.

Generally, ESI method has shorter total acquisition time for wide area with equivalent pixel resolution compared with the focused beam image-spectrum technique [7]. However, these advantages accompany two drawbacks. Generally, energy resolution of spectrum-image is about 0.3eV to 1eV while the energy resolution of extracted ESI spectrum is decided on width of selective energy slit which is typically about 3eV to 20eV [7]. The extracted ESI spectrum is actually a convoluted version of original spectrum, since the integrated intensity within the energy window is used to present intensity of one pixel in the ESI spectrum. Secondly, the extracted ESI spectra are sampled discretely in energy space, such that the

HsinChu, Taiwan 300, Republic of China
E-mail: frchen@msc.nthu.edu.tw

Contents

Cover micrograph

Holographic phase image (top) and 3-D nanostructure (middle) of a gold particle supported on TiO_2, and its HREM image (bottom). (See pages 6 to 9)

Courtesy of Dr.Satoshi Ichikawa, National Institute of Advanced Industrial Science and Technology (AIST Kansai)

dispersion of ESI spectra is usually low. These two drawbacks can be overcome using maximum entropy de-convolution method and FFT interpolation, respectively [12].

Due to lower signal to noise ratio in the core loss region than in the low loss region, application of ESI technique in the core loss region is more difficult. For the core loss analysis, noise is an important component in the spectrum because it always mixes with the real signal in the raw spectrum and it cannot be identified directly. In a FEG/EELS system, the high frequency noise may be caused by instability of the electron source and recording CCD system [13], while the low frequency may contribute from the plural scattering which can be removed using Fourier-log method [10,14]. The presence of the high frequency noise in the spectrum will limit de-convolution process to remove the pulsar scattering and convolution effect from finite energy slit, since the de-convolution process not only improves the signal but also enhances the noise. De-noise process is, therefore very important for reconstructing quantifiable spectra in the core loss region.

There are several methods to reduce noise in the signal. Random noise can be minimized by spatial averaging technique, but slightly degrading energy resolution. For a periodic object used for high resolution TEM imaging, for example, Fourier filter is usually applied to remove the noise, but the artificial signal may be added or the signal is distorted in the edge of spectrum, especially, for a small size of filter window. All of these filters involve transferring the data to the reciprocal space (frequency domain) and removing the noise from the specific frequencies. When using these methods, the basic assumption is that the noise localized in particular frequency domains. However, this assumption is not convenient for EELS spectrum because the noise may be randomly mixed with the signal in any frequency space. The above mentioned methods may be not suitable for EELS spectrum.

Daubechies and Mallat [15, 16] introduced wavelet transformation, which allows decomposing of low frequency signal and high frequency noise. Muto [17] applied wavelet transformation technique to separate efficiently the high frequency noise and low frequency signal which was further introduced for EXELFS analysis without distorting the original signal component. In this article, technique of wavelet transformation is integrated with fast Fourier transformation (FFT) interpolation and maximum entropy de-convolution to restore the quality of the extracted EEL-spectra of C K-edge from a series of ESI images of DLC thin film, so that a two dimensional sp^3/sp^2 ratio map can be possibly analyzed and quantified. A flow chart of signal processing procedures for reconstructing ESI spectra is depicted in the **Fig. 1**. The detail theory and formulation can be found in our publication [18].

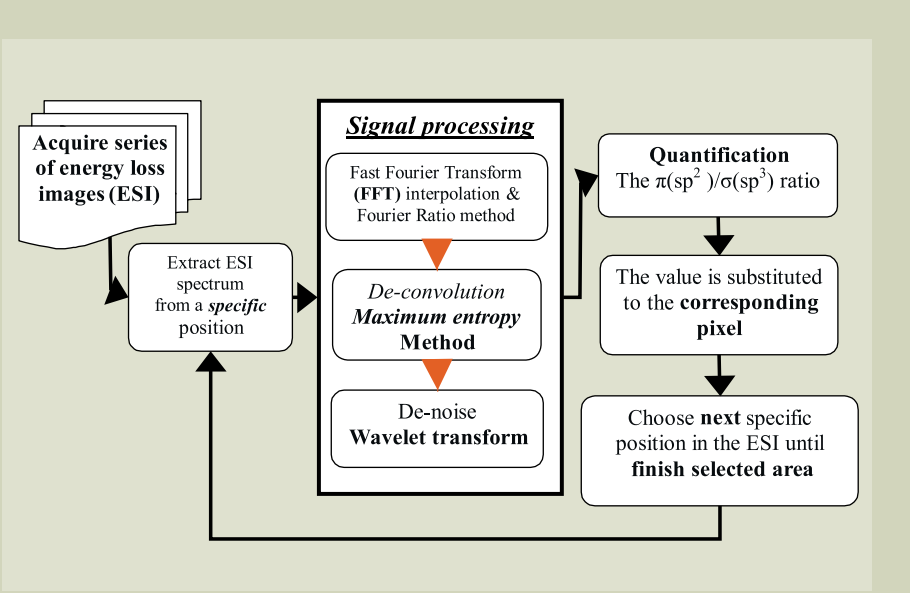

Fig. 1. A flow chart of signal processing procedures for reconstructing ESI spectra and quantify sp^2/sp^3 ratio.

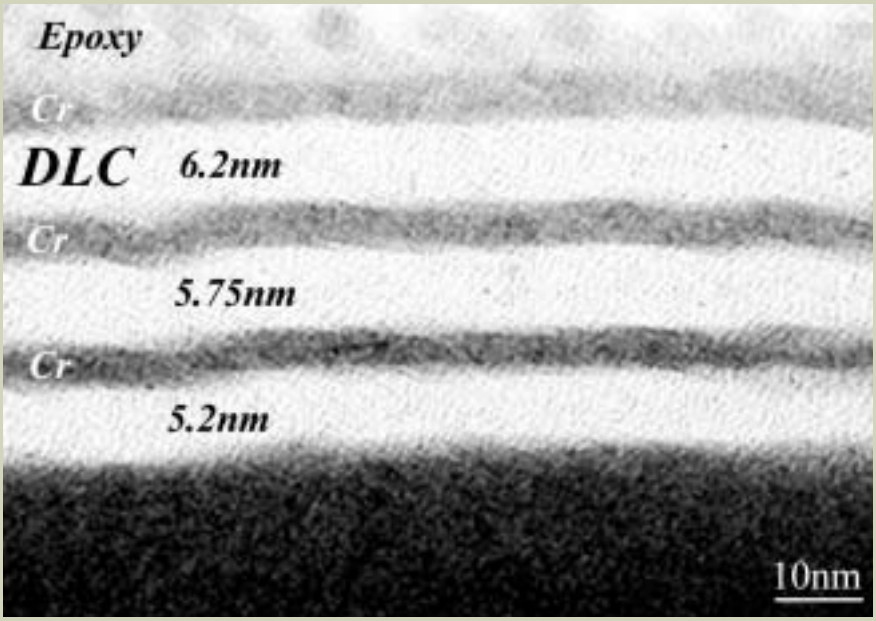

Fig. 2. A bright field image of three layers of amorphous diamond like carbon (a-DLC) films (white contrast) which are separated by the Cr layers (darker contrast). The thickness of a-DLC and Cr layer are 5nm and 2nm, respectively.

Reconstruction of sp^2/sp^3 map from ESI series

Figure 2 shows a bright field image of three layers of amorphous diamond like carbon (a-DLC) films which are separated by the Cr layers. The thicknesses of the a-DLC film and Cr layer are 5 nm and 2 nm, respectively. The morphology of a-DLC layers is seemed smooth and uniform. The ESI series from the energy range of 240 eV to 340 eV were recorded from the same area shown in Fig. 2. The sampling width and the energy width are 2 and 4 eV respectively. The C K-edge has two peaks which corresponds to π^* and σ^* transition local at the 284 eV and 290 eV, respectively. Although the separation of π^* (sp^2) and σ^* (sp^3) edges is 6eV, the signal of π^* and σ^* is still faintly visible. Nevertheless, it is necessary to interpolate the as-extracted spectrum to have a better dispersion in order to obtain better result in the latter de-convolution procedure.

The FFT interpolation is a universal interpolation method which is model independent [12, 18] and very useful for re-sampling for ESI spectra in the core loss region, since the characteristic edges may have no simple mathematical relationship. After the ESI spectra re-sampling with the FFT interpolation method, the maximum entropy and Fourier ratio de-convolution were employed to remove the convolution effect from the selective energy slit and specimen thickness. Then, the de-noise procedure, wavelet transformation, was processed to remove the noise which was enhanced by the de-convolution procedures and is shown in **Fig. 3**.

Fig. 3(a) is the “approximation” component (low frequency component) of a completely processed ESI spectrum under different level (frequency) of wavelet decomposition. Fig. 3(b) shows the corresponding “detail” compo-

nent (noise, the higher frequency component) of the processed ESI spectrum. The "detail" component corresponds to the amount of removed noise froma the original signal. The criterion of the best level for wavelet transformation is given in our publication [18]. The spectrum marked lv2 is best choice in this case due to the fact that it keeps 99.6% of the main characteristic information of the original spectrum without distortion. Comparison among original ESI spectrum, improved ESI spectrum (signal-processed) and probe spectrum which acquired at the same position is shown in the Fig. 3(c). Fig. 3(c) suggests that the improved ESI spectrum has almost the same quality with that of the probe spectrum even in the ELNES region. Although, there is minor difference in the intensity between probe-acquired and the processed ESI spectrum in the higher energy loss region, it can be due to the fact that they are obtained from area of different thickness and with different convergent angle. After reconstructing the ESI spectra, the quantification of sp^2/sp^3 ration of carbon k edge spectrum can be calculated. The quantification of sp^2/sp^3 ratio method was developed by many scientists [19-23] in the last ten years. In this experiment, the EELS spectrum acquired from polygraphite with magic angle [23, 24] is used as standard to quantify the sp^2 fraction in the DLC thin film. The Gaussian distribution model is employed to fitting the content of $\pi^*$and σ^* bonding. After calculating the ratio of the π^* and σ^* bonding from the reconstructed spectra (512×512 pixels), a two-dimensional sp^2 fraction distribution map is shown in **Fig. 4**. The variation of sp^2 fraction is from 15 to 80%. It is evident that ESI image contains more extra information than a bright field TEM image. It is found that the middle of DLC film contains higher sp^3 fraction, while lower sp^3 fraction usually observed in the Cr/a-carbon interface. The thickness in the low sp^2 region is estimated to be about 0.5 to 1 nm in width. This may be due to preferential nucleation and catalytic growth of the graphite-like structure in the C/Cr interface in the beginning of sputtering process [22]. The sp^2 bonding in amorphous

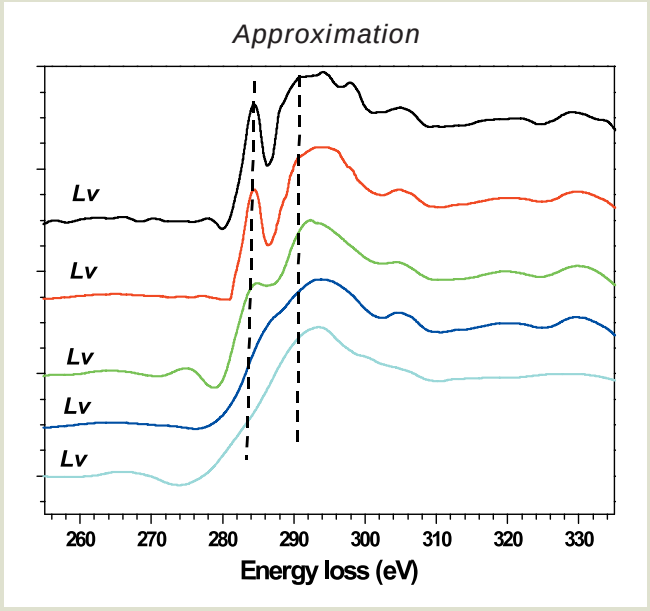

(a)

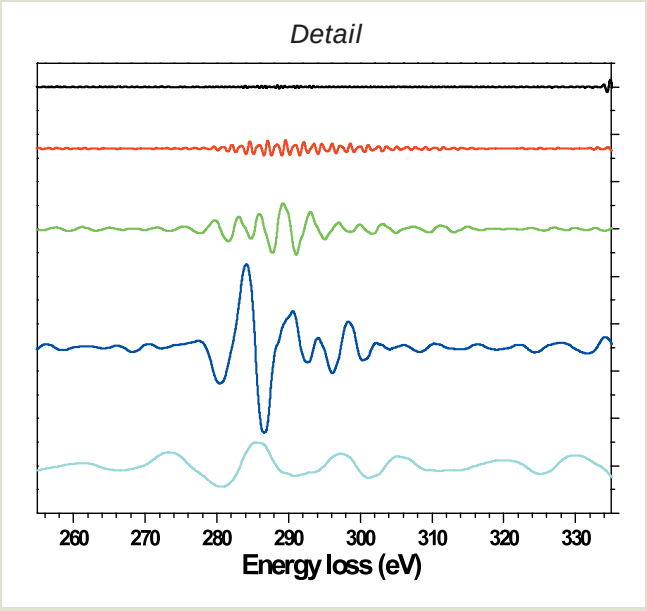

(b)

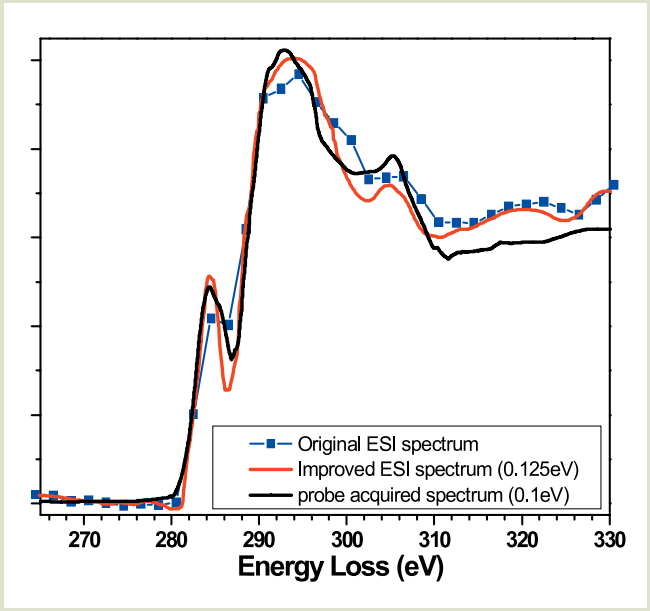

(c)

Fig. 3. (a) The "approximation" component of a completely processed ESI spectrum under different level of wavelet decomposition.
(b) shows the corresponding "detail" component of the processed ESI spectrum.
(c) Comparing the original ESI spectrum, improved ESI spectrum and probe acquired spectrum at the same position.

DLC film could convert to sp^3 bonding or it may be etched away in the later processes by introduction of energetic ions and hydrogen gas. The compress stress could further build up in the later stage of DLC film growth which is also an important factor to promote a transition of sp^2 to sp^3 [23]. This is consistent with previous reports that the most of a-DLC layer has high sp^3 fraction [21-23]. As soon as the sputtering process stops, the surface carbon atoms have the dangling bond which has higher surface energy. For reducing the surface energy, the dangling bond may convert back to character of sp^2 bond.

Conclusion

A set of signal processing methods consists of FFT interpolation, maximum entropy deconvolution and wavelet transformation has been successfully integrated to improve the equality of the extracted spectrum from ESI series. The processed ESI spectra have quality as good as those of a probe-acquired and it even matches with the main characters of near edge fine structure of a C K-edge. This integrated method has been used to semi-quantitatively analyze the sp^3/sp^2 ratio in DLC thin film which acts as a protection layer for the hard disk. This method is applicable to record good quality of 2-dimensional core loss EELS spectra with good spatial resolution, so that electronic structure of materials can possibly be analyzed quantitatively with spatial resolution of near nanometer scale.

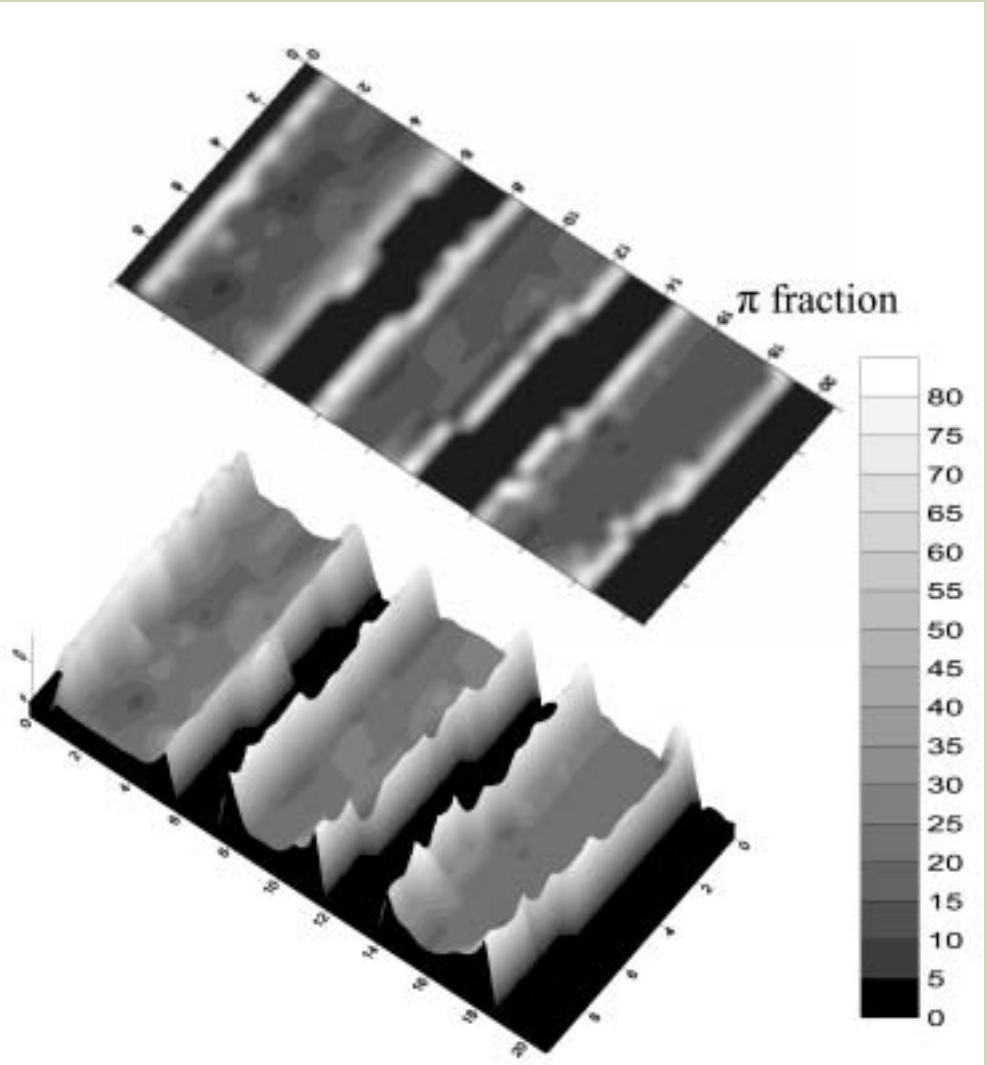

Fig. 4. sp^2/sp^3 map from the same area of Fig. 2. The height is proportional to the ratio of sp^2/sp^3. This map is projected to be a 2-dimensional contour which is displayed on the top of map. The ratio of sp^2/sp^3 is shown in terms of grey color in the contour map.

Acknowledgments

The specimens are prepared by *TRACE storage technology Corp.*. The authors acknowledge form (NSC 90-2216-E-007-053) and (NSC 91-2216-E-007-041)

Reference

1. P. E. Baston, *Phys. Rev. B.* **48**, 2608 (1993)
2. H. Kurata and C. Colliex, *Phys. Rev. B.* **48**, 2101 (1993)
3. C. Jeanguillaume and C. Colliex, *Ultramicroscopy*. **78**, 252 (1989)
4. A. M. David, T. Yujiun, R. Rishi and J. Silcox, Nature, **366**, 725 (1993)
5. C. Jeanguillaume, P. Trebbia and C. Colliex, *Ultramicroscopy*, **3**, 237 (1978)
6. L. Reimer, *Energy-filtering transmission electron microscopy*, Springer-Verlag, NY (1995)
7. J. Mayer and J. M. Plitzko, *J. Microsc*, **183**, 2 (1996)
8. J. M. Martin, B. Vacher, L. Ponsonnet and V. Dupuis, *Ultramicroscopy*, **65**, 229 (1996)
9. J. Mayer, U. Eigenthaler, J. M. Plitzko and F. Dettenwanger, *Micron.* **28**, 361 (1997)
10. P. J. Thomas and P. A. Midgley, *Ultramicroscopy*, **88**, 187 (2001)
11. K. Suenage, M. Tence, C. Mory, C. Collies, H. Kato, T. Okazaki, H. Shinohrar, K. Hiraahara, S. Bandow and S. Iijima, Science, **290**, 2280 (2000)
12. S. C. Lo, J. J. Kai, F. R. Chen, L.C. Chen, L. Chang, C. C. Chiang, P. Ding, B. Chin, H. Zhang and F. Chen (2002) *J. elec. Microsc*, **50**(6), 497 (2000)
13. V. J. Keast, A. J. Scott, R. Brydson, D. B. Williams and J. Brulley, *J. Microsc*, **203**, 135 (2001)
14. R. F. Egerton, *Electron-energy loss spectroscopy in the electron microscopy*, Plenum Press, NY (1996)
15. I. Daubehies, Comm. *Pure Appl. Math*, **41**, 909 (1988)
16. S. Mallat, *IEEE. Trans. Pattern Anal. and Machine Intell*, **11**, 674 (1989)
17. S. Muto, *J. Elec. Microsc*, **49**(4), 525 (2000)
18. J. Y. Yan, F. R. Chen and J. J. Kai, *J. Elec. Microsc*., **51**(6), 391 (2002)
19. J. Robertson, *Surf & Coat Tech*, **50**, 185 (1992)
20. S. D. Berger, D. R. Mckenzie, *Philos. Mag. Lett*. **57**, 285 (1988)
21. A. J. Papworth, C. J. Kiely, A. P. Burden, S. R. P. Silva and G. A. J. Amaratunga, *Phys. Rev. B*, **62**, 12628 (2000)
22. C. A. Davis, G. A. J. Amaratunga and K. M. Knowles, *Phys. Rev. Lett*. **80**, 3280 (1998)
23. A. C. Ferrari, B. K. Tanner, V. Stolojan, L. M. Brown, S. E. Rodil, B. Kleinsorge and J. Robertson, *Phys. Rev. B.* **62**, 11089 (2000)
24. N. K. Menon and J. Yuan, *Ultramicrosopy*., **74**, 83-94 (1998)

Electron Holographic Analysis of Nanostructured Gold Catalyst

S. Ichikawa[†], T. Akita[†], M. Okumura[††], M. Kohyama[†], and K. Tanaka[†]

[†]National Institute of Advanced Industrial Science and Technology (AIST Kansai)
[††]School of Science, Osaka University

The catalytic properties of nanostructured gold catalysts are known to depend on the size of the gold particles and to be activated when the size decreases to a few nanometers. We investigated the size dependence of the three-dimensional (3-D) nanostructure on the mean inner potential of gold catalysts supported on TiO_2 using electron holography and high-resolution electron microscopy (HREM). The contact angle of the gold particles on the titanium oxide supports tended to be >90° for gold particles with a size of >5 nm, and <90° for a size of <2 nm. This decreasing change in the contact angle (morphology) acts to increase the perimeter and hence the area of the interface between gold particles and TiO_2 oxide supports, which is considered to be an active site. The mean inner potential of gold particles also changed as their size decreased. The value of the inner potential of gold, which is ~25 V in bulk state, rose to >40 V when the size of the gold particles was <2 nm. This phenomenon indicates the existence of a charge transfer at the interface between gold and TiO_2. The 3-D structure change and the inner potential change should be attributed to the specific electronic structure at the interface, owing to both the "nano size effect" and the "hetero-interface effect."

Introduction

Gold has been known as one of the most chemically stable elements from the earliest time. The properties of gold are well-known in bulk, but tend to change at nanometer size. Gold catalyst is a typical case. Catalytic properties of gold catalysts depend on the size of gold particles supported on certain oxides, in particular the particle diameter. Gold shows high activity as a catalyst when the particle size decreases down to 5–10 nm [1], although it is inert in bulk. The catalytic property becomes more active, as the size is <5 nm [1]. Furthermore, it is reported that characteristics change suddenly to exhibit platinum-like behavior when the mean diameter is <2 nm [1].

With regard to the microstructure of metal catalysts supported on oxides, the particle size distribution has been investigated using only high-resolution electron microscopy (HREM) [2] up to now. However, many problems must be overcome in order to elucidate the relationship between the catalytic mechanism and the atomic and electronic structure. When the contact angle at the interface between the particle and the support varies without a change of the particle size, both the perimeter which is considered to be one of the important reaction sites [1], and the area of the interface change. Hence it is necessary to reconsider the parameter of "particle size" on the basis of the three-dimensional (3-D) nanostructure in the vicinity of the interface.

When a potential exists in the path of an electron beam, the phase of the electron wave varies in proportion to the distance of the potential that the beam passes through. With a specimen without an electric or a magnetic field, the electron wave is affected by the mean inner potential, i.e. the thickness of the specimen. The conventional transmission electron microscopy (TEM) methods use only the information on the amplitude component of an electron beam, and mostly neglect the information on the phase change by the mean inner potential. However, the phase shift can be recorded in a hologram by electron holography and the phase image reconstructed using the interference of the electron wave. This provides the thickness information that is difficult to obtain using the HREM technique. Thus 3-D nanostructural information can be obtained at atomic scale combing electron holography and HREM.

In this paper we report on the size dependence of the particle morphology and the mean inner potential of the gold catalyst supported on TiO_2 powder, using electron holography and HREM.

Experiment

A powder of Au/TiO_2 catalyst was prepared using the deposition precipitation (DP) method [3] from an aqueous solution of $HAuCl_4$ and TiO_2 powder P-25 that consisted of 25% rutile and 75% anatase. The weight ratio of gold was 1 wt %. With highly dispersed gold particles, the powder of Au/TiO_2 support was calcined in air at 473 K or 673 K for 1 h. The Au/TiO_2 powder was then dispersed in ethanol, and supported on a copper micro-grid mesh. After the drying process, the specimen was ready for observation.

Holograms and HREM images were acquired using a JEOL JEM-3000F with Schottky field emission gun operated at 300 kV and a JEOL EM-30170 biprism unit. The biprism voltage was 130–150 V, which give fringes at 0.85–1.0 nm intervals at magnifications of ×600 K to ×1 M. The phase images were digitally reconstructed from obtained holograms using JEOL HIPS software.

Results

The mean diameter of gold particles in Au/TiO_2 catalyst calcined at 473 K and 673 K was 2.6 nm and 4.2 nm respectively [2]. The results of observing two typical gold particles, one a large particle with a diameter ~5 nm (calcined at 673 K) and the other a small particle with a diameter <2 nm (calcined at 473 K), are described below.

The images of the 5 nm gold particle supported on TiO_2 are shown in **Fig. 1**. The incident beam direction was the <110> zone axis. Figure 1(a) is a HREM image, and Fig. 1(b) is the reconstructed phase image amplified 30 times then superimposed on the HREM image. Contour lines that indicate equal thickness appear across the particle. Since the thickest part of the gold particle is surrounded by a center contour line that is typical to an

[†]1-8-31 Midorigaoka, Ikeda, Osaka, 563-8577, Japan,
E-mail : s.ichikawa@aist.go.jp

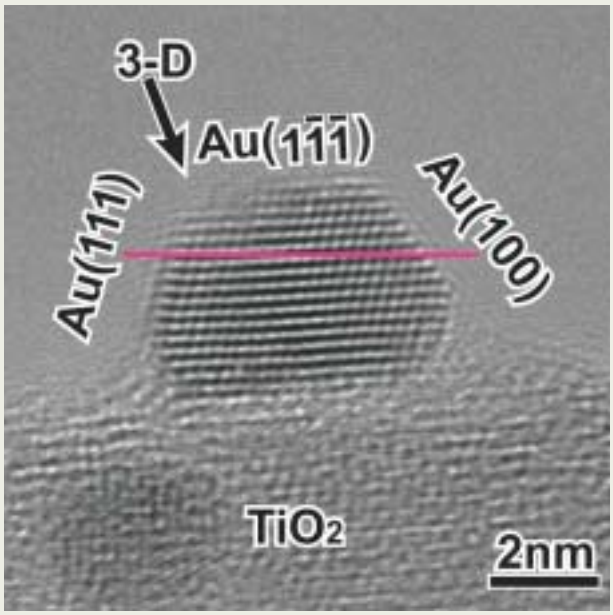

(a)

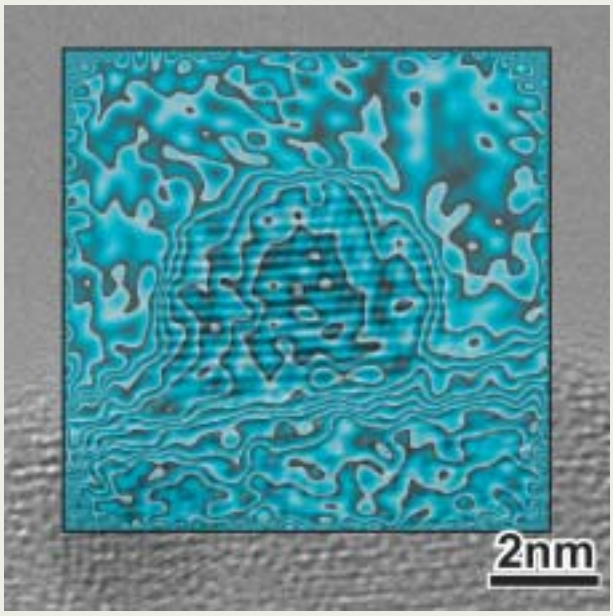

(b)

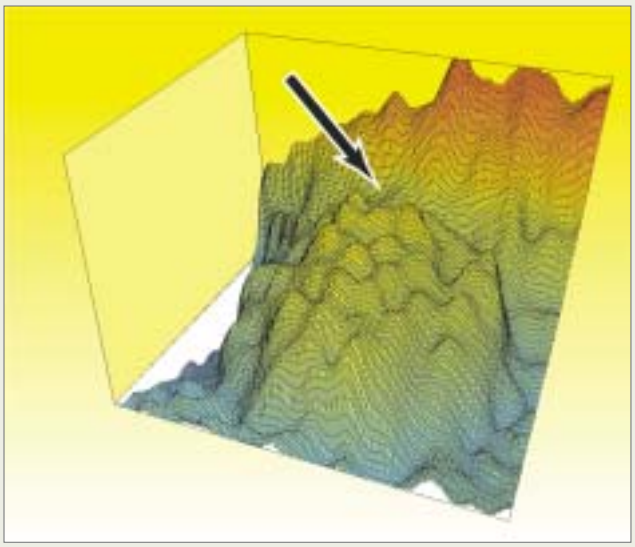

(c)

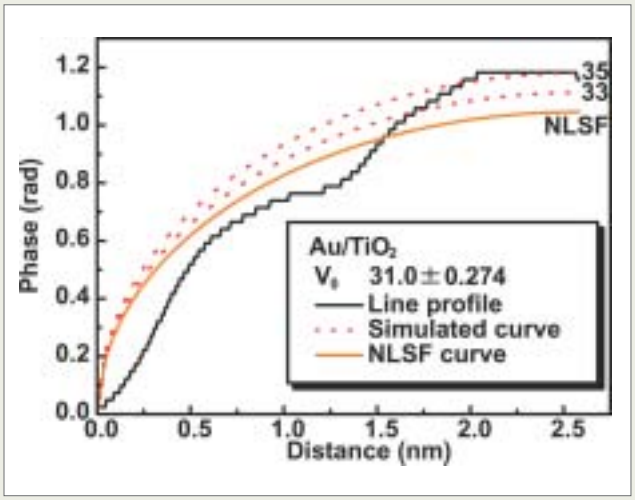

(d)

Fig. 1. The HREM image (a) and the phase image (b) reconstructed from the hologram of the Au/TiO_2 catalyst with a size ~5 nm. The phase image (b) was amplified ×30 and overlapped on the HREM image (a). (c) shows a 3-D wire frame viewed from the arrow in the HREM image (a). (d) shows the line profile of the phase shift along the line in the HREM image (a) and the fitting curve using the sphere approximation (dotted curve).

island structure (the arrow in Fig. 1(b)), it is considered thicker than the region near the interface between gold and TiO_2. Figure 1(c) shows a 3-D wire frame viewed from the arrow in Fig. 1(a) where the height of this 3-D image corresponds with the phase shift of phase image. It reveals that the interfacial region is obviously concave (the arrow in Fig. 1(c)). Hence in this case the contact angle between the gold particle and the TiO_2 support is >90º.

Figure 1(d) shows the line profile and its fitting curve in the phase image (Fig. 1(b)) along the black line in the HREM image (Fig. 1(a)). The shape of the section is a circle on the assumption that the shape of this gold particle is a sphere. The profile was fitted by nonlinear least square method using a semicircle function with the mean inner potential as a parameter. The solid line is the fitted curve and the dotted lines are simulated curves. As a result, the mean inner potential of the gold particles was estimated to be ~31 V.

Figure 2 shows the images of a gold particle that is 1.6 nm in height from the interface. The incident beam direction was also the <110> zone axis. Fig. 2(a) and (b) are a HREM image and a phase image amplified 30 times then superimposed on the HREM image respectively. The diameter of the particle is ~2.5 nm and different from its height in the HREM image for this particle. The shapes of the contour lines differ from Fig. 1. Since they protrude from the interface and do not form an island shape, the thickness of this particle increases as the distance from the interface decreases. In the central part of the particle, the contour lines appear along the [001] plane at almost regular intervals. Considering the characteristics of the contour lines in the phase image and the analysis of the interplanar angles and spacing in the HREM image, the 3-D shape of the gold particle is assumed to be the top half of a truncated octahedron as shown in Fig. 2(c). The truncated octahedron (Fig. 2(c)) is known as a polyhedron with minimum surface energy in a

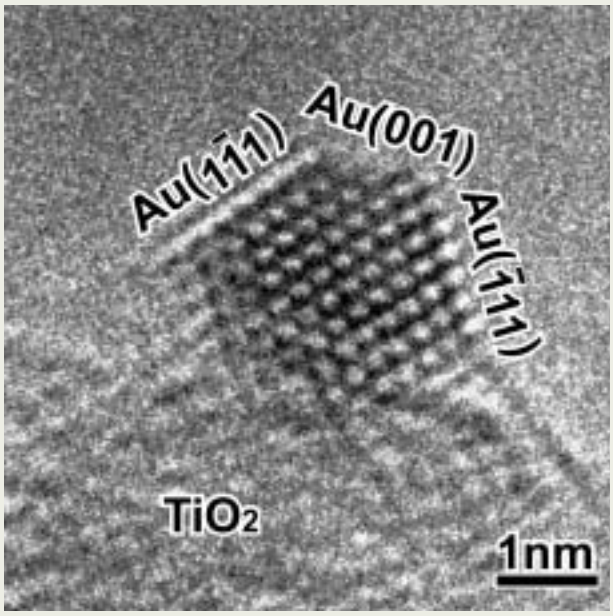

(a)

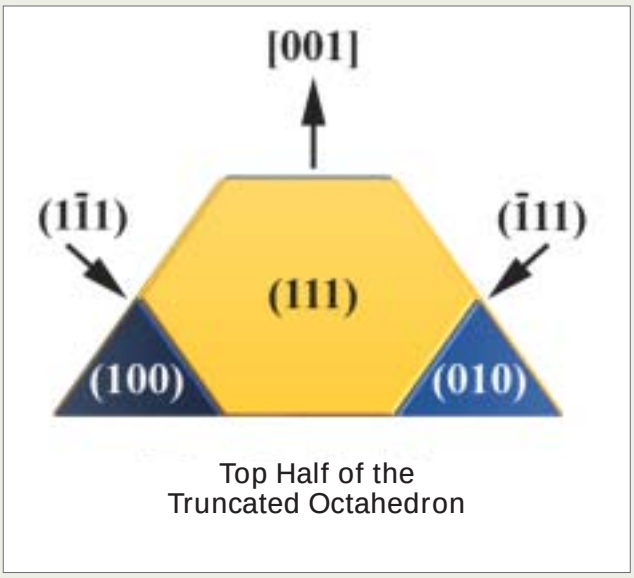

(c)

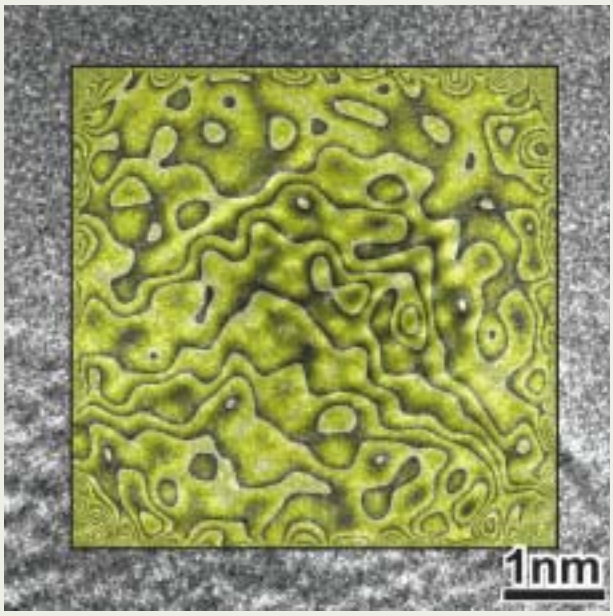

(b)

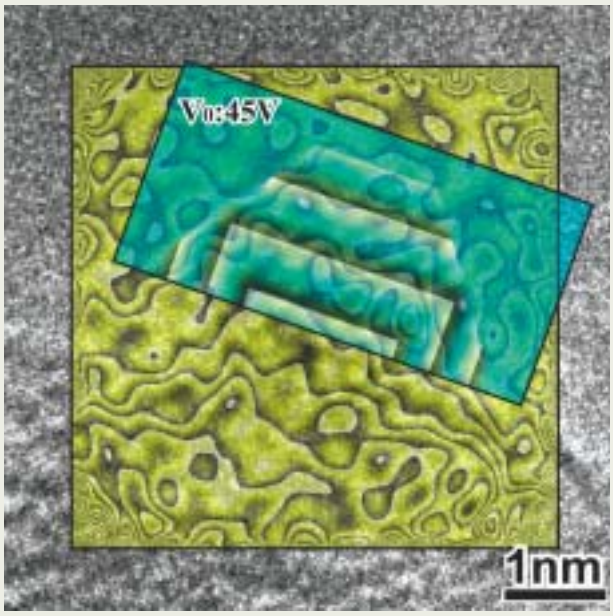

(d)

Fig. 2. The HREM image (a) and the phase image (b) reconstructed from the hologram of the Au/TiO_2 catalyst with a size <2 nm. The phase image (b) was amplified ×30 and overlapped on the HREM image (a). (c) is the schematic 3-D illustration of the top half of a truncated octahedron model. (d) is the simulated phase image of a truncated octahedron model superimposed on the reconstructed phase image (b) when the mean inner potential of gold is 45 V.

face-centered cubic (FCC) structure.

The phase image of the 3-D model was simulated using the top half truncated octahedron model shown in Fig. 2(c) and the mean inner potential V_0 as a parameter. Figure 2(d) shows the simulated image superimposed on the HREM image (Fig. 2(c)). The contour line interval varies with the mean inner potential V_0. Comparing with the simulated image, the reconstructed phase image shows the same characteristic as the top half of the truncated octahedron model in that the contour lines appear in parallel with the (001) planes at regular intervals. This confirms that the gold particle has the shape of the top half of an octahedron and that the contact angle at the interface is <90º. This in turn means that the perimeter of gold per unit volume at the interface with the support for this particle is longer than that of the particle for which the contact angle is >90º with the same diameter.

The intervals of the contour lines parallel with (001) planes were optimized by changing V_0. The simulated image was in good agreement with the reconstructed image when the potential V_0 was 45 V, a value significantly higher than the 31 V of the gold particle with the size of 5 nm.

The relationship between the particle size of gold and the mean inner potential, which measured by the 3-D model simulation and the sphere approximation for line profile, is shown in **Fig. 3**. When the size of gold supported on TiO_2 is <5 nm, and the gold is supported on active carbon, which is considered to have very weak interaction with gold and to have low catalytic activity, the mean inner potential of gold is the same as the experimental value of bulk (21–23 V) [4-6] and the calculated value of bulk (25–30 V) [7]. On the other hand, when gold is supported on TiO_2 with the size <5 nm, the mean inner potential tends to begin increasing, and furthermore tends to increase suddenly with the size <~2 nm. This increasing tendency of the gold inner potential agrees with

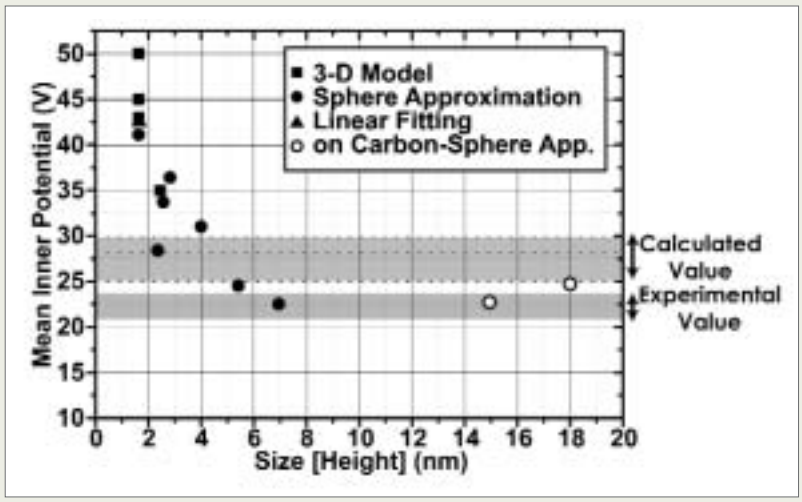

Fig. 3. The relationship between the size of gold particles and the mean inner potential.

the size dependence on the gold catalytic property.

Discussion

According to the report on the orientation relationship between gold and TiO_2 [8], it is frequently observed in both rutile and anatase TiO_2 that the {111} plane of gold is parallel to the interface between gold and TiO_2, and that this orientation relationship has good lattice matching for the anatase type. The index of gold interfacial plane in Fig. 1 is the {111} plane and that in Fig. 2 is the {100} plane. In the case of a large particle (Fig. 1), the contact angle is >90º in spite of good lattice matching. This means that the volume ratio of the atoms located on the interface shrinks during the grain growth due to the effect of minimizing the interfacial energy. It is considered that the interaction such as the charge transfer at the interface is small. Conversely, the 3-D shape near the Au/TiO_2 interface tends to enlarge the volume ratio of the atoms located on the interface in the small particle. This suggests that some interaction at the interface exists aside from the lattice matching.

The perimeter increases as the interfacial shape changes toward enlarging the area at the interface. The perimeter of the top half of the truncated octahedron (Fig. 2(c)) is ~2.4 times longer than that of the "perfect" truncated octahedron with respect to the model with the {100} plane parallel to the interface, i.e. the ratio of the perimeter length per unit volume is ~4.8. Hence the increase in the reaction site due to not only the decrease in the particle size but also the morphology change that occurred when the diameter became <2 nm is one of the most important reasons for the increase in turn-over frequency (TOF), that is the rate of reaction per surface atom, from the gold catalyst <5 nm in diameter.

For the top half octahedron model (Fig. 2(c)) of the gold particle <2 nm in size, the atomic ratio that has the same neighbor atomic configuration as in FCC bulk crystal is only 50% assuming that the other 50% of the atoms are located on the surface and at the interface. Hence the small gold particle is most likely affected by the surface and the interface, and it is considered that the mean inner potential increase is due to the local electronic structure at the interface between the gold and the TiO_2.

The mean inner potential in transition metal elements tends to depend on the electron configuration, especially the outer valence electrons [9], and depends on the number of 3d electrons in case of IV period atoms in the periodic table [10]. The potentials of gold, platinum, and iridium are calculated to be 28.20 V, 32.14 V, and 37.24 V using non-binding approximation and Radi's atomic scattering factor [7, 11]. The measured inner potential of a gold small particle is >40 V, which it is closer to platinum or iridium rather than gold bulk. It is considered that the gold small particle is positively charged if electrons transfer from gold to TiO_2 at the interface, and this changes the electronic structure of the whole gold particle to an electronic structure like platinum or iridium. The same results assuming the charge transfer at the Au/TiO_2 interface and the change of electronic structure were also reported from experiments using XPS [12], EXAFS [13], and TEM [13], and our results support them.

The electron holographic technique used in conjunction with HREM enabled the determination of the electronic structure change directly at nanometer scale. Details of the mean inner potential increase in gold catalyst ware clarified by the work function analysis using a scanning probe microscopy and by the simulation of the electronic structure at the interface using first-principles calculation.

Conclusions

The 3-D structure of gold supported on TiO_2 was analyzed by electron holography and HREM. For gold particles with a height <2 nm from the interface, the contact angle of gold particles on TiO_2 tended to be <90º, and tended to be >90º for those >5 nm. A change in the morphology occurred that increased the volume ratio of the atoms located on the interface and at the perimeter as the particle size decreased.

The mean inner potential of gold depends on the particle size. For gold particles with a height <2 nm, the potential increases suddenly to >40 V.

The electron holographic technique enables the analysis of 3-D structures at atomic scale, and the detection of changes in electronic structure. It has been found to be effective in the analysis of nanostructured particles.

Acknowledgement

The present study is supported by the Cooperative System for Supporting Priority Research, Japan Science and Technology Corporation.

References

1. M. Haruta, *Catal. Today* **36**, 153–166, (1997).
2. T. Akita, P. Lu, S. Ichikawa, K. Tanaka, and M. Haruta, *Surf. Interf. Anal.* **31**, 73–78, (2001).
3. S. Tsubota, D. A. H. Cunningham, Y. Bando, and M. Haruta, in Scientific Bases for Preparation of Heterogeneous Catalysts edited by G. Poncelet et al. (Elsevier Science, New York, 1995), pp. 227–235.
4. R. Buhl, *Zeitschrift für Physik* **155**, 395–412, (1959).
5. M. Keller, *Zeitschrift für Physik* **164**, 274–291, (1961).
6. Y. C. Wang, T. M. Chou, and M. Libera, presented at *Microscopy Society of America meeting* 1997, Cleveland, OH, 1997.
7. M. Gajdardziska-Jpsifovska and A H. Carim, in *Introduction to Electron Holography* edited by E. Völkl, L. F. Allard and D. C. Joy (Kluwer Academic / Plenum Publishers, New York, 1999), pp. 267–293.
8. T. Akita, K. Tanaka, S. Tsubota, and M. Haruta, *J. Electron Microscopy* **49**, 657–662, (2000).
9. J. C. H. Spence, *Acta Cryst.* **A49**, 231–260, (1993).
10. S. Ichikawa, K. Okazaki, T. Akita, M. Okumura, K. Tanaka, and M. Kohyama, Mat. Res. Soc. Symp. Proc. **738**, G13.11, (2003).
11. G. Radi, *Acta Cryst.* **A26**, 41–56, (1970).
12. M. Haruta, S. Tsubota, T. Kobayashi, M. Kageyama, M. J. Genet, and B. Delmon, *J. Catal.* **144**, 175–192, (1993).
13. K. Tanaka, T. Hayashi, and M. Haruta, *J. Japan Inst.* Metals **60**, 693–694, (1996).

Single Atomic Column Observation in Silicon Boundary

Hidetaka Sawada[†], Hideki Ichinose[†] and Masanori Kohyama[††]

[†]**Department of Materials Science, The University of Tokyo**
[††]**Special Division of Green Life Technology, National Institute of Advanced Industrial Science and Technology**

Atomic resolution high voltage transmission electron microscopy (ARHVTEM) was applied on the atomic structure investigations of {112} Σ3 CSL grain boundary of silicon. A single atomic column in the grain boundary was imaged as a circular spot. Atomic structure of the {112} Σ3 CSL grain boundary was directly shown from the obtained image. Electronic structure of the boundary was investigated by ab-initio calculation.

Introduction

Since atomic structure observation of a Σ11 coincidence site lattice (CSL) boundary of gold in 1981 [1] was firstly observed, vast number of grain boundaries and crystal interfaces of various kinds of material, namely iron [1], silicon [2,3], germanium [4] and ceramics [5] were analyzed employing high-resolution transmission electron microscope (HRTEM) lattice imaging. In particular, unique reconstruction manner of the boundary attracted a large number of HRTEM researches [6 to 10]. Recently, electronic property is keenly interested especially in the covalently bonded materials [11 to 14]. However, atomic structure is not yet fully identified experimentally. The identification of the single atomic column, introduced in the structure models [14, 15], is one of most important task to solve the problem. Trouble is that an ordinary lattice image does not show precise atomic position. Simple periodic information on a lattice image cannot cope with this grain boundary structure analysis. Highly developed recent interface science requires more precise atomic structure information that is hardly obtained by an ordinary lattice imaging of HRTEM. In the present paper, the atomic structure of the {112} Σ3 CSL boundary of silicon is analyzed. The superb ability of our atomic resolution high voltage electron microscope (ARHVTEM) [16] is employed to investigate individual atomic site of the grain boundary.

Methods

A high purity polycrystalline silicon film was produced by the reduction method of trichlorosilane using hydrogen (purity: 99.999999999%). The film was sliced, polished and Ar ion milled. Spherical and chromatic aberration coefficients of the employed JEM-ARM1250 atomic resolution high voltage transmission electron microscope are respectively Cs = 1.4 mm, Cc = 2.5 mm. The experimentally certified resolution of this microscope is 0.1 nm at the Scherzer defocus [16].

[†]7-3-1 Hongo, Bunkyo-ku, Tokyo 113-8656, Japan
E-mail: hsawada@jeol.co.jp
He now works for JEOL Ltd.

Ab-initio calculation

Multi-slice image simulation was employed with ab-initio calculation to help accurate image analysis. An atomic configuration was firstly obtained from the micrograph. Secondary, 96-atoms super cell was constructed following the experimentally obtained atomic configuration. Hamann-Schlueter-Chiang (HSC) optimized pseudo potential ($3s^2 3p^{0.5} 3d^{0.5}$) was produced. Starting with the obtained atomic configuration, the ab-initio molecular dynamics calculation was performed to relax the structure using a plane-wave pseudo potential method based on the density-functional theory with a plane-wave cutoff energy of 25 Ry and four special k points per irreducible forth of the Brillouine zone. Then the multi-slice image calculation was carried out on this structure. The calculated image was compared with the image.

Result

{111} Σ3 and {221} Σ9 boundary

A Σ3 CSL grain boundary, being parallel to {111} plane (noted as {111} Σ3CSL boundary), is shown in **Fig. 1 (a)**. Uniform image contrast in the picture shows that an electron beam was well oriented to be parallel to <110> axis of the both crystal. Good matching of the magnified image in **Fig. 1 (b)** to the geometrical structure model that was established in silicon shows that atomic structure of the boundary is well identified by ARHVTEM observation. A high-resolution image of a {221} Σ9 CSL grain boundary is shown in **Fig. 1 (c)**. A magnified image of the boundary is shown in **Fig. 1 (d)** and each round rectangular spots were identified as silicon-silicon dumbbell. The every atomic site in the boundary was described by dumbbell structure. The observed structure consisted of 5-membered ring and 7-membered ring unit and was as the same structure as observed in silicon [3]. It shows that ARHVTEM observation enables us to investigate the distorted atomic structure in the grain boundary.

{112} Σ3 boundary

A wide view of a {112} Σ3 CSL grain boundary is shown in **Fig. 2 (a)**. Periodic structure is apparent in the boundary (**Fig. 2 (b)**). A unit structure of the boundary is magnified in **Fig. 2 (c)**. There were three different kinds of dark spots in the grain boundary. They were two types of rod shape spots and small round spots. The rod shape spots in the both side crystals oriented in <001> direction in each component crystal. However, in the grain boundary, central two spots in a periodic unit oriented in the different direction from the ordinary crystalline spot ('A' and 'B' in Fig. 2 (c)). To each rod shape spot, two atomic sites could be reasonably allotted. Remainder spots shown by arrows in Fig. 2 (c) were too small to allot two atoms. These two spots were half of the rod shaped spot in length but were same in width. These circular small spots tell that the image is originated from single atoms aligned parallel to the electron beam at this position. Connecting each atomic site of the image, we can produce a network model and is shown in **Fig. 2 (d)**. The resultant boundary structure consisted of one 5-membered ring, one 7-membered ring and one distorted 6-membered ring. This experimentally determined structure was quite similar to the model proposed by geometrical consideration by Papon [15] and was also similar to the model produced from an ordinary lattice image [4]. Presently produced atomic model shows that the atomic connection is smooth except for two places shown by arrows. The atom at this place is missing one bonding partner. That is, each atom at this position has one dangling bond.

Ab-initio relaxation

The experimentally obtained atomic structure (**Fig. 3 (a)**) was relaxed by ab-initio calcu-

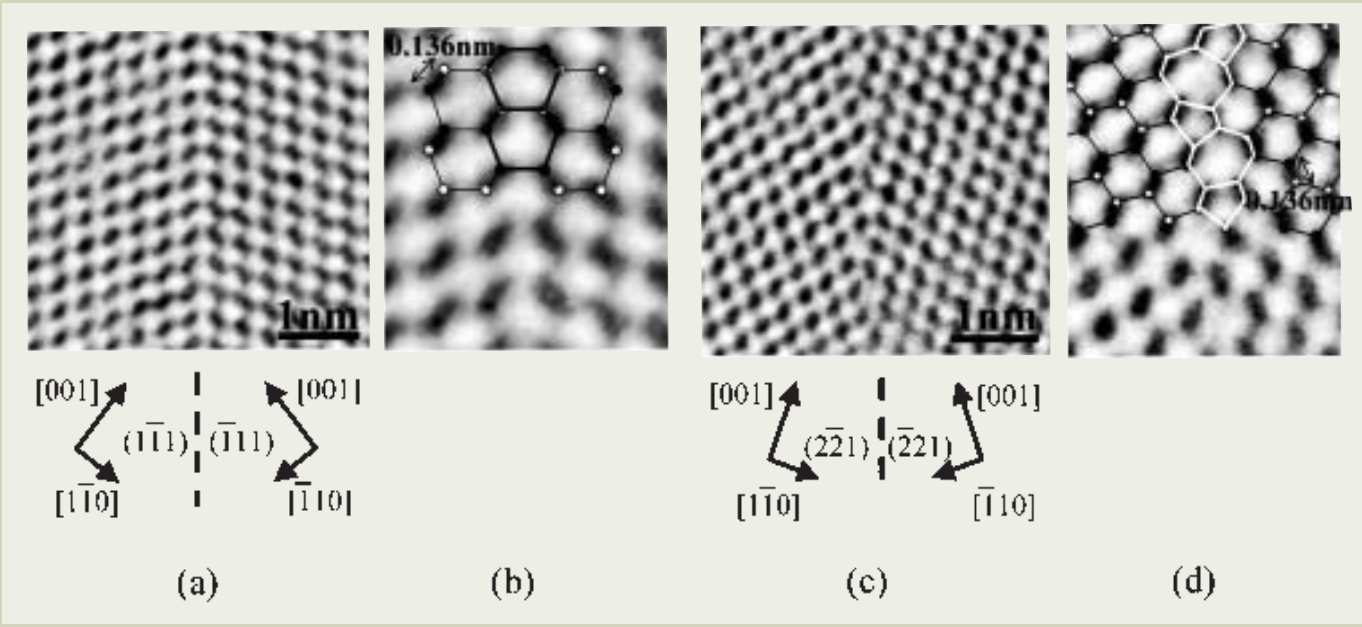

Fig. 1. (a) A high-resolution image of the {111} Σ3 grain boundary in silicon.
(b) An atomic structure network model is superimposed on the ARHVTEM image of the {111} Σ3 CSL grain boundary. Open circles and solid circles respectively correspond to atoms on {110} and {220} plane.
(c) A high-resolution image of the {221} Σ9 boundary in silicon.
(d) A magnified image of the {221} Σ9 boundary. Atomic structure was constructed from the ARHVTEM image. The boundary consisted of 5-membered ring and one 7-membered ring unit, as indicated by white line.

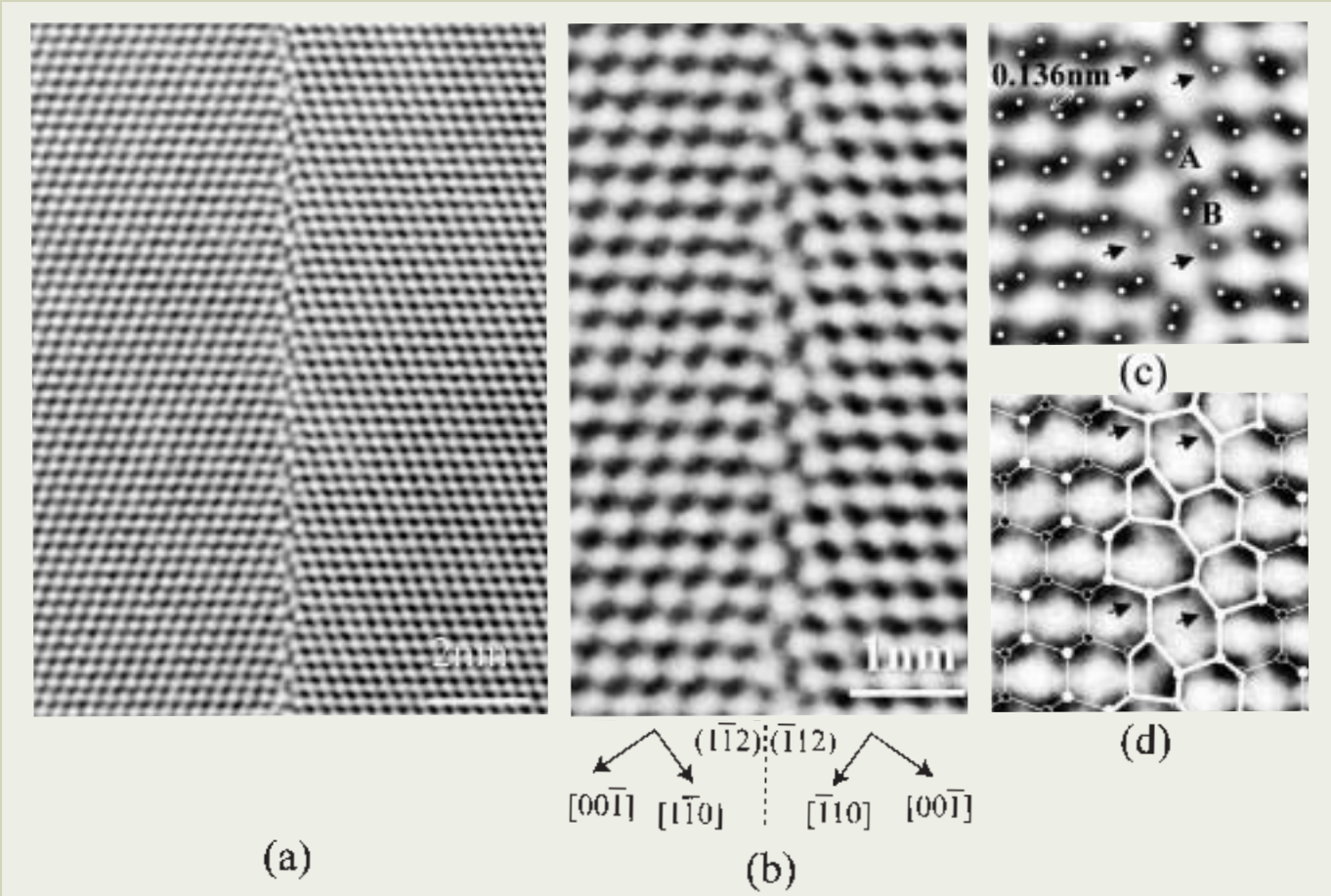

Fig. 2. (a) A HVTEM image of the {112} Σ3 grain boundary in silicon.
(b) A magnified image of (a).
(c) A superimpose of atomic sites on the ARHVTEM image, allotting two atoms to each dark rod-shaped spot and one atom to the small round spots. A single atomic column is indicated by an arrow.
(d) Atomic structure model constructed from Fig. 2 (c).

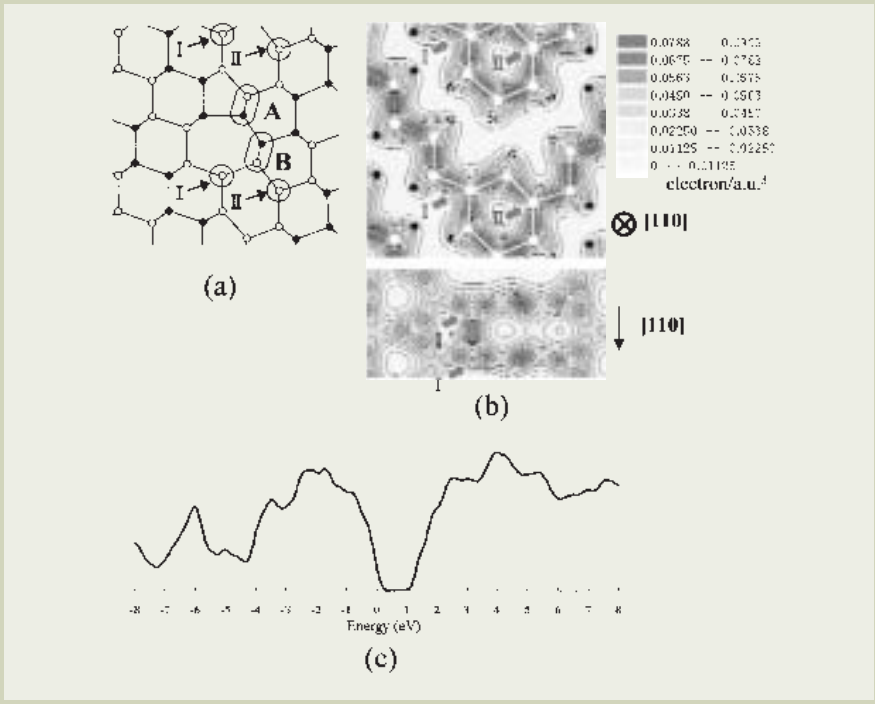

Fig. 3. (a) The atomic structures that obtained by ARHVTEM observation. Each single atomic column is indicated by I and II.
(b) Valence electron density distributions of the boundary by ab-initio molecular dynamics calculation on ($\bar{1}11$) plane and ($\bar{1}\bar{1}1$) plane, which transverse the atom (Ecut 25Ry). The atom located above the atom I along the [110] direction was noted by I'. The bonding between the atom I and I'can be seen along the [011] direction.
(c) The calculated density of states with Ecut of 15 Ry.

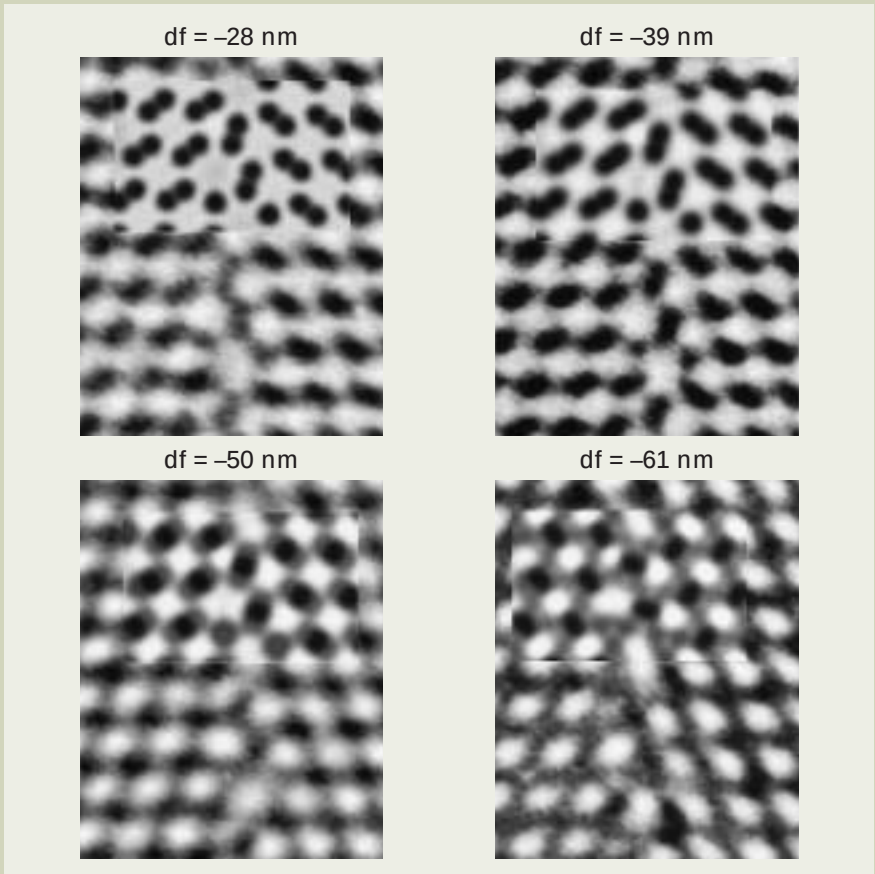

Fig. 4. ARHVTEM experimental image of {112} Σ3 grain boundary at the -28 nm, -39 nm, -50 nm and -61 nm defocus condition (Scherzer defocus: df = -39 nm). Multi-slice simulation image of the relaxation structure by ab-initio molecular dynamics calculation was inserted at each defocus condition. Thickness of the simulated image is 6 nm. Experimental image shows good matching with simulated image. The change in image contrast of the picture due to defocus well coincided to that of simulated image.

lation (**Fig. 3 (b)**). The resultant structure shows that the three fold-coordinated atom moved in [110] direction to get the fourth partner: the three fold-coordinated atom indicated by an arrow and another three fold-coordinated atom that located on the upper (110) plane slightly shifted to make the atomic distance of them favorable (Fig. 3 (b)). The dangling bond at the single atomic column disappeared by the bonding between the atoms I and I' along the [110] direction. The density of states (DOS) of the structure doesn't show the gap peak (**Fig. 3 (c)**) due to the absence of the dangling bond.

ARHVTEM images of the relaxed structure were then simulated by the multi-slice method at several defocus conditions in **Fig. 4**. Similar characteristic feature to the experimental image is seen in the defocus range of −28 nm, −39 nm, −50 nm and −61 nm (Fig. 4). The atomic site corresponded to the darkest spot in the dark spot of the image at the defocus of −39 nm and at −28 nm. The same tendency was also seen in the simulated image.

Summary

ARHVTEM and ab-initio calculation were applied on the silicon grain boundary atomic structure analysis. An atomic column was imaged in dark contrast. A small circular spot represented the single atomic column site in the grain boundary. Grain boundary structure was given simply by connecting the atom site.

References

1. Ichinose H. and Ishida Y.: *Phil. Mag*., **A 43**,1253 (1981).
2. Ichinose H., Tajima Y. and Ishida Y.: *Trans. Japan. Inst. Met. Suppl.*, **253** (1986).
3. J. Thibault, L. Putaux, A. Jacques, A. George, H. M. Michaud and X. Baillin: *Mater. Sci. Eng*., **A164**, 93 (1993).
4. Bourret A. and Bacmann J. J.: *Surf. Sci*., **162**, 495 (1985)
5. Uemura Y., Inomata Y. and Ichinose H.: *J. Ceram. Soc. Japan*, **95**, 788 (1987).
6. Fontaine C., Smith, D. A.: *Appl. Phys. Lett*., **40**, 153 (1986)
7. Sawada H. and Ichinose H.: *Scripta mater*., **44**, 2327 (2001)
8. Ragaru C., Lancin M. and Godon C.: *Eur. Phys. J. AP*, **5**, 135 (1999)
9. Tanaka K., Kohyama M., Iwasa M.: *Materials Science Forum*, Vols.294-296, 187 (1999)
10. Zhang Y., Ichinose H., Nakanose M., Ito K., Ishida Y.: *J. Electron Microscopy*, **48**, 245 (1999)
11. Buis A., Oei Y-S and Schapink F. W.: *Trans. Japan. Inst. Met. Suppl.*, **221** (1986)
12. Kohyama M., Kose S., Kinoshita M. and Yamamoto R.: *J. Phys, Condens. Matter I* 8251 (1989)
13. Ichinose H., Nakanose M.: *Thin Solid Films*, **319**, 87 (1998)
14. Kohyama M., Yamamoto R., Watamabe Y., Ebata Y. and Kinoshita M.: *J. Phys. C, Solid State Phys*., **21**, L695 (1988)
15. Papon A. M. and Petit M., *Scr. Metall*., **19**, 391 (1985).
16. Ichinose H., Sawada H.: Takuma E. and Osaki M.: *J. Electron Microscopy*, **48**, 887 (1999).

The Scanning Electron Microscope as a Tool for Experimental Nanomechanics

Giuseppe Pezzotti

Ceramic Physics Laboratory & Research Institute for Nanoscience, RIN
Kyoto Institute of Technology

We show here that the electron beam can be routinely used for stress measurements in very small volumes, as small as that of atomic clusters. Nano-scale stress measurements can be obtained through piezo-electroluminescence assessments, taking advantage of wavelength shift of native or dopant-induced luminescence spectra. Stress measurement in a field-emission gun scanning electron microscope (FEG-SEM) can be considered to be the first step towards a new field of experimental nanomechanics, whose assessments may open a completely new perspective in the development and quality control of materials and devices. From a materials science perspective, for the first time, we have experimentally visualized how stresses intensify or relax within materials nanostructures, in particular in glass.

Introduction

Luminescence is commonly excited either by photons (photoluminescence, PL) or by electrons (electroluminescence, EL). The former has traditionally been a very important method for studies of ceramics [1,2], the latter is less popular, but it has the advantage that it is easily compatible with surface examination by scanning electron microscopy and with highly local excitation [3]. The effective excitation volume in both PL and EL experiments necessarily includes the finite depth excitation and an additional volume arising from the diffusion of generated excitons (either monochromatic light or electron beam); this latter may make the actually probed volume substantially larger than the nominal probe size [4]. Despite this probe broadening effect, probing by EL may provide a substantial breakthrough in improving the spatial resolution of the spectroscopic measurement towards a nanometric scale, below the typical limit of the micron scale imposed by the finite wavelength of monochromatic light in PL assessments. The piezo-spectroscopic (PS) effect may be defined as the shift in the frequency of a spectroscopic transition in a solid in response to an applied strain or stress. The spectral signal can be due to a variety of different phenomena, *e.g.* Raman scattering or luminescence. Independent of whether monochromatic light or electrons are used as the excitons for stimulating luminescence, the wavelength of the luminescence lines reliably shifts as a function of stress. The ultimate aim is therefore to combine the high-resolution imaging, which has been achieved by FEG-SEM with a reliable nano-scale stress measurement. Based on our measurement experience, we suggest that to achieve an efficient and reliable stress measurement in a nanoscopic environment, it is essential to couple an analytically versatile electron microscope (preferably provided with an in-lens thermal filament) with a sensitive spectrometer, which can analyze the emitted light with superior precision. The combination of these two devices may enable one to collect, upon scanning by electrons but collecting in output wavelength luminescence shifts, a "stress image" to be compared with the conventional SEM image built by secondary-electrons detection.

Matugasakigoshiyokaidouchiyo, Sakyo-ku,
Kyoto 606-8585, Japan.
E-mail: pezzotti@ipc.kit.ac.jp

Theoretical background

The origin of the piezo-spectroscopic effect is that when the lattice of ions surrounding a luminescence atom embedded in the material nanostructure is distorted, for instance by an applied stress, the crystal field potential at the luminescent site is altered which, in turn, changes the energies of the electronic transitions. Thus, by measuring the shift of luminescence spectra, the lattice strain can, in principle, be determined [5]. In the elastic regime, strains are directly proportional to stresses, thus stresses are directly accessible provided that appropriate calibrations of wavelength-shift as a function of stress are preliminary performed. In addition to these well-known notions, we report here for the first time that also the optical activity of defects can be used as a tool for probing the local stress state. In other words, we can apply piezo-spectroscopic techniques to the luminescence arising either from electron-induced transformation of pre-existing point defects or from the creation of new ones. Although the mechanisms of electron-induced transformations of point defects are not exhaustively understood on the atomic scale level [6], from a phenomenological viewpoint, the luminescence emission of such (pre-existing or newly formed) defects occurs at a characteristic wavelength, which depends on the stress state around the defect. This technique has worked suitably for oxygen defects in silica-based glass materials, as we shall show in the successive section. A schematic illustrating the principles of the piezo-electroluminescence measurement is shown in **Fig. 1.** Due to electron-phonon coupling, optical spectra consist generally of broad bands, rather than of separate sharp lines. Broadening is a property, which repeats exactly the same way ('homogeneously') in every instance of a certain defect in a crystal, however, in glass, the site-to-site non-equivalence of difference instances of the same defect causes the optical transition energies to differ. This site-to-site variation results in an additional 'inhomogeneous' broadening of the spectra. Similar arguments may apply when considering the local crystallographic environment around a luminescent atom (*e.g.*, a rare-earth atom) embedded in a glass structure. However, the experimental practice has taught us that the nanometer scale represents a suitable meso-scale for probing stresses within the glass structure in the sense that yet a statistically meaningful number of luminescent sites (either a luminescent atom or a point defect) are available in the probed volume, but also that such number is small enough to make the contribution of inhomogeneous broadening (usually on the order of 0.1 eV) negligible as compared to the much larger homogeneous broadening (typically between 0.3 and 1 eV). The general

notion, according to which the glassy disorder dramatically affects the shape of the luminescence spectrum, thus completely smearing out its sharp features, is based on the assumption of micrometer-size or larger probing (*e.g.*, by a laser beam). The availability of a nanometer-sized probe has newly revealed that luminescence bands may appear to possess an asymmetric profile that can be resolved into a sharp component and a broad shoulder-1ike side band. Leaving aside the broad side band component, which may arise due to inhomogeneous broadening and/or to the presence of sites with different coordinations [7], stress analysis can be performed only on the sharp band component. The plot of this sharp electroluminescence band shift vs. stress can be generally approximated with a straight line for a limited stress range investigated, whose slope (usually referred to as the piezo-spectroscopic coefficient, Π) can be obtained within an accuracy of better than 3%. Our results of stress dependence clearly show that, despite the lack of specific symmetry or long-range periodicity within glass structure, electroluminescence bands shift coherently and precisely with stress.

When a general stress state, σ_{ij}, is applied to a crystal, the piezo-spectroscopic response, seen as a shift of amount $\Delta\nu$ of a selected luminescence band, will be given in terms of the applied stress resolved along its crystallographic axes [8]:

$$\Delta\nu=\Pi_{ij}\sigma_{ij} \quad (1)$$

where the repeated index notation is adopted and the stress tensor, σ_{ij}, is resolved in the crystallographic reference frame. In the general case, the two cartesian systems associated to the principal stress axes and the crystallographic cell axes are not coincident and a transformation matrix of geometrical factors is required:

$$\Delta\nu=\Pi_{ij}a_{ik}a_{jl}\sigma_{ij} \quad (2)$$

where a_{ik} and a_{jl} are the geometrical coefficients of transformation matrices. For the majority of the applications, the stresses are relatively small (*i.e.*, accompanied by strains typically <1%), therefore possible gradients and second-order terms are negligible, greatly simplifying eq.(2). On the other hand, when the strains involved are very large, it can be expected that second-order terms, *e.g.*, those due to shear, may become of significance and a non-linear analysis may be required. In addition, if the sample is polycrystalline or, to a greater extent of disorder, glassy, eq.(2) does not apply. However, if there is no preferential texture and a sufficiently high number of differently oriented grains (for polycrystals) or clusters (for glasses) is probed, eq.(2) can be phenomenologically rewritten as follows:

$$\overline{\Delta\nu}=\frac{1}{3}(\Pi_{11}+\Pi_{22}+\Pi_{33})(\sigma_{11}+\sigma_{22}+\sigma_{33}) \quad (3)$$

where $\overline{\Delta\nu}$ is the band shift averaged over the probed ensemble of grains (or clusters). Note that in eq.(3) the residual stress is considered to be three-dimensional and pseudo-hydrostatic within the probed volume, the piezo-spectroscopic coefficient being merely the trace of the piezo-spectroscopic tensor. Note also that shear stress components are neglected in a volume relatively large with respect to the luminescent moiety. It is immediate to recognize that there exists a dependence of the stress value calculated through eq.(3) on the geometry of the probed volume. For example, if probing is performed upon penetrating the sample surface only by a very thin thickness, the component of stress, σ_{33}, perpendicular to the specimen surface should be neglected. Therefore, the measured band shift corresponds to larger in-plane stresses as compared to the case of a fully hydrostatic stress field. This example illustrates the importance of carefully assessing the probe geometry in piezo-spectroscopic measurements. Some details of such calibrations will be given in the next section.

In statistical terms, the luminescence signal is emitted from any small volume containing a luminescent moiety within the elementary probed volume. If thermal broadening and quantum uncertainty of the energy of the electronic states involved in the luminescence emission process could be neglected, the luminescence band of a crystal under a uniform state of stress should tend to be a single Dirac δ-function. If the stress state is mesoscopically non-uniform, the elementary luminescent moieties of the probed volume may experience different stresses and the wavelength of their respective Dirac functions be shifted of different amounts. It follows that the width of the luminescence band contains, in principle, information on the stress distribution within the probed volume. Ma and Clarke [9] have worked out an expression for alumina relating the band-width to the stress distribution. In glasses, however, broadening has various origins (*i.e.*, inhomogeneous broadening, presence of defects specific exclusively to the glassy state, etc.), which makes it problematic a direct assessment of stress distribution from band-width, without adopting an appropriate criterion for deconvoluting the broad spectrum.

Alumina crystals have the corundum structure, with the oxygen ions arranged in an hexagonal close-packed lattice, with the Al^{3+} ions occupying 2/3 of the octahedral sites. Cr^{3+} ions substitute for Al^{3+} ions in the octahedral sites, with a small trigonal distortion. The luminescence spectrum (a doublet R_1 and R_2) of alumina originates from the characteristic red fluorescence of ruby as a result of the radiative decay of electronic transitions of d^3 electrons of a native Cr^{3+} impurity on Al^{3+} substitutional sites [10]. The strong and sharp fluorescence of the R_1 and R_2 doublet is due to transitions from the ^2E state to the ground state. Lanthanide ions in glass are directly coordinated by MO_4 tetrahedra, with each tetrahedron contributing two oxygens to coordination with the lanthanide. In a glass, due to its inherent disorder and lack of long-range periodicity, the energy levels cannot be accurately assigned. However, we have observed relatively sharp and intense bands in the electroluminescence spectrum. For example, bands at 565, 597, 639, and 693 nm can be assigned to the $4G_{5/2}\rightarrow 6H_{5/2}$, $4G_{5/2}\rightarrow 6H_{7/2}$, $4G_{5/2}\rightarrow 6H_{9/2}$, and $4G_{5/2}\rightarrow 6H_{11/2}$ transitions, respectively [11]. Spectra reported for Sm-activated phosphors [12] demonstrated that the most intense peak of Sm^{3+} is the highest-energy peak (ranging from 594 to 608 nm) of the 590-620 nm region. The reported optical luminescence bands of defects in non-doped synthetic silica are numerous and the assignment of the bands is still controversial in some cases. A complete discussion of oxygen-related defects in silica is beyond the scope of this paper. Here, it should be remarked only that the most controversial is the region around 4.8 eV, in which bands arising from oxygen excess-related defects (*e.g.*, three oxygen-excess defects, peroxy radical defects, non-bridging oxygen hole center) overlap [13]. A relatively intense band located at 1.9 eV (630 nm) is unequivocally related to the presence of Si-O non-bridging oxygen hole center. While the exact position of each single emission remains somewhat uncertain for oxygen-excess defects, optical bands arising from oxygen deficiency-related defects are relatively well characterized [13]: two intense bands located at 2.7 eV (460 nm) and 3.0 eV (410 nm) can be ascribed to dicoordinated Si and Ge, respectively. An additional band, related to interstitial O_2, has been reported at higher wavelength [14].

Experimental procedures

The scanning electron microscope (SEM) employed in this study was a new thermal filament type field emission gun (FEG) device with a lateral spatial resolution of 1.5 nm (JSM-6500F). The microscope was mounted within a cut-out on an air-suspended optical table, thus eliminating vibration and aiding optical alignment. A high-sensitivity cathode luminescence detector unit (MP-32FE, Horiba Ltd., Kyoto, Japan) was employed for the collection of light upon reflection into an ellipsoidal mirror and transmission through an optical fiber. The emitted light spectrum was analysed using a triple-monochrometer equipped with a CCD camera. A new mapping device (PMT R943-02 Select, Horiba Ltd., Kyoto, Japan) and related software was developed which enabled us to collect with nanometric spatial resolution, and automatically analyze, a large number of spectra. The collected data were analyzed with the curve-fitting algorithms included in the SpectraCalc software package (Galactic Industries Corp.).

The signal from a neon discharge lamp was systematically collected, concurrently to each measured spectrum, for obtaining an external frequency calibration [15]. In the present measurements, the strategy for obtaining very high spatial resolution was the same as that previously suggested by Warwick [16]: (i) using a low accelerating voltage ($\leq$ 1.5 kV) to inject electrons into the surface with minimal lateral scattering (1.5 nm); (ii) using a small probe generated by a bright, field-emission source; (iii) detecting photons from pre-diffusion radiative recombination events. We were aided in this effort by the high efficiency of the luminescent probes used in this study. In particular, in the case of rare-earth doped glasses, a spectrum of good quality, suitable for precise mathematical fitting, could be collected within one second. It should be noted that the efficiency of a selected lanthanide activator can vary considerably with concentration and upon the concurrent presence of other lanthanide impurities; however, the relative efficiency of

luminescence in a specific host is essentially site-independent [17].

It is well known that in modern FEG-SEM devices the spot size of the electron beam is much smaller than the spatial extent of the beam energy dissipation volume, even at low beam energies of 1 or 2 keV. In the absence of excessive beam charging and the accompanying astigmatism this may introduce, the resolution is therefore determined almost entirely by the interaction of the beam with the sample. One semi-empirical way to calculate the beam energy dissipation volume is using the Grün-range-related method proposed by Everhart and Hoff [18]. The modified Grün equation, giving the maximum penetration depth or electron range, R_g, can be written as:

$$R_g = \frac{0.0398}{\rho} \sqrt[1.75]{E_{acc}} \quad (\mu m) \qquad (4)$$

where ρ and E_{acc} are the material density in g/cm^3 and the acceleration voltage in keV, respectively. A good first approximation of the lateral extension of the excitation volume is a circle with the same diameter as the penetration depth. An acceleration voltage E_{acc} 1.5 keV was employed throughout the experiments. Typical scattering of the electron beam in the subsurface of the specimen is shown in Fig. 1. Despite the occurrence of electron beam broadening, a high spatial resolution better than 10 nm could be achieved in any measurement of the present study, as calculated according to the modified Grün equation.

A four-point bend loading micro-jig (**Fig. 2 (A)**) was equipped with a load cell of 100 N and placed under the optical microscope into the electron microscope. Luminescence spectra were mapped to calibrate the stress dependence of sapphire and various glasses. Optical fibers were directly calibrated by using a laboratory-made tensile micro-jig, as shown in **Fig. 2(B)**. In the rather short time necessary for collecting fluorescence spectra in the present materials, no significant relaxation in the loading jigs could be detected.

The sapphire crystal was a well-annealed commercially available crystal (Nakazumi Crystal Lab.) nominally pure (*i.e.*, containing 0.005 wt.% Cr as a native impurity). The alumino-silicate glass (60-Silica/5-Alumina/20-Alkaline-metal-oxide/15-Multi-valent metal oxide (in mol%)) was a commercially available grade from Hoya Corp. Electro-Optics Co. This glass was prepared using a conventional melt-quenching method, after mixing the raw powders with SmF_3, in order to obtain a final concentration of the lanthanide element (*i.e.*, the luminescent probe) of 1000 ppm (in mole). Quenching experiments were performed either by fast dipping in molten ice or by direct contact in a metal anvil, the quenching rates in these two cases being approximately 0.1 and 100 K/s, respectively. Nd^{3+} and

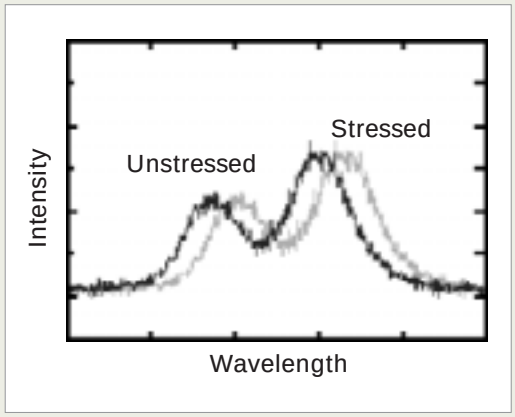

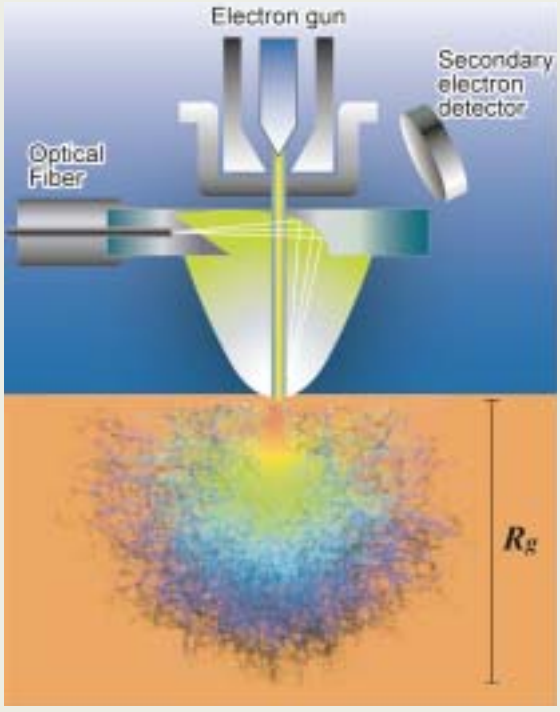

Fig. 1. Schematic of piezo-electroluminescence measurement and beam broadening effect (with reference to eq.(4)).

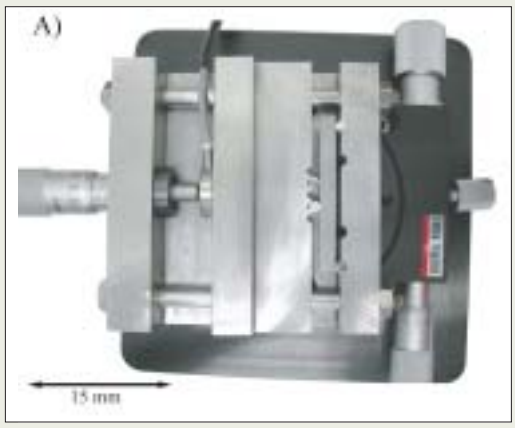

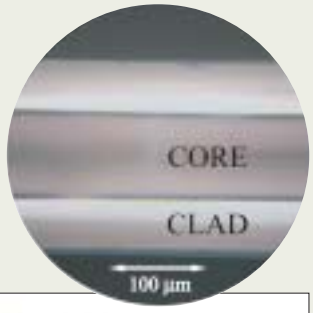

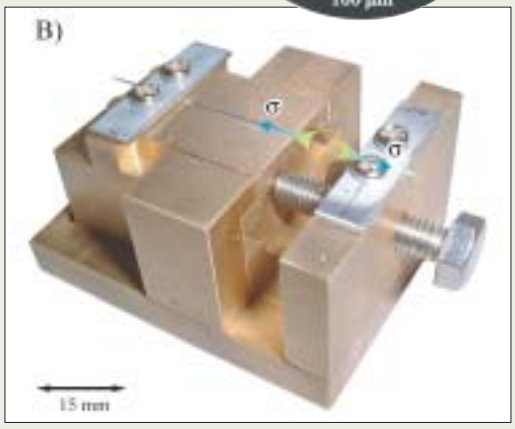

Fig. 2. Miniature jigs for four-point bending loading and tensile (fiber) loading, in (A) and (B), respectively.

Er^{3+}-doped silica optical fibers were core/clad-structured laboratory-made devices. They were obtained from two separate Japanese companies whose identity we cannot reveal for industrial reasons. The latter fiber contained also an unknown fraction of Ge-ion as a co-dopant for the core structure.

Results and discussion

Electroluminescence spectra were collected at identical locations upon successively increasing the externally applied stress, and the relative spectral shift, $\Delta\nu$, with respect to the unstressed wavelength accurately measured. To minimize the error involved with instrumental fluctuations, a suitable band from a neon discharge lamp was recorded concurrently to each individual spectrum and its known wavelength assumed as a reference. A grid comprising of 5×10^3 spectra was collected with the electron beam focussed to a spatial resolution of about 30 nm, to approximately cover an area of 5 µm per each stress data point. This procedure was repeated at 10 different stress states and the wavelength band shifts recorded. Given the dependence of electroluminescence spectra on the electron beam orientation angle and local structures, an average band shift was calculated with respect to a matrix of unstressed wavelengths collected at the same locations. To a degree of accuracy, all bands of all the investigated materials shifted linearly with the applied stress. Electroluminescence spectra and the dependence of selected bands from the Sm^{3+}-doped alumino-silicate glass, pure silica, Er^{3+} or Nd^{3+}-doped silica, and single-crystal sapphire on uniaxial stress, σ_u, are shown in **Figs. 3 (A)-(E)**, respectively. In the plots, a negative sign indicates a compression stress. The results of stress calibration in glasses, as compared to crystalline sapphire, clearly show that, despite the lack of specific symmetry or long range periodicity within the glass structure, electroluminescence bands shift coherently and precisely with stress. Another interesting finding is that bands related to glass defects, despite their relative broadness, are very sensitive to stress (*i.e.*, piezo-spectroscopic coefficient more than one order of magnitude larger) as compared to bands arising from rare-earth-activated phosphors.

As an application of the microscopic stress measurement into the FEG-SEM, **Fig. 4** shows

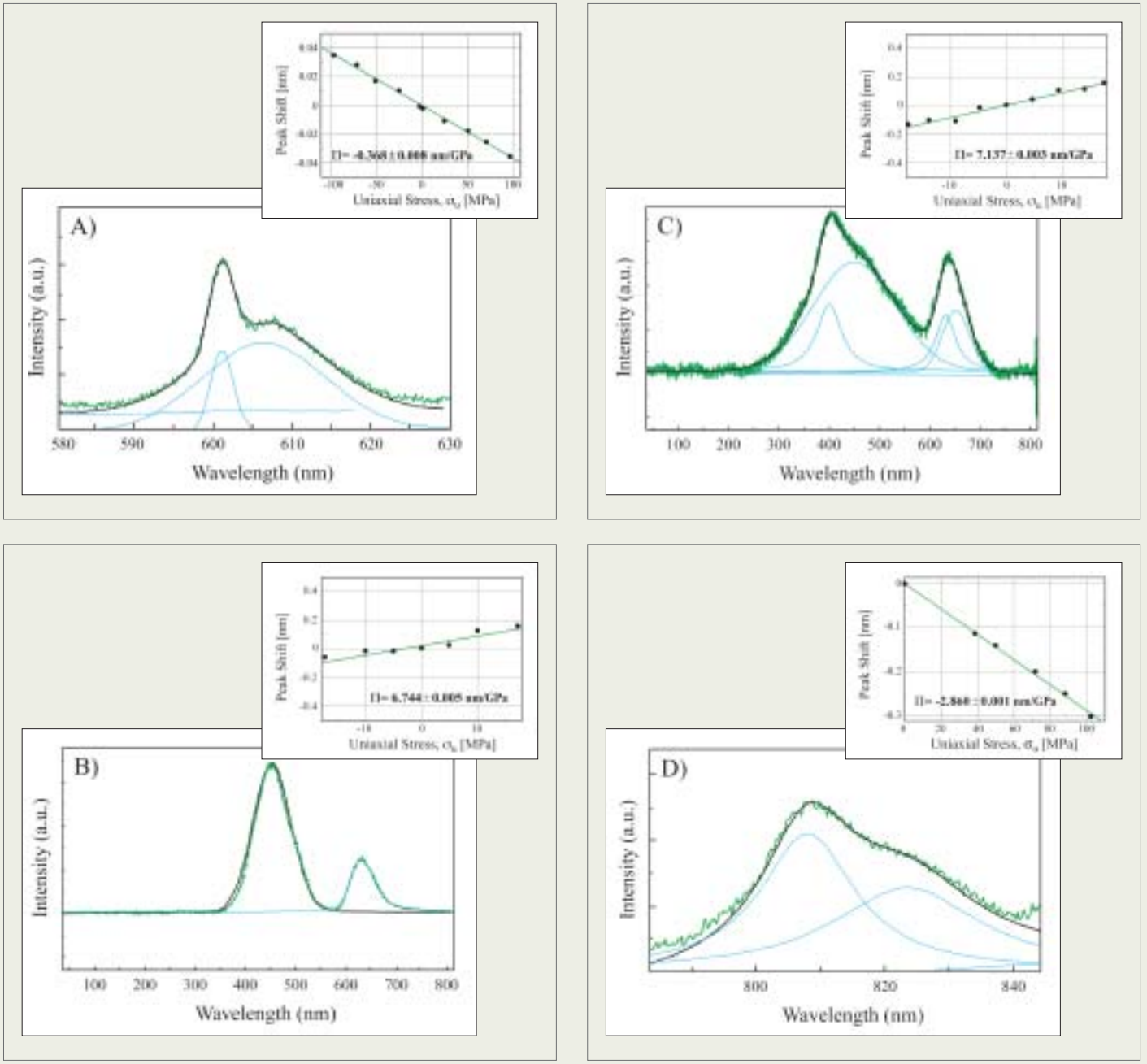

the stress profile recorded across an indentation print on a polished and well-annealed surface of Sm^{3+}-doped alumino-silicate glass. The linear stress map, collected using electrostimulated peak shifts with the relatively low spatial resolution of 200 nm, clearly indicates a region of high compressive stress that corresponds with the indentation print, whilst a region of low tensile stress (with a maximum tensile stress of about 300 MPa) was recorded outside the indentation location. This characteristic microscopic stress distribution is similar to that recorded by photoluminescence for indentations in other brittle materials [19].

The microscopic cracks generated at the edge of the indentation print in brittle materials can be regarded as equilibrium cracks embedded in an infinite medium [20]. Assuming that glass behaves as a brittle material, the stress field ahead of a crack tip, $\sigma_t(x')$, along an abscissa, x', with origin at the crack tip and oriented towards the crack propagation direction, should obey the following equation [21]:

$$\sigma_t = \frac{K_{IC}}{\sqrt{2\pi x'}} \qquad (5)$$

Therefore, the slope of a plot of σ_t vs $1/\sqrt{2\pi x'}$ represents the crack-tip toughness, K_{IC}, of the material [22]. This plot, collected with a probe size of 30 nm at the tip of the indentation crack, is shown in inset in Fig. 4. Despite the data scatter (presumably due to the nanostructure of the specimen, as discussed later), a least-square fitting locates a slope corresponding to $K_{IC}=0.75 \pm 0.1$ MPa $\times$ $m^{1/2}$. This value is reasonable for glass and comparable with that experimentally measured by macroscopic fracture mechanics assessments [23]. At this stage, it seems reasonable to assume that we are obtaining, through piezo-electroluminescence assessment, a reasonable and consistent estimate of microscopic stresses in the FEG-SEM, at least comparable with that obtained by the more popular piezo-spectroscopy technique based on photo-stimulated spectroscopies [5]. The next challenge would be to expand the possibility of stress measurement towards the nanometer scale, thus exploiting the high potential for improving spatial resolution offered by the electron beam.

Interesting structural observations can be made by examining the (local) nanometric distribution of stress developed within a glass

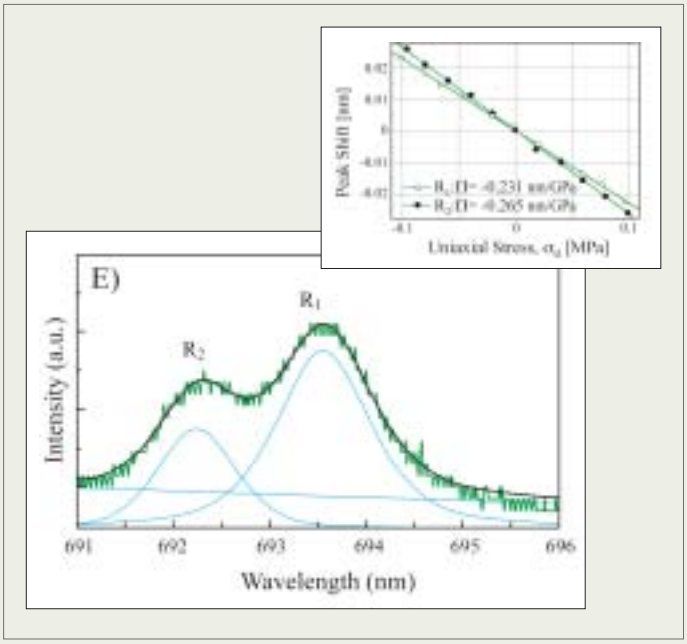

Fig. 3. Typical electroluminescence bands, their spectral deconvolution and stress dependence for Sm-doped alumino-silicate (A), pure silica (B), Er/Ge-doped silica (C), Nd-doped silica (D), and Cr-doped sapphire (E). In this latter spectrum, both bands, $\mathbf{R_1}$ and $\mathbf{R_2}$, were probed with respect to their stress dependence; in (A), only the sharp component of the deconvoluted spectrum was calibrated with respect to shift upon applied stress. In (B) and (C), stress calibration is shown for the 630 nm and 460 nm band, respectively. In (D), only the more intense band component was characterized.

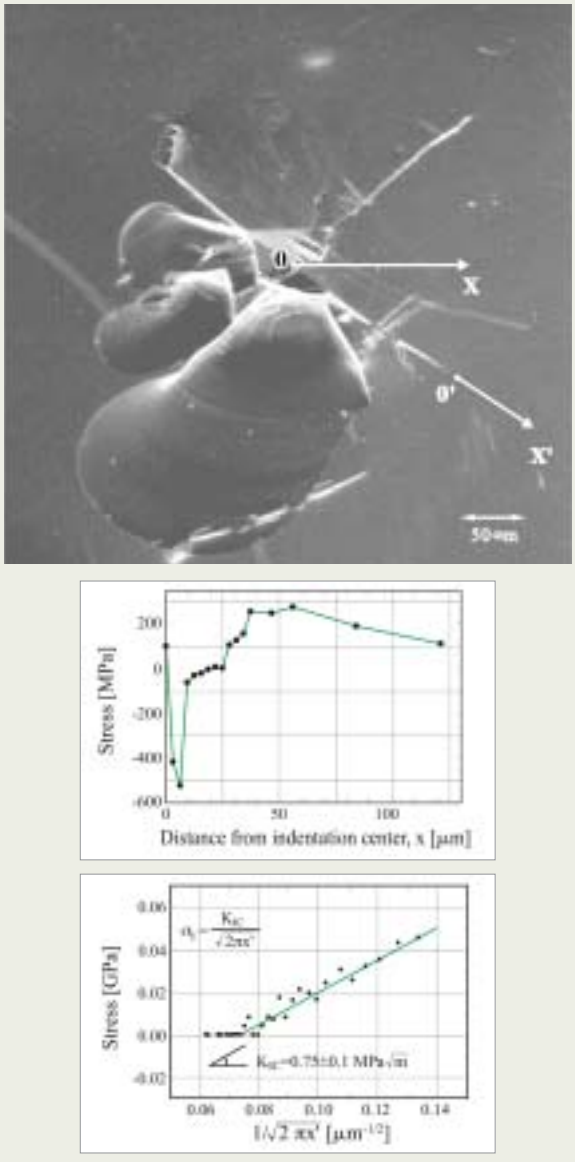

Fig. 4. Indentation print in Sm-doped alumino-silicate glass and microscopic stress distributions as detected by piezo-electroluminescence along an abscissa, x, with origin at the center of the print (perpendicular to the indentation edge) and along an abscissa, x', with origin at the tip of a microcrack originated at the corner of the indentation (directed towards the crack propagation direction).

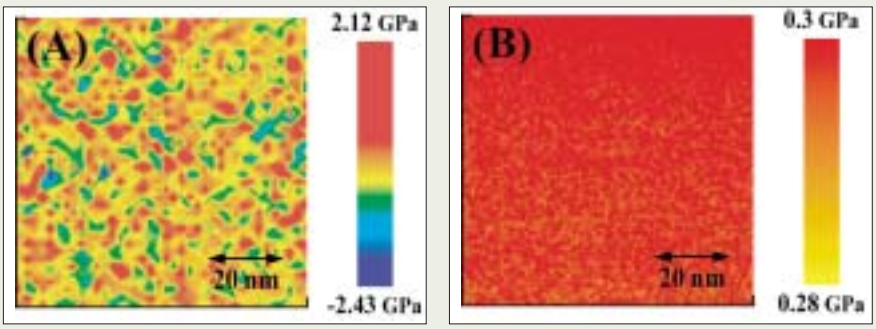

Fig. 5. Nanometer-scale stress distributions in alumino-silicate glass (A) and sapphire crystal (B). The same far-field tensile stress (300 MPa) was applied to both materials. Note the micellar nanostructure shown by the glass, as compared to the rather homogeneous stress distribution experienced by the crystal.

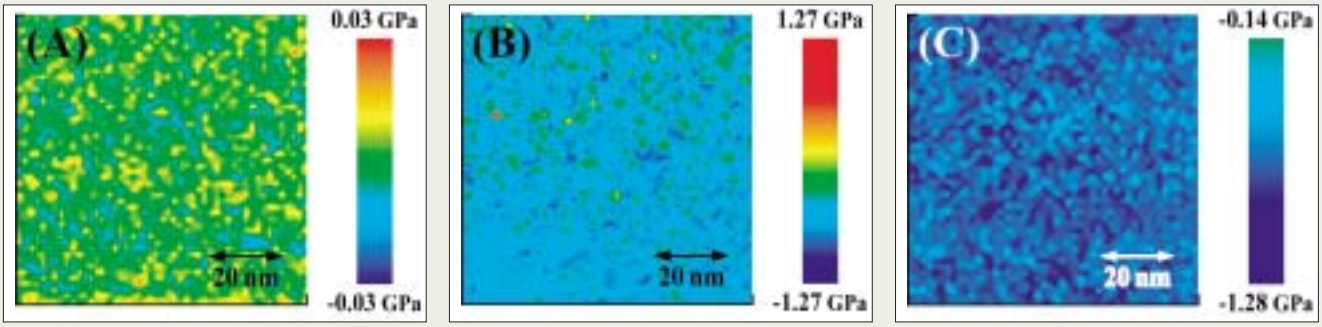

Fig. 6. Nanometer-scale stress distributions in well-annealed Sm-doped alumino-silicate glass (A), and, in the same glass, quenched at different quenching rates, $\dot{T}=10^{-1}$ and 10^{2} K/s (in (B) and (C), respectively). Note the highly compressive residual stress developed upon quenching, the faster the cooling rate the higher the stress.

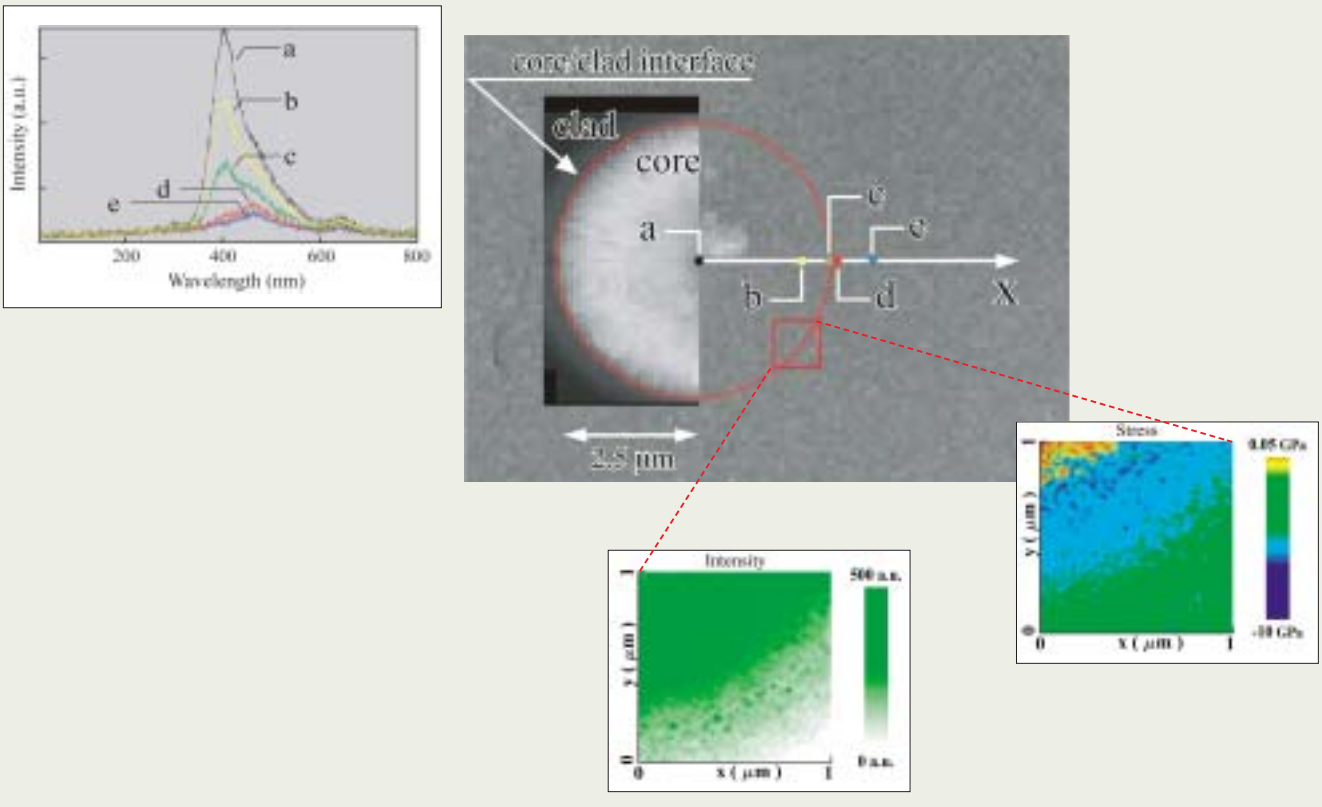

Fig. 7. FEG-SEM micrograph of an area on the section of an Er/Ge-doped optical fiber device and the evolution of the electroluminescence spectrum from the center of the core towards the clad. Band intensity maps of the 410 nm band collected in the overall core and (with higher magnification) nearby the core/clad interface are shown. A hydrostatic stress map nearby the core/clad interface is also shown. The spatial resolution of the stress measurement here was better than 5 nm.

structure, as compared to a crystalline structure under the same far-away stress field. This comparison is shown for alumino-silicate glass and sapphire in **Figs. 5 (A)** and **(B)**, respectively. Noticeably, a periodic stress distribution was revealed to exist with a nanometer scale in glass, which was not observed in crystalline sapphire. When evaluated at a nanometric scale, local stresses were clearly higher (*i.e.*, up to the GPa level) when compared to the applied (far-field) stress. However, it was always noted that the arithmetical average of nanostress values, calculated over micrometre-scale areas, resulted in values very close to the far-field stress. Therefore, it seems that we have experimentally verified the hypothesis that glasses are composed of micelles or paracrystals characterized by a degree of order intermediate between that of a polycrystal and that of a random array [24]. In recent X-ray studies using the Rietveld method [25], very small crystallized fractions could be found, which corresponds to a degree of regular spacing with nanometre-scale intervals, some 20 times that of the Si-O interatomic spacing. These paracrystalline features on a nanometer scale may themselves be arranged in arrays with differing degrees of structural order. Glass-in-glass structural separation upon cooling may lead to local differences in density. Durville et al. [26] used the luminescence of Cr^{3+} in order to investigate the incipient crystallization of a silicate glass and to characterize glass ceramics. In their studies, use was made of the fact that Cr^{3+} ion prefers the crystalline above the amorphous phase. On the other hand, rare-earth ions show a luminescence spectrum fairly independent of the bonding environment [17]. According to this argument, we may consider, in first approximation, the rare-earth ions to be homogeneously distributed throughout the glass structure, without segregating to preferential sites. These notions may strengthen the idea that, in our nanomechanics assessments, the stress state within the glass structure has been sensed without being significantly influenced by the segregation behavior of the atomic stress sensor installed into the glass structure, namely by the local structure present in the probed volume.

Residual stress maps were also collected on the surface of glass specimens, which were quenched from high temperature. Two examples of structures quenched from the same temperature with different cooling rates are shown in **Fig. 6 (B)** and **(C)**. A micellar structure very similar to that observed in the well-annealed glass sample (**Fig. 6 (A)**) was present in a mildly quenched sample, while a finer micellar structure was "frozen" at a higher cooling rate. The (average) surface residual stress field, compressive in nature, significantly increased with increasing the cooling rate. However, the maximum compressive stress, carried by highly packed micelles, was independent of cooling rate. In other words, we have visualized the well known notion that compressive stresses higher than a threshold value make the structure of glass macroscopically deform in an anelastic fashion, due to shrinkage of a loosely bonded network which obeys an apparently low bulk modulus. From a more general point of view, the way nanometer-scale stresses distribute within the glass structure proves the coexistence of strong and weak interpenetrating networks, with the attendant appearance of cohesive molecular groupings. In other words, our piezo-electroluminescence observation experimentally proves that, in the general case, the nanostructure of glass *is not* a continuous random network.

A straightforward application of the technique can be shown for optical fiber devices. **Figure 7** shows a conventional FEG-SEM micrograph of the fiber section in an Er^{3+}-doped device, whose bands in the clad and core regions were shown in Figs. 3 (B) and (C), respectively. The variation of the local spectrum from the core center towards the clad region is shown together to a band intensity map and a residual stress map (in insets), as collected nearby the core/clad interface using the relatively sharp band located at 410 nm. The spatial resolution of this stress measurement was better than 5 nm. The stress map clearly indicates a region of relatively high tensile stress that corresponds with the core area, whilst in the clad region a compressive-stress region was found in the neighborhood of the core/clad interface. It should be noted that the 410 nm band was generally not detectable in the clad area, however, the stress at the core/clad interface could be measured by virtue of a certain amount of ions, which diffused during processing from the core area towards the clad (cf. intensity map in inset of Fig. 7). The diffusive area was about 0.5 µm in thickness. The compressive stress developed within the intermediate (diffusive) region counterbalances the residual tensile stress developed in the core. The maximum stress magnitude recorded with a nanometric spatial resolution was of the GPa order, however the stress distribution was highly inhomogeneous. The detected inhomogeneous (micellar) structure was similar to that observed Sm^{3+}-doped glass samples. The results of nanomechanics characterizations suggest a significant impact of nanostresses, as developed during fiber processing, on the mechanical and optical performance of the fiber device. The residual stress contribution to the refractive index can be rigorously characterized by tensorial stress-optical equations [27]. Briefly here, a residual compressive stress stored in the clad of the fiber will produce an increase in the refractive index of the fiber clad, whereas a tensile residual stress will decrease the refractive index of the core. Therefore, the mismatch in refractive index between core and clad can be significantly reduced by the residual stress field, with significant impact on enhancing the signal loss in the glass fiber device.

Conclusion

The presently available experimental and theoretical evidence indicates that *stress microscopy* can be routinely pursued into the FEG-SEM. Piezo-electroluminescence can provide a unique tool for the quantification of stress information on a nanometer scale within both crystals and glasses. While the primary subject of this article was the evidence concerning the possibility of estimating stresses on a nanometer scale, much of the spectroscopic outcomes can also be applied to obtain structural information, upon appropriate statistical analysis of the obtained spectra, thus using local deformation as a means for imaging glass nanostructures. High-resolution scanning piezo-electroluminescence provides a direct and unique insight into the mechanics of molecular clusters and a better understanding of the mechanical behavior of solids, which will ultimately lead to the improved design of material structures, and control of nanotechnology devices.

References

1. T. Toyoda, T. Obikawa, T. Shigenari: *Mater. Sci. Eng. B*, **54**, 33 (1998).
2. G. Pezzotti: *J. Raman Spectr.*, **30**, 867 (1999).
3. A. Gustafsson, M-E. Pistol, L. Montelius, L. Samuelson: *J. Appl. Phys.*, **84**, 1715 (1998).
4. A. E. Grün: *Z. Naturforsch. A*, **12a**, 89 (1957).
5. Q. Ma and D. R. Clarke: *J. Am. Ceram. Soc.*, **77**, 298 (1994).
6. L. Skuja: *J. Non-Cryst. Solids*, **239**, 16 (1998).
7. G. Vijaya Prakash and R. Jagannathan: *Spectrochim. Acta*, **A55**, 1799 (1999).
8. L. C. Ciacchi, G. Gregori, V. Lughi, A. Rossi, V. Sergo: *Recent Res. Develop. Applied Spectroscopy*, **2**, 243 (1999).
9. Q. Ma and D. R. Clarke: *J. Am. Ceram. Soc.*, **76**, 1433 (1993).
10. J. He and D.R. Clarke: *J. Am. Ceram. Soc.*, **80**, 69 (1997).
11. G. K. Das Mohapatra: *Phys. Chem. Glasses*, **40**, 57 (1999).
12. M. S. Magno, G. H. Dieke: *J. Chem. Phys.*, **37**, 2354 (1962).
13. L. Skuja, K. Tanimura, N. Itoh: *J. Appl. Phys.*, **85**, 3518 (1996).
14. W. Carvalho, P. Dumas, J. Corset, V. Newman: *J. Raman Spectr.*, **16**, 330 (1985).
15. G. Pezzotti: *Microscopy & Analysis*, **33**, 5 (2003).
16. C. A. Warwick: *Inst. Phys. Conf Ser. No 117*, **10**, 681 (1991).
17. G. Boulon: *Mat. Chem. Phys.*, **16**, 301 (1987).
18. T. E. Everhart and P. H. Hoff: *J. Appl. Phys.*, **42**, 5837 (1971).
19. S. E. Molis, D. R. Clarke: *J. Am. Ceram. Soc.*, **73**, 3189 (1990).
20. J. Rödel, E. R. Fuller, Jr., B. R. Lawn: *J. Am. Ceram. Soc.*, **74**, 3154 (1991).
21. P. C. Paris and G. C. Sih: in *Fracture Toughness Testing and its Applications*, pp. 30-83 (ASTM Tech. Publ., NY, 1965).
22. A. G. Haerle, W. R. Cannon, M. Denda: *J. Am. Ceram. Soc.*, **74**, 2897 (1991).
23. J. Mencik: *Strength and Fracture of Glass and Ceramics*, Elsevier, NY, 1992, p.120.
24. P. J. Flory: *Science*, **188**, 1268 (1975).
25. X. Orlhac, C. Fillet, P. Deniard, A. M. Dulac, R. Brec: *J. Appl. Cryst.*, **34**, 114 (2001).
26. F. Durville, B. Champignon, E. Duval, G. Boulon: *J. Phys. Chem. Solids*, **46**, 701 (1985).
27. U. C. Paek and C. R. Kurkjian: *J. Am. Ceram. Soc.*, **58**, 330 (1975).

Observation of Dislocation Structures of Fatigued Metallic Materials by Scanning Electron Microscopy

Yoshihisa Kaneko and Satoshi Hashimoto

Department of Intelligent Materials Engineering, Faculty of Engineering, Osaka City University

In order to predict crack nucleation in fatigued metallic materials, it is strongly desired to clarify instantaneous dislocation structures which can lead to fatigue cracking. However, because conventional TEM observation must include the process that materials are shaped to thin foils, direct dislocation observation has been difficult for the purpose of damage inspections of engineering parts in use. Recently, the electron channeling contrast imaging (ECCI) which enables nondestructive dislocation imaging in bulk samples has rapidly been developed. With a help of the ECCI method performed in an FE-SEM, characteristic dislocation structures peculiar to fatigue phenomena were successfully observed. Accordingly, it is suggested that the ECCI method is suitable for the nondestructive inspection of the fatigued materials.

Dislocation Structure and Crack Nucleation in Fatigued Metallic Materials

Most of engineering metallic materials are collectives of crystals. Individual component crystals usually contain several kinds of lattice defects. Dislocation is one of linear lattice defects. The dislocation plays an important role in stressed crystals. When an applied stress exceeds a yield point, the crystal begins to deform plastically by means of dislocation movements along slip planes. With the increasing amount of plastic deformation, dislocation density would increase due to the occurrence of multiplication mechanisms such as activation of the Frank-Read source and the double cross slip. Such an increase in the dislocation density causes strain hardening of crystals.

Under unidirectional deformation, the multiplied dislocations are tangled each other and/or arranged linearly along slip planes, depending on several factors relating to dislocation behaviour. Distributions of these dislocations are rather homogeneous. On the other hand, to-and-fro motion and cross slip of dislocations occur frequently during fatigue deformation. Such dislocation motions induce multiplication and mutual annihilation of the dislocations. Resultant dislocation distribution produced by fatigue deformation has been established by many fundamental researches [1]. If these multiplication and annihilation are repeated sufficiently, the dislocations are usually self-organized into dislocation bundle structure called "vein" in crystals having relatively high stacking-fault energy. The vein structure is composed from high- and low dislocation density regions which have irregular shapes. The dislocation density amounts to 10^{11} cm^{-2} at the high density region. Further fatigue cycling can give rise to the formation of "persistent slip bands (PSBs)" along the primary slip plane in the vein structure if plastic strain amplitude is in a certain range. The PSBs were originally reported in optical microscope observations as a slip band persistently reappeared by load cycling even after specimen surface layer was removed. The dislocation structure of the PSB has been studied using transmission electron microscopes (TEM). The morphology of the PSB dislocation structure is characterized by ladder-like dislocation structure as schematically shown in **Fig. 1**. The ladder-like structure is composed from regularly-spaced dislocation walls which are considered as the collective of edge dislocation multipoles.

The fatigued crystals are strain-hardened with development of the PSB and vein dislocation structure. After the fatigue cycling is sufficiently applied to the crystal, cyclic stress-strain responses such as stress amplitude would be saturated. Internal substructure of a saturated crystal is composed from two phases —— the PSB and the vein structures —— in single-slip-oriented copper fatigued at plastic strain amplitude ranging from 6×10^{-5} to 7.5×10^{-3}. Volume fractions of these two phases depend on the plastic strain amplitude: the PSBs are dominant at high strain amplitude. This is because the PSB can carry very large plastic strain in comparison with the vein matrix structure. Because slip activities are concentrated at the PSBs, pronounced extrusions and intrusions are generated at intersections of the PSBs with crystal surface, due to random slip processes. Moreover, volume expansion of the PSBs occurs owing to production of vacancies. Due to such fatigue-induced phenomena, rough surface topology appears locally at the PSBs as shown in **Fig. 2**. It has been recognized that intragranular fatigue cracks are nucleated preferentially at the PSBs [2-5]. Stress concentration due to such rough surface is expected to cause the preferential crack nucleation.

During further fatigue loading, the nucleated cracks continue to propagate across crystals, and subsequently a final fatigue rapture occurs. It is well known that such fatigue raptures often lead to serious accidents in various engineering structures. In order to prevent the fatigue rapture, nondestructive inspections including X-ray and ultrasonic wave methods have been employed for detecting fatigue cracks. However, in order to improve the prevention of the fatigue rapture, it is desirable to perform prediction of fatigue crack nucleation rather than the detection of the cracks which are already nucleated. Because the PSB formation precedes to the fatigue crack nucleation as mentioned above, it is feasible that the detection of the PSB formation corresponds to the prediction of the fatigue crack nucleation. However, the conventional TEM observation must include a shaping process to a thin foil: it can be said that the TEM observation is inadequate for the inspection of engineering parts which are in use. Accordingly, a nondestructive method to observe dislocation structure is desirable instead of the TEM.

Electron Channeling Contrast Imaging

Recently, a new observation technique called 'electron channeling contrast imaging (ECCI)' has been employed to image dislocations (see review [6]). The ECCI method has a characteristic feature that the dislocations lying close to crystal surface can be detected nondestructively using a scanning electron

Sugimoto 3-3-138, Sumiyoshi-ku, Osaka 558-8585, Japan.
E-mail: kaneko@imat.eng.osaka-cu.ac.jp

microscope (SEM). Because of the surface observation using the SEM, it appears that the ECCI method is suitable for the damage inspections at the fatigued materials. In addition, the ECCI has some advantages in examining the dislocation structure in the fatigued materials. If we use the TEM, visible field of a thin foil sample is limited to narrow area where the incident electron beam can pass through. Hence, the TEM observation at low magnification such as ×100 is almost impossible. In such a situation, there is a risk that one can miss the PSB formation if the total number of the PSBs generated in material is very few. Moreover, surface layer of materials is difficult to be observed by the TEM because of difficulty in foil preparation. This seems inconvenient for investigations of fatigue processes since most fatigue cracks are nucleated at the surface layer. On the other hand, the ECCI technique enables us to observe the dislocation structure of the surface layer at various magnifications.

When the incident electrons are penetrated into material, it is considered that some incident electrons are deflected around atomic nuclei at large angle more than 90°. Such backscattered electrons can escape from crystal surface. By detecting the intensity of the backscattered electrons, we would obtain several information including Z-contrast, topographic contrast and electron channeling contrast [7]. The electron channeling contrast phenomena was reported first by Coates [8] as Kikuchi-like reflection patterns in SEM. This electron channeling contrast comes from a specific characteristic that the intensity of the backscattered electrons is sensitive to the incident beam orientation relative to lattice planes. The beam orientation dependence of the backscattered electron intensity has been described often by the Bloch waves of two types [9]. According to the calculation based on the two-Bloch wave model [10], the intensity of the backscattered electrons changes with incident beam angle as schematically shown in **Fig. 3**. It should be emphasized that the intensity decreases rapidly at the angle where the Bragg condition is satisfied.

In 1967, Booker et al [11] have proposed a possibility that dislocations are detectable in SEM by imaging the backscattered electron intensity which shows rapid change in the vicinity of the Bragg angle. Let us consider the dislocation imaging mechanism in SEM. In the vicinity of a dislocation, lattice planes are slightly bent and their lattice spacings are also varied locally. This kind of lattice distortion gives rise to small change in the Bragg condition when the incident beam is applied to the crystal. In order to observe the dislocations using the ECCI, crystal samples need to be rotated suitably such that the Bragg condition is satisfied between the incident beam and a certain lattice plane. Because the backscattered electron intensity changes rapidly near the Bragg angle as shown in Fig. 3, the channeling contrast would emerge around the dislocations which induce the local change in the Bragg condition. Accordingly, we can image the dislocations lying close to crystal surface by scanning the incident beam tilted at the Bragg angle and by detecting the backscattered electrons that escape from the surface. Details of the dislocation image profiles in the ECCI have been calculated by Clarke et al [12] and Wilkinson et al [13, 14].

Early experimental studies on the ECCI technique were examined in thin foils [15, 16]. This is because the dislocation imaging in bulk samples was difficult due to substantial background signal. In a bulk sample, the electrons backscattered from interaction volume can become dominant instead of those backscattered from the incident beam which carry the channeling contrast information. Since the crystals were required to be thin foils for the ECCI observation, the dislocation structures of deformed materials have mainly been investigated using TEM. Clarke et al [12] has referred to a possibility that the use of high brightness electron source such as a field-emission gun is desirable for the dislocation imaging in SEM. Morin et al [17] prepared the SEM system with the field-emission gun and succeeded in the dislocation imaging in a silicon bulk sample. Thereafter, the dislocation imaging by the ECCI with a bright electron source has been reported in bulk samples of several materials [18-22].

Recently, the ECCI method has been applied for the dislocation structure observation in fatigued materials [23-33]. According to these studies, it seems that the ECCI method —— which enables us to conduct the nondestructive dislocation imaging at large view —— deepen our knowledge about microscopic aspects of fatigue phenomena. In the present report, our recent results of the ECCI observation in fatigued copper single crystals and austenitic stainless steel polycrystals are intro-

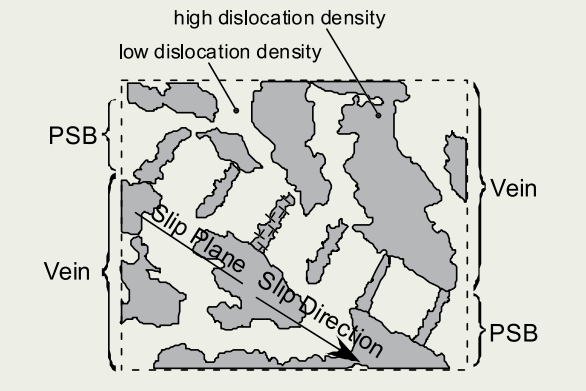

Fig. 1. Schematic illustration of dislocation structures of a fatigued crystal, viewed from a direction perpendicular to both slip direction and slip plane normal. The dislocation structure consists of the vein structure and the PSB having ladder-like dislocation wall structure along slip plane.

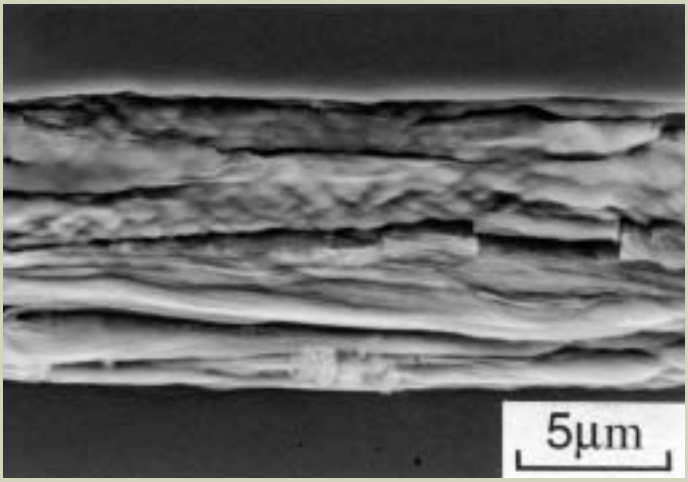

Fig. 2. SEM photograph showing fatigue cracks nucleated at a PSB which was formed in Fe-30%Cr alloy single crystal.

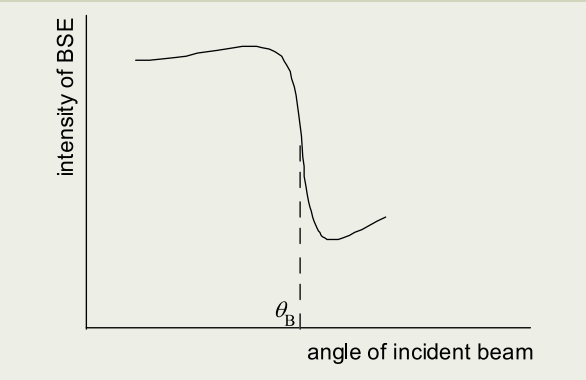

Fig. 3. Schematic illustration of the change in the backscattered electron intensity plotted against the incident beam direction. A doted line indicates the Bragg condition.

duced.

ECCI Observation of Microstructure in Fatigued Materials

Copper single crystals

In order to examine validity of the ECCI method, the authors attempted to observe the electron channeling images of fatigued copper single crystals whose dislocation structures were investigated well by TEM. Copper single crystals were grown by the Brigdman method using seed crystals having well-defined orientations, from a copper material of 99.99% purity. The single crystals were shaped to strip specimens of 6 mm gage length and 4 × 4 mm^2 cross-section. We prepared the specimens of different stress axes; i.e., [123], [111], [100] and [211] directions, in order to investigate the orientation dependence of the dislocation structures. The stress axis of [123] is a single-slip orientation, and the others are multiple slip orientations. The fatigue tests are carried out in air at room temperature. During the fatigue deformation, the plastic shear strain amplitude of the specimen was controlled to be 2×10^{-3}. After interruptions of the fatigue tests, the specimens were mechanically and electrolytically polished to obtain planar surface. Then, the specimen surfaces were observed by the ECCI method in JEOL JSM-6500F FE-SEM. The observations were performed at an acceleration voltage of 15 kV and a probe current of about 3.5 nA. In order to adjust the crystal orientation to achieve the Bragg condition, we utilized the electron-channeling pattern (ECP).

Figure 4 shows the comparison between a secondary electron image and an electron channeling contrast (ECC) image of exactly the same position after 1500 fatigue cycles. Owing to the electrolytic polishing before the observation, it is recognized in the secondary electron image that the specimen surface was very flat. On the other hand, a few band-like structures formed along the primary slip vector are visible in the ECC image. Being absent in the secondary electron image, the band-like images should be due to some structural changes inside the surface layer of the specimen.

The ECC images of the specimens having [123], [111], [100] and [211] stress axes are presented in **Fig. 5**. Figure 5(a) is a high magnification photograph of the band-like structure shown in Fig. 4. It is apparent that the band is composed from regularly-spaced walls whose average spacing was about 1.4 μm. This morphological feature is identical to the PSB which have been observed using conventional TEM [34, 35] by incorporating contrast reversal in the ECCI. (Bright contrast corresponds to the region of high dislocation density in the ECCI, as opposed to the TEM observation.) Hence, it can be concluded that the band-like structures detected by the ECCI were the PSBs formed at surface layer.

The ECCI observation at the single crystal having [211] axis revealed similar band-like structure formed along slip direction. However, the wall structure inside the band differed from that of the PSBs at the single-slip orientation. Although the dislocation walls of usual PSBs are arranged perpendicular to slip vector, the walls in the [211] specimen were perpendicular to stress axis. This kind of unusual wall arrangement has not been reported as far as we know, even in TEM observation.

The [111] and [100] specimens exhibited different dislocation structures considerably from the [123] specimen. In the [111] specimen, sinusoidal dislocation walls arranging perpendicular to tensile axis are clearly visible. This structure is analogous to the results of TEM observation in the specimen of the same orientation [36]. The dislocation structure of the [001] specimens observed by the ECCI is composed from two kinds of parallel dislocations walls. These walls are intersected each other almost at right angle. This special structure has also been reported in TEM observation [37] and is called "labyrinth structure".

Stainless steels

The ECCI can provide new insights into fatigue damage evaluation as mentioned above, owing to its nondestructive way of observation. From a viewpoint of practical applications, it seems important to confirm that evolution of dislocation structure in engineering materials such as stainless steel can be detected using the ECCI method. Hence, the ECCI observations were performed also on austenitic stainless steel polycrystals (Fe-19Ni-11Cr alloy) subjected to high-cycle fatigue.

The Fe-19Ni-11Cr alloy specimens were annealed at 1473 K for 1 hour. Resultant average grain size was approximately 120 μm and a yield stress at monotonic tensile test was 90 MPa. The stainless steel specimens were fatigued at constant stress amplitude of 140 MPa. The number of cycles to failure (fatigue life) at 140 MPa stress amplitude was found to be about 10^5 cycles.

Figure 6 shows the ECC images of the stainless steel fatigued until 5×10^4 cycles. This number of cycles corresponds to about half of the fatigue life. It is confirmed that the

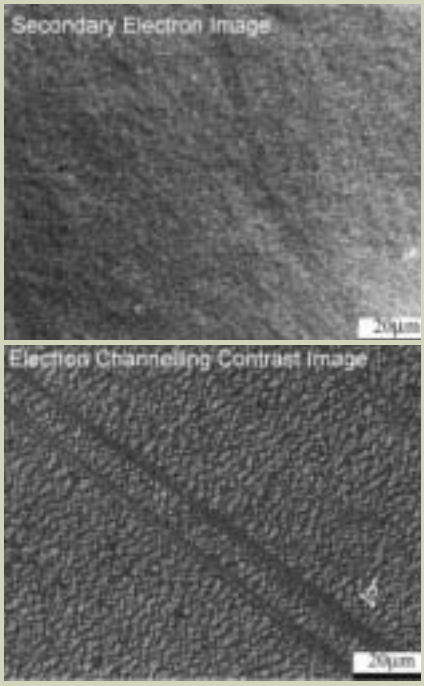

Fig. 4. Secondary electron and electron channeling contrast images of the same position of (11$\bar{1}$) crystal surface. The images are taken after 1500 cycles in the copper single crystal having [123] stress axis.

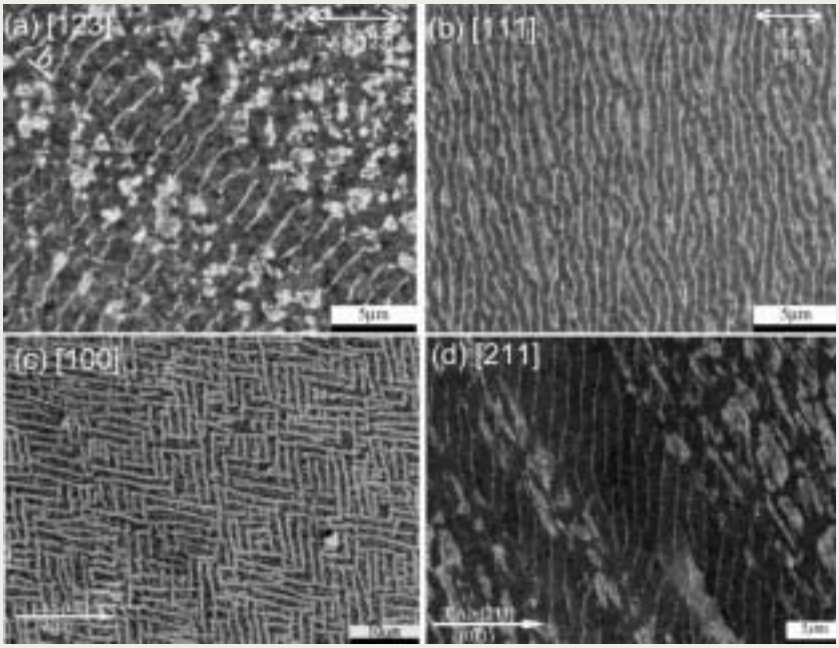

Fig. 5. Electron channeling contrast images in the fatigued copper single crystals of (a) [123] axis after 1500 cycles, (b) [111] axis after 4000 cycles, (c) [100] axis after 5000 cycles and (d) [211] axis after 5000 cycles. Observation planes are parallel to (11$\bar{1}$), (1$\bar{1}$0), (010) and (0$\bar{1}$1) for the [123], [111], [100] and [211] specimens, respectively.

ladder-like dislocation structures of PSBs formed at the fatigued stainless steel were visible in the ECC images, as well as in the copper single crystals. The dislocation walls had somewhat irregular shapes in comparison with that of the copper. Preferential formation of the PSBs along an annealing twin boundary was also recognized. The preferential PSB formation has been attributed to elastically incompatible stresses exerting locally along the twin boundary [38, 39].

One can consider that the most important advantage of the ECCI is the nondestructive observation of dislocation structure. The nondestructive observation enables us to estimate fatigue damage continuously even during fatigue process. This kind of the estimation would help us to understand dislocation processes leading to fatigue cracking, but has been impossible as long as the TEM is used. For this reason, the authors tried to show the change in dislocation structure of the same grain, by repeating cycle interruption and subsequent ECCI observation.

The dislocation structures of the same grain at 10^3, 10^4 and 10^5 cycles are presented in **Fig. 7**. It is recognized that the self-organization of dislocations already started even at 10^3 cycles. The ECC image at 10^4 cycles revealed that the dislocation walls changed its shape into irregular ones due to further fatigue cycling. At 10^5 cycles, the appearance of cell structure having slight misorientation was detected in the vicinity of grain boundary. It is likely that formation of the cell structure is attributed to secondary dislocations activated due to grain boundary incompatibility.

Summary

The dislocation structures developed in the fatigued copper and stainless steels were nondestructively observed in SEM by imaging the electron channeling contrast appropriately. Because the ECC images were almost identical to the TEM observation in the copper single crystals, it seems possible that the ECCI method will replace the conventional TEM technique, at least for the investigation of fatigued structures. It is also suggested that the ECCI is useful in estimating the fatigue damage of engineering materials such as stainless steel, from the result that the change in dislocation structure at the same position was successfully depicted.

Acknowledgement

We would like to thank A. Ono and T. Yanagihara (JEOL Ltd.) for helping a part of the ECCI observation. This research is supported by JSPS Grants-in-Aid for Scientific Research (15360372).

References

1. Suresh S.: *Fatigue of Materials, Second Edition*, Cambridge University Press, Cambridge, 39 (1998).
2. Basinski Z. S. and Basinski, S. J.: *Scripta Metall.*, **18**, 851 (1984).
3. Polak J.: *Mater. Sci. Eng.*, **74**, 85 (1985).
4. Hunsch A. and Neumann P.: *Acta Metall.*, **34**, 207 (1986).
5. Kaneko Y., Mimaki T. and Hashimoto S.: *Acta Mater.*, **47**, 165 (1999).
6. Wilkinson A. J. and Hirsch P. B.: *Micron*, **28**, 279 (1997).
7. Wells O. C.: *Scanning Electron Microscopy, Vol. I, IIT Research Institute* 747 (1977).
8. Coates D. G.: *Phil. Mag.*, **16**, 1179 (1967).
9. Humphrey C. J.: *Rep. Prog. Phys.*, **42**, 1825 (1979).
10. Hirsch P. B. and Humphreys C. J.: *Proc.the 3rd Annual Scanning Electron Microscopy Symposium, edited by O. Johari* , 449 (1970).
11. Booker G. R., Shaw A. M. B., Whealan M. J. and Hirsch P. B.: *Phil. Mag.*, **16**, 1185 (1967).
12. Clarke D. R. and Howie A.: *Phil. Mag.*, **24**, 959 (1971).
13. Wilkinson A. J., Anstis G. R., Czernuszka J. T., Long N. J. and Hirsch P. B.: *Phil. Mag. A*, **68**, 59 (1993).
14. Wilkinson A. J. and Hirsch P. B.: *Phil. Mag. A*, **72**, 81 (1995).
15. Clarke D. R.: *Phil. Mag.*, **24**, 973 (1971).
16. Stern R. M., Ichinokawa T., Takashima S. and Hashimoto H.: *Phil. Mag.*, **26**, 1495 (1972).
17. Morin P., Pitaval M., Besnard D. and Fontaine G.: *Phil. Mag.*, **40**, 511 (1979).
18. Joy D. C.: *Mater. Res. Soc. Symp. Proc.*, **183**, 199 (1990).
19. Czernuszka J. T., Long N. J., Boyes E. D. and Hirsch P. B.: *Phil. Mag. Lett.*, **62**, 227 (1990).
20. Czernuszka J. T., Long, N. J. Boyes, E. D. and Hirsch P. B.: *Mater. Res. Soc. Symp. Proc.*, **209**, 289 (1991).
21. Ng. B. -C., Simkin M. A. and Crimp M. A.: *Mater. Sci. Eng. A*, **A239-240**, 150 (1997).
22. Simkin B. A. and Crimp M. A.: *Ultramicroscopy*, **77**, 65 (1999).
23. Zauter R., Petry F., Bayerlein M., Sommer C., Christ H. -J. and Mughrabi H.: *Phil. Mag. A*, **66**, 425 (1992).
24. Zhai T., Martin J. W., Briggs G. A. D. and Wilkinson A. J.: *Acta Mater.*, **44**, 3477 (1996).
25. Schwab A., Bretschneider J., Buque C., Blochwitz C. and Holste C.: *Phil. Mag. Lett.*, **74**, 449 (1996).
26. Zhai T., Martin J. W., Briggs G. A. D. and Wilkinson A. J.: *Acta Mater.*, **44**, 3477 (1996).
27. Melisova D., Weiss B. and Stickler R.: *Scripta Mater.*, **36**, 1061 (1997).
28. Ahmed J., Wilkinson A. J. and Robbert S. G.: *Phil. Mag. Lett.*, **76**, 237 (1997).
29. Jia W. P., Li S. X., Wang Z. G., Li X. W. and Li G. Y.: *Acta Mater.*, **47**, 2165 (1999).
30. Zhang Z.F. and Wang Z. G.: *Phil. Mag. A*, **81**, 399 (2001).
31. Ahmed J., Wilkinson A. J. and Roberts S. G.: *Phil. Mag. A*, **81**, 1473 (2001).
32. Li S. X., Li X. W., Zhang Z. F., Wang Z. G. and Lu K.: *Phil. Mag. A*, **82**, 3129 (2002).
33. Kaneko Y. and Hashimoto S.: *J. Japan Inst. Metals*, **66**, 1297 (2002).(in Japanese)
34. Ackermann F., Kubin L. P., Lepinoux J. and Mughrabi H.: *Acta Metall.*, **32**, 715 (1984).
35. Ma Bao-Tong and Laird C.: *Mater. Sci. Eng. A*, **102**, 247 (1988).
36. Lepisto T., Kuokkala V. -T. and Kettunen P.: *Scripta Metall.*, **18**, 245 (1984).
37. Jin N. Y. and Winter A. T.: *Acta Metall.*, **32**, 1173 (1984).
38. Heinz A. and Neumann P.: *Acta Metall. Mater.*, **38**, 1933 (1990).
39. Kaneko Y., Hashimoto S. and Miura S.: *Phil. Mag. Lett.*, **72**, 297 (1994).

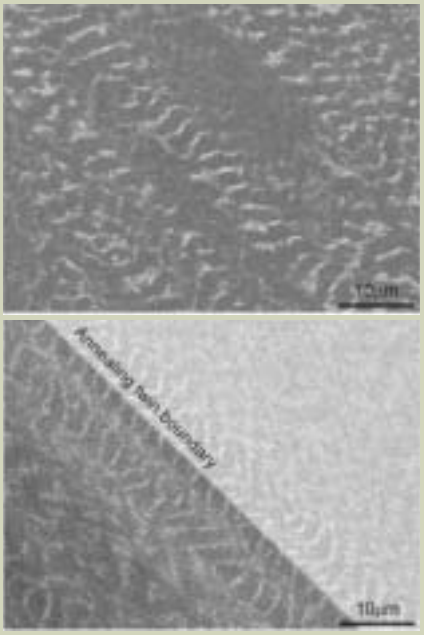

Fig. 6. Electron channeling contrast images showing PSBs developed in Fe-19Ni-11Cr alloy fatigued at constant stress amplitude of 140 MPa until 5×10^4 cycles.

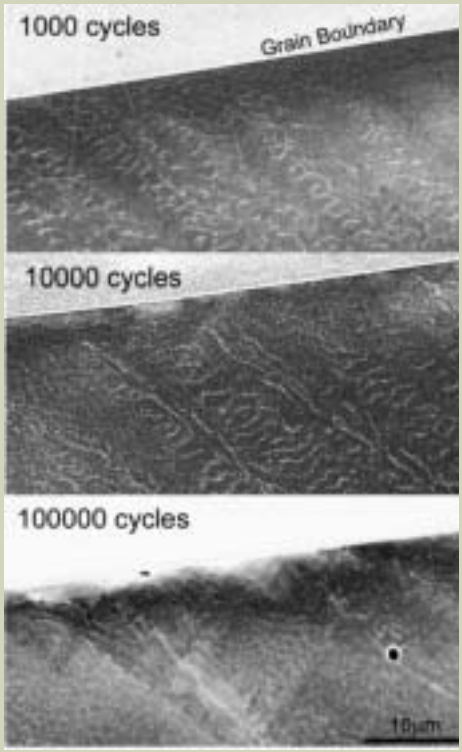

Fig. 7. Change in the electron channeling contrast images observed at same position in the Fe-19Ni-11Cr alloy fatigued at 140 MPa stress amplitude.

Protein NMR
–Ability of the JNM-ECA series–

Katsuo Asakura

Application & Research Center, JEOL Ltd.

Introduction

The structural analysis of protein by solution NMR completely differs from the structural analysis of natural products or synthetic organic compounds.

In the structural analysis of a natural product or a synthetic organic compound, analysis target is compound whose primary structure is completely unknown. However, the target of the solution NMR for protein is the protein whose primary structure is known. Purpose of the solution NMR for protein is the analysis of higher order structure. The structural analysis of the protein performed daily in many research institutes is not a complicate work in which many organic-chemists are afflicting their head in front of various spectra but a simple work which is performed mechanically. A machine may truly draw a final result. Thus, the structural analysis of protein by the solution NMR is not so complicated and so difficult as is generally thought.

On the other hand, although it is generally considered that an instrument that can perform protein NMR measurement is excellent, what is the reason for an NMR instrument to receive such an evaluation? In order to obtain the spectrum for performing analysis of the higher order structural of protein, an NMR spectrometer with high accuracy, high stability, and high sensitivity is needed.

The demand from such research of the protein NMR contributed greatly not only to the development of the NMR instrument, but also to the development of the NMR spectroscopy itself including an application to other fields in the last ten years.

It may not be an overstatement that this contribution produced the predominant position of the protein NMR in the current world of NMR.

The new spectrometer ECA of JEOL is fulfilling the performance required for various NMR measurements which are used for higher order structural analysis of protein. The spectrometer can demonstrate the ability for not only the protein NMR but also various measurements.

In this article, the ability of ECA is introduced through protein solution NMR while explaining the outline of fundamental protein solution NMR.

Solution NMR for Protein

First of all, the outline of protein solution NMR is explained here. The contents mentioned are about the very fundamental outline and may differ slightly from what is studied in the so-called “latest field”. The solution NMR of the protein described here is at the level where structural analysis is made as a routine.

Sample preparation

The protein sample which is used for the hither order structural analysis by NMR is in many cases, labeled with a stable isotope by biological synthesis.

Usually at first, a manifestation system of target protein is established by using Escherichia coli whose gene is manipulated, and is cultured in a culture medium in which carbon and nitrogen source labeled by a stable isotope (such as glucose whose entire carbon is labeled by ^{13}C and ammonium chloride whose all nitrogen is labeled by ^{15}N) are added. Then the protein whose entire carbon and nitrogen are labeled by the stable isotope can be obtained.

The obtained protein, which was labeled by a stable isotope is purified by LC, etc and then condensed by ultrafiltration, and then measured by NMR.

There are required cautions different from a general organic compound for sample preparation of biological samples. The conditions and notes required for the preparation of the protein solution sample used in usual NMR measurement are explained below.

● Handling of sample solution

The protein aqueous solution generally has a high viscosity and because it does not fall down inside of the sample tube once it adheres to glass surface, the detection quantity of the NMR measurement will decrease, and sensitivity will decrease sharply. Therefore, taking careful precautions are required for the handling of a precious sample in order to prevent any loss.

In order to smooth the surface of glass or plastic and to suppress the adhesion or the variance of a sample on the surface to a minimum, silicon coating is applied to the instrument used for sample preparation including the NMR sample tube. Moreover, in order to pour the sample solution into the NMR sample tube without touching the inner wall as much as possible, the long Pasteur pipette that reaches the bottom of the NMR sample tube is prepared (**Fig. 1**).

● Solvent

In order to maintain the higher order structure in the living body, the protein is measured in the aqueous solution in principle. However, if deuterated water is used as a solvent because a protein has many exchangeable amide protons, many information will be lost by carrying out deuterium substitution of the amide proton which serves as a key in the analysis of a spectrum. Thus, water (H_2O) is used for sample preparation, though usually about 10% of deuterated water is added in this water solution for NMR lock.

● Concentration

The concentration should be adjusted about 1mM (0.4mM-2mM). If solubility is high, the sample can be adjusted for the concentration, from 5mM to 10mM. But an association between molecules may occur in the solution if concentration is too high. Since line width of the signal may spread or higher order structure may change occasionally if association of molecules occurs, in order to prevent the unexpected analysis result caused by association, it is necessary to check the existence of association by comparing line shapes between the low and high concentration samples.

● pH

pH of the protein sample should be adjusted to about five to seven. Exchange speed of

Fig. 1. Pasteur pipette for sample preparation.

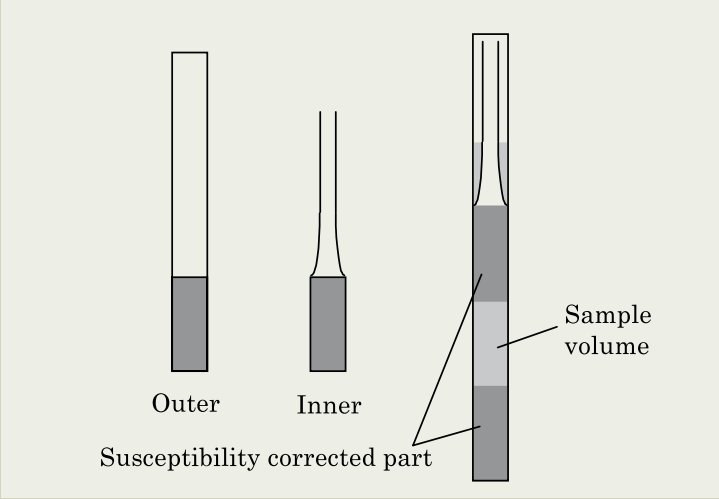

Fig. 2. Susceptibility corrected symmetrical micro cell.

exchangeable protons, such as an amide proton, is made slow by lowering pH. However, since the higher order structure may change when pH is low, it is necessary to confirm by the circular dichroism (CD) spectrum, etc.

● Buffer

In order to prevent the signal of buffer solution from hampering the spectrum analysis, the buffer solution without protons should be used. The typical examples are deuterated phosphoric acid buffer, deuterated acetic acid Buffer, and others.

● Temperature

In order to bring the temperature close to the temperature in the living body, it should be kept about 30 to 40°C. By setting a slightly higher temperature to reduce the viscosity of solution, the T_2 of the protein molecule lengthens. For this reason, generally a better spectrum is obtained at a slightly higher temperature.

● Other

A surface-active agent and a reduction agent may be added if necessary.

● Degas

If dissolved oxygen is contained in the sample solution, the relaxation time may become short due to paramagnetic relaxation, and the spectrum may cause the loss of sensitivity. Moreover, it may become the obstacle for detection of NOE correlation. In order to prevent these losses by the relaxation phenomenon, degas is performed to remove dissolved oxygen. Although the degas has been performed by methods of decompression or deoxidization by bubbling of inactive gas, since it is hard to use bubbling for a system in which a bubble tends to remain as described in the following section, and bubbling may cause inadequate deoxidizing, generally the decompressing method is used. In the decompressing method, degas is performed under weak decompression at about several mmHg. In this case, careful handling is needed, so that the sample solution may not be lost by the bumping.

● Bubble

Once the protein aqueous solution bubbles, removing bubbles will be very difficult. Therefore, at the time of sample preparation, it is necessary to be careful so that bubbles will not be made. Especially when you use a symmetrical micro cell with corrected magnetic susceptibility (**Fig. 2**), it is necessary to remove air bubbles completely because the static magnetic field is disturbed by the difference of the magnetic susceptibility between solution and air if air bubbles exist near the observation area. Moreover, air bubbles may be generated not only at the time of sample preparation but also by temperature change under NMR measurement, and that may decrease the resolution.

● Preservation

An azide is added to prevent the generation of mold. Although it is dependent on a kind of protein and the conditions of sample preparation, a protein sample can be used for several weeks if preserved in the refrigerator. At any rate, although the term may differ, since protein breaks gradually, it is necessary to observe it carefully.

Measurement Preparation

● Shim adjustment

If a sample preparation finishes and a measurement sample is inserted into the SCM, first, turn on the NMR lock and adjust the resolution. As usually the protein solution NMR is measured in the water solution in principle, it is necessary to eliminate a huge water signal which is several 10,000 times to several million times the ^{1}H concentration of the target protein. The signal of water has to be narrow enough in order to eliminate the signal of water selectively by the pulse technique until the multinuclear multi-dimension measuring method was introduced. At the same time, if the line shape of a signal is narrowed, the S/N improves and as a result, a good spectrum can be obtained. The S/N improvement is presently the main purpose for resolution adjustment, as the multinuclear multi-dimension measuring method is used frequently. In order to obtain a good spectrum, it is necessary to perform sufficient resolution adjustment for each measurement sample.

Rotating a sample tube is not likely in measurement of protein solution NMR. Therefore, in order to obtain a good spectrum, it is necessary that the resolution is adjusted firmly not only using the Z-axis but also using the X and Y-axis, and the higher order shim axis.

● Measuring pulse duration

Since a pulse width may change depending on the difference of salt concentration in the aqueous solution sample of the protein as described above, a pulse width must be measured for every measurement sample in principle. Since many RF pulses are arranged for the pulse sequence used with protein solution NMR, very small shift of a pulse duration influences quite greatly on the whole sequence. Therefore, before performing a higher order NMR measurement, the pulse duration is measured by using the signal of target protein, and a higher order NMR measurement is performed
using the measured value.

● Checking sample by NMR

The protein solution sample must be verified by NMR if there is a possibility of deterioration after being kept for a long term since sample preparation. However, because several thousand of the overlapped ^{1}H signals appear in the protein 1-dimensional NMR spectrum, not only analysis of the spectrum but also checking the sample using the spectrum cannot be carried out in most cases. Then, generally, the protein sample is checked using the two-dimensional NMR spectrum of ^{15}N-^{1}H HSQC . When the pattern of a signal in the HSQC spectrum is abnormal and the phase of the spectrum cannot be adjusted, the target protein is likely to be broken.

Spectrum Analysis (Assignment of Signal)

The most work in protein solution NMR is for the signal assignment of ^{1}H spectrum. The amino-acid sequence of protein's primary

structure is determined at manifestation of the protein, and there is no chance in which NMR is used for the analysis of amino-acid sequence. It is the higher order structure of protein that must be determined by NMR spectroscopy. Main purpose of NMR is to make higher order structure on the basis of the distance information of NOE. Therefore, in order to clear the position of NOE signal between protons in the protein, it is the main role in the many measurements to assign 1H signals from various measurement results. However, it is not so easy to assign the signal of the ^{1}H spectrum that consists of several thousand protons. The overlapped signals are dissociated by using 3 dimensional and 4 dimensional measurements and are assigned to known amino-acid sequences. The spectrum has a specific pattern for every amino acid residue, and the chemical shift or the spin-coupling constant has a characteristic law that makes it possible to assign the signals. Therefore, the automation to assign the protein spectrum is being progressed now. The features of the protein NMR spectrum are introduced below.

● Chemical shift

The ^{1}H chemical shift of protein is roughly limited for each environment of the amino acid (**Fig. 3**). That is, the proton signals of the amino-acid group are observed around the following chemical shift range, respectively.

- Amide proton: Near 8 ppm,
- Aromatic ring of side chain: Near 7 ppm,
- Proton of α position: Near 4 ppm
- Proton of β position: Near 2-3 ppm
- Methyl-group: Near 1 ppm

There is the same correlation in the chemical shift of ^{13}C. Selective excitation for each carbon area by dealing with the carbon of α or β position and carbonyl carbon just like other nuclides is utilized in the various measuring methods for an assignment in ^{13}C spectrum. Although it is not directly related to the assignment of amino-acid sequence, change of the chemical shift originating in the higher order structure can be seen. For example, the signal of the proton at α position shifts to the high magnetic field in an α-helix structure, and it shifts to low magnetic field in a β-sheet structure. In addition, a proton signal may shift about ± 1 ppm by the position related with the aromatic ring of a side chain. Moreover, in a protein including metallic bond, a quite big shift can be observed at the part bonded with metal.

● Homonuclear spin-coupling

Since the amino acid that constitutes protein is connected by a peptide bond, the spin coupling between ^{1}H-^{1}H is divided by the carbonyl group, and the spin coupling between ^{1}H-^{1}H is restricted in the same amino-acid residue. Therefore, the pattern of the spin coupling between ^{1}H-^{1}H (**Fig.4**) is characterized for every kind of amino acid, and the amino acid is identified using this fact. Moreover, dihedral angle φ derived from the spin-coupling constant between the proton of an α position and an amide proton $^{3}J_{H\alpha HN}$ is useful to determine secondary structure of the main chain.

● Heteronuclear spin-coupling

The spin-coupling constants other than ^{1}H-^{1}H coupling related to the main chain are almost fixed as shown in **Fig. 5**, and they are used for selection of the pathway of magnetization transfer. Each signal is assigned by dividing the overlapped ^{1}H signal into the chemical shifts of ^{13}C or ^{15}N using the multi-dimension NMR spectrum. Thus, the chemical shift and the spin-coupling constant are utilized in various multinuclear multi-dimension measurements for the assignment of signals.

● NOE

NOE correlation is used for higher order structural analysis. Furthermore, ^{1}H homonuclear NOE between an amide proton and a proton of an α position which sandwiched the carbonyl group shows that the two protons belong to the amino-acid residue which adjoined each other through the peptide bond, and the ^{1}H homonuclear NOE is used for assignment of the amino-acid sequence by ^{1}H homonuclear experiment.

This technique is called Sequence-specific resonance assignments method combining with the classification information of the amino acid determined on the basis of the spin coupling or the chemical shift (**Fig. 6**).

Higher Order Structural Analysis

If assignment of the signal is completed, you can carry out the higher order structural analysis. The higher order structure of protein consist of the secondary structure like an α-helix structure or a β-sheet structure whose amino-acid sequence forms with stereo specific regularity in protein, tertiary structure where some secondary structures have been arranged spatially, and the quaternary structure where the domain built with the three-dimensional structure has been arranged spatially. The clarification of the higher order structure is the purpose of structural analysis in a protein solution NMR measurement.

As described above, the amino-acid sequence's primary structure of protein is known, and the protein structure constructed by entangling known polypeptide chain is solved using the information that can be

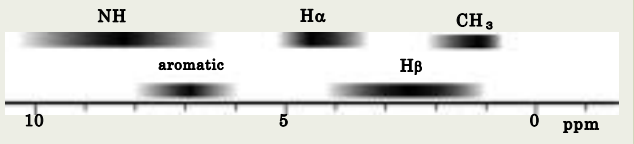

Fig. 3. Typical chemical shift of ^{1}H in protein.

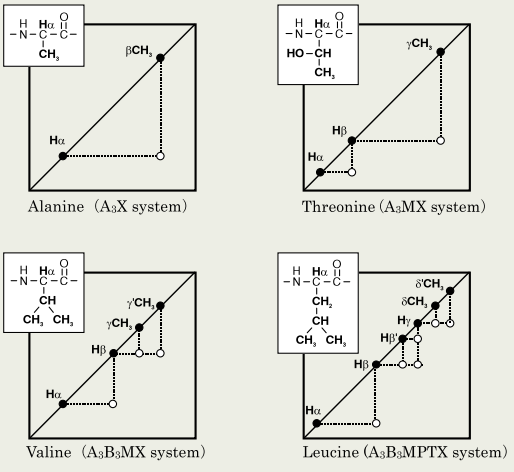

Fig. 4. Example of the spin coupling network by COSY of the ^{1}H spin system of amino acids.

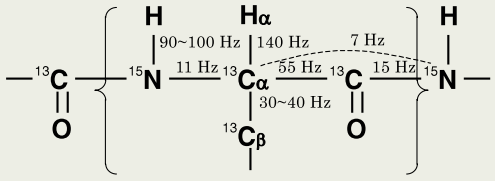

Fig. 5. Typical spin-coupling constant in the amino acid residue.

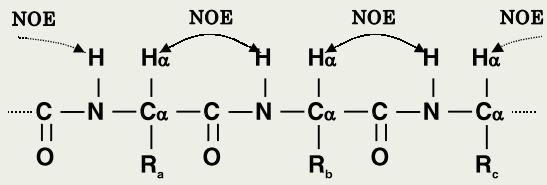

Fig. 6. The method of the sequence specific chain assignment.

Signal intensity of NOE	Maximum value of distance
Small	≦5Å
Middle	≦4Å
Large	≦3Å

Table 1. Signal intensity of the NOE and roughly estimated distance between atoms.

acquired from NMR.

In this measurement, the structure optimization calculation algorithm is used such as the distance geometry method and restrained molecular-dynamics method with restraint conditions. In any case, a number of NOE signals including distance information are collected from NMR spectrum as much as possible. If the information of NOE signals are given to the calculation program as the parameters, the computer will estimate the higher order structure where a computer sufficiently demonstrates the capability. Work of researcher is judging whether the structure estimated by the computer is right or not, and considering the interpretation to the structure.

● Distance information of NOE signal

Usually, the strength of NOE is in inverse proportion to the 6th power of distance between protons. Therefore, if quantitative analysis of the NOE is carried out, an exact distance between atoms can be found. However, the cross relaxation caused by NOE phenomenon has many relaxation paths other than the direct cross relaxation path between two nuclei. Therefore, NOE is classified into about 3 stages of "large NOE", "middle NOE ", and "small NOE", without exact analysis, and it is considered as the restriction conditions for the maximum value of the distance between atoms (**Table 1**).

● Distance geometry method

A set of the distance information and a dihedral angle gives spatial position information of the atoms, and the technique to induce structure on the basis of the information is the distance geometry method. Usually, a structure calculation is progressed by fixing the bond length of a covalent bond and a bond angle to the standard value of a common protein, and using a dihedral angle as a variable. Some structures converged in the direction which fulfills the restraint conditions of the distance of NOE are taken out, and the structure thought as the most suitable is made into the last structure.

Although the calculation is also quick and the load to the computer is also small since this technique has few variables, it is difficult to converge on true structure since a structural change is restricted by atomic contact (the passing through of covalent bonds is not possible).

Therefore this method is used to search an initial structure for the molecular-dynamics method as described below.

● Restrained molecular-dynamics method

Molecular Dynamics method is a technique generally used in order to carry out the simulation of the molecular motion. This method vibrates a molecule virtually and optimizes the structure. The molecular dynamics method with additional restraint condition of distance from NOE as a potential, is called molecular dynamics method, and used in the solution NMR of protein. Since this method uses Cartesian coordinate as position information, and has many variable parameters, a lot of calculations are necessary, and the load to a computer is also large. However, at present, since calculation time is shortened by fast progress of the calculation capability of a computer, this technique is frequently used.

● Simulated annealing method

As one of the techniques of the molecular-dynamics calculation, there is the simulated annealing method. This calculation technique is mainly used for the protein structure optimization calculation.

The simulated annealing method differs from ordinary molecular-dynamics calculation. In this method, the molecular motion is intensified by setting the parameter that contributes to a covalent bond weak in the initial stage of a calculation and raising the temperature of the system abruptly in the initial stage of a calculation. After that, while lowering the temperature of the system gradually and making the molecular motion slow, each parameter is strengthened and the structure is converged. This method can prevent the convergence to pseudo-structure by preventing a structural change caused by atomic contact.

Ability of ECA

Adopting multi-sequencer system

The multi-sequencer system, which is an effective system in the multi-channel measurement used abundantly in protein NMR, is adopted in the ECA spectrometer (**Fig. 7**). A multi-sequencer system points out the parallel processing mechanism of the pulse output by two or more sequencer units. The sequencer unit controls the pulse-output timing and the high-speed parameter setting. Two or more sequencer units independently control the pulse of each channel including PFG. The unit called master sequencer can flexibly control all the complicated pulse programs at a high speed including the pulse sequence for a protein NMR measurement by controlling the output timing of each sequencer.

Direct Digital Synthesizer

Each sequencer unit is individually connected with the DDS (Direct Digital Synthesizer) daughter card which generates the digital intermediate frequency (IF), and controls the digital output. The DDS daughter

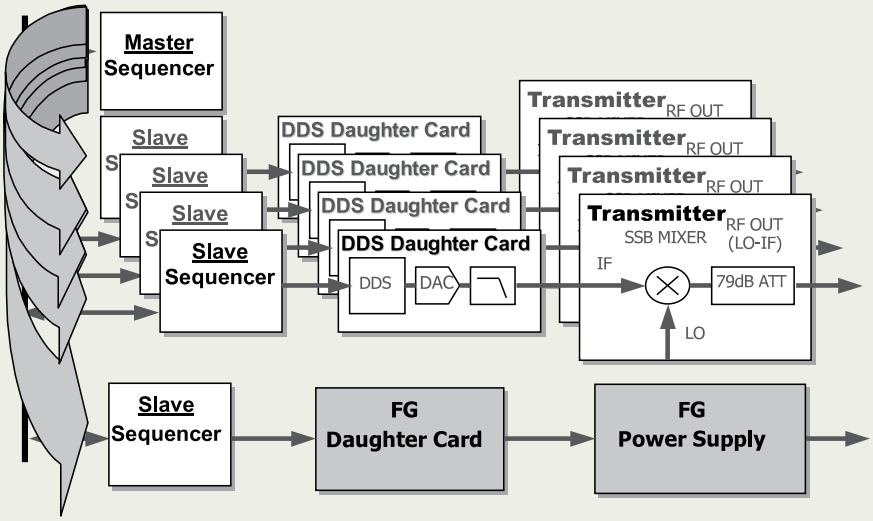

Fig. 7. Multi-sequencer system.

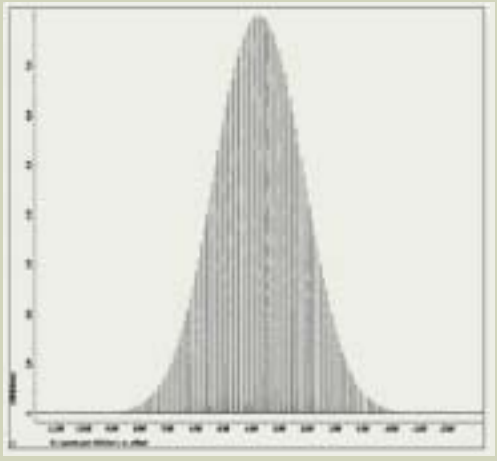

Fig. 8. Selective excitation profile by Gauss pulse.

card precisely controls the offset frequency, the phase and the amplitude of RF transmitted frequency at a high speed. Since the DDS daughter card digitally modulates IF, the pulse shape of a selective excitation pulse can also be outputted with very high accuracy. Moreover, since the RF modulation of a selective excitation pulse is controlled by calculation value for the formula, an error against the ideal waveform can be suppressed to a minimum by comparison with the list of format.

The excitation profile of the Gauss pulse with 1ms pulse duration is shown in **Fig. 8**. It shows that the selective excitation is carried out correctly.

Long term stability

The protein NMR measurement is basically a higher order measurement, and almost measurements require a very long-term period. Several days are required for one measurement on general conditions, in some cases one week or so is required. Therefore, it is necessary to keep the spectrum stability in the long term by keeping the stability of RF and controlling the temperature.

The ECA spectrometer has realized very high stability by optimizing all the circuits related to spectrum stability. Very good RF stability is shown in the 30 degrees pulse stability test (**Fig. 9a**). Very excellent stability is also shown in the stability test by hetero spin echo experiment (**Fig. 9b**).

Protein spectra of ECA

The ECA spectrometer can be applied to measurement of the protein solution NMR. Here, a part of pulse sequence, which is provided as standard for the solution NMR of protein in the ECA, is introduced with data shown. All the spectra are measured for ubiqitin labeled ^{13}C and ^{15}N by using the ECA600 spectrometer (**Fig. 10a**). Although the pulse sequence diagram is shown for each sequence, the contents of the pulse sequence provided as standard may change without a prior notice.

^{15}N-^{1}H HSQC

^{15}N-^{1}H HSQC experiment is to obtain the correlation of ^{15}N and a proton. A cross peak appears in the position in which the chemical shift of the amide proton directly bonded with ^{15}N and the chemical shift of ^{15}N intersect (**Fig. 10b**).

^{13}C-^{1}H HSQC

^{13}C-^{1}H HSQC is the experiment for obtaining the correlation of ^{13}C and ^{1}H. A cross peak appears in the position in which the chemical shift of ^{1}H directly bonded with ^{13}C and the chemical shift of ^{13}C is crossed (**Figs. 11a and 11b**).

HNCO

HNCO is a 3D measurement for obtaining the correlation between an amide proton of the main chain and a carbonyl carbon of the peptide bond. In the two dimensional spectrum sliced on the chemical shift of ^{15}N, the cross peak between an amide proton of the specified amino acid and a carbonyl carbon in the same peptide bond appear (**Figs. 12a to 12e**).

HNCA

HNCA is a 3D measurement for obtaining the correlation between an amide proton and the carbons of α position. In the two-dimensional spectrum sliced on the chemical shift of ^{15}N, the correlation signals between the amide proton of the specific amino acid and both α-carbons within the same amino acid residue appears; also, in adjacent amino acid residue connected with the same peptide bond appear as the cross peaks (**Figs. 13a to 13e**).

HN(CO)CA

HN(CO)CA is a 3D measurement for obtaining the correlation between an amide proton and the α-carbon of adjacent amino acid residue.

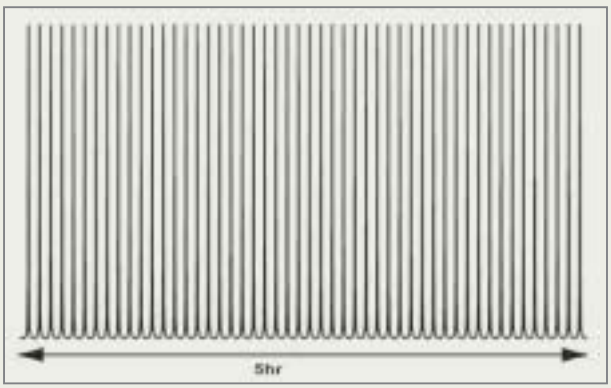

(a) 30deg pulse stability test, Standard deviation : 0.09%.

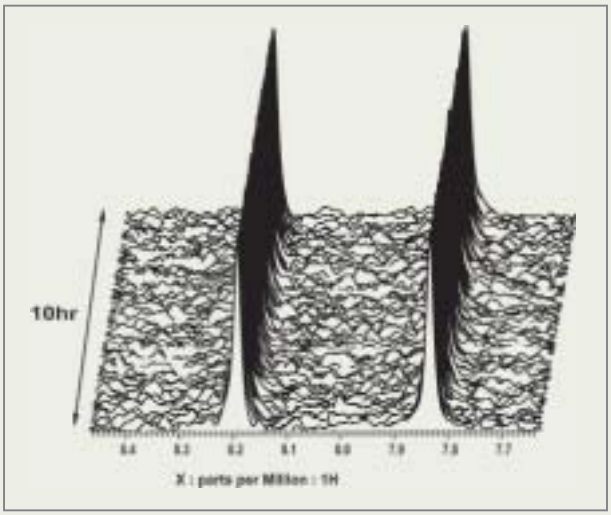

(b) Hetero spin echo spectrum of 1% $CHCl_3$.

Fig. 9

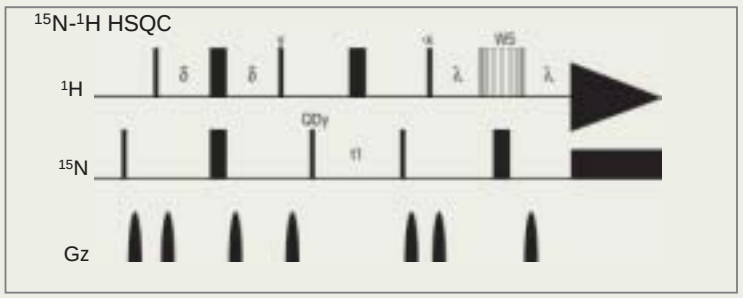

(a) Pulse sequence of ^{15}N-^{1}H HSQC.

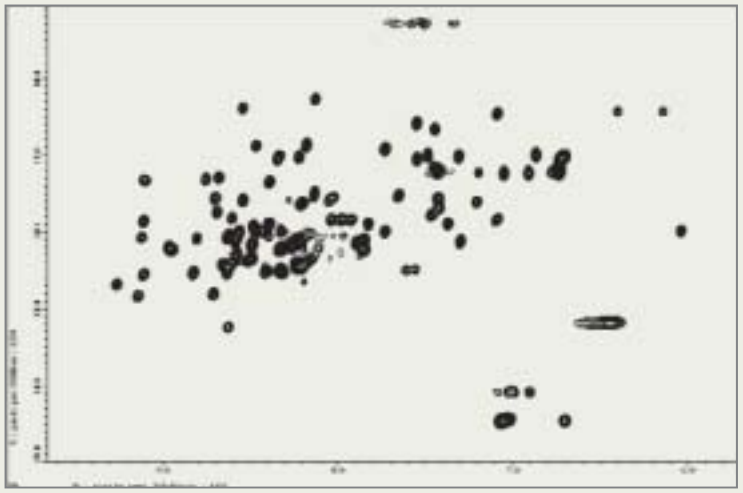

(b) ^{15}N-^{1}H HSQC spectrum.

Fig. 10

Since the magnetization transfer through carbonyl carbon differing from HNCA, the correlation signal with the α-carbon within the same amino acid residue does not appear.

In the 2D spectrum sliced on the chemical shift of ^{15}N, the correlation signal between the amide proton of the specific amino acid and the α-carbon in the adjacent amino acid residue connected by the peptide bond belonging to the amide appears as a cross peak (**Figs. 14a to 14e**).

HNCACB

HNCACB is a 3D experiment for obtaining the correlation between an amide proton and the carbon of α position and β position. In the two-dimensional spectrum sliced on the chemical shift of ^{15}N, the correlation signal between the amide proton of the specific amino acid and both the α-carbon and β-carbon within the same amino residue appear, and also the adjacent amino residue connected by the peptide bond belonging to the amide proton appear as the cross peaks. Moreover, the signal phase reverses by α-carbon and β-carbon (**Figs. 15a to 15e**).

CBCA(CO)NH

CBCA(CO)NH is a 3D measurement for obtaining the correlation between an amide proton and the carbon of α and β positions.

Since the magnetization transfers via carbonyl carbon differing from HNCACB, a correlation signal within the same residue does not appear. In the two-dimensional spectrum sliced on the chemical shift of ^{15}N, the correlation signal between the amide proton of the specific amino acid and α and β carbon in the adjacent amino acid residue appear as the cross peaks (**Figs. 16a to 16e**).

HBHA(CBCACO)NH

HBHA(CBCACO)NH is a 3D measurement for obtaining the correlation between an amide proton and the proton of α and β positions. Same as CBCA(CO)NH, since the magnetization transfers via carbonyl carbon, a correlation signal between protons within the same amino acid residue does not appear. In the two-dimensional spectrum sliced on the chemical shift of ^{15}N, the correlation signals between the amide proton of the specific amino acid and α and β proton in the adjacent amino acid residue appear as the cross peaks (**Figs. 17a to 17e**).

^{15}N-edited NOESY

^{15}N-edited NOESY is a 3D measurement for obtaining NOE correlation between an amide proton and the proton which is in near space.

In the two-dimensional spectrum sliced on the chemical shift of ^{15}N, the correlation signals between the amide proton of the specific amino acid and the protons that are closely spaced appear as the cross peaks (**Figs. 18a to 18d**).

HCCH-TOCSY

HCCH-TOCSY is a 3D measurement for obtaining the spin network between the protons of a side chain.

In the two-dimensional spectrum sliced at the chemical shift of ^{13}C, the correlation signals between the protons which is bonded with the carbon directly and the protons in the same amino acid residue appear as the cross peaks (**Figs. 19a to 19e**).

Conclusion

Although it tends to be thought that the higher order structural analysis of a protein by solution NMR is a very difficult field for an inexperienced person, both measurement and analysis of the spectrum is not so difficult at present. Especially automation of analysis is increasingly advancing; completely automated analysis of protein that consists of a certain number of amino-acid residues will be performed in the near future. The structural-analysis technique by the solution NMR of protein, which is explained in this article, is already established as a routine-work system, and is used as a stereo-structure analysis of new protein at laboratories worldwide. Of course in the future, much advanced research techniques on protein are required, such as the evolution to dynamics of protein, the structural-analysis technique for the protein having very large molecular weight, and a measurement in a certain solid state being applied to the protein film.

Therefore, high-level requirements for the NMR instrument will increase. By solving these requirements with cooperation among industry, university and government, the NMR spectroscopy will be further developed, and possibly new research fields will be created.

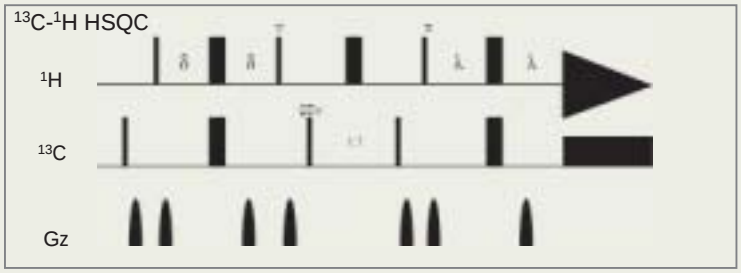

(a) Pulse sequence of ^{13}C-^{1}H HSQC.

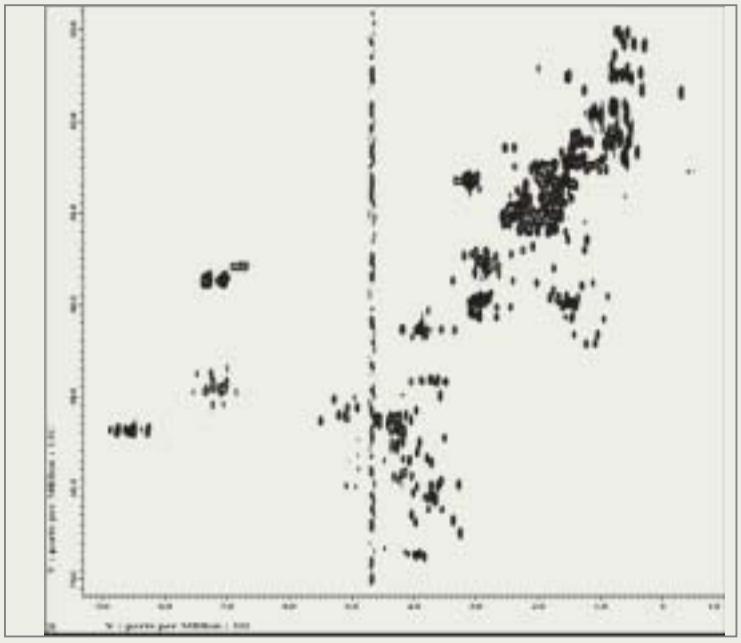

(b) ^{13}C-^{1}H HSQC spectrum.

Fig. 11

References

1. Kurt Wuthrich, " NMR of proteins and nucleic acids" John Wiley & Sons, New York, (1986)
2. Yoji Arata, "Protein NMR: Analysis Interpretation and Evaluation of Structure Data ", Kyoritsu Shuppan, Tokyo (1996)
3. Yoji Arata, "the Book of NMR", Maruzen, Tokyo, (2000)
4. Nobuaki Nemoto, Takuya Yoshida, Yuji Kobayashi, Science and Industry, 69 (10), 419-425.5 (1995)
5. Nobuaki Nemoto, Takuya Yoshida, Yuji Kobayashi, Science and Industry, 70 (2), 48-55.6 (1996)
6. M. Sattler, J. Schleucher, C. Griesinger, Progr. NMR Spectrosc.,34 and 93-158. (1999)
7. J. Cavanagh, W. J.Fairbrother , A. G.Palmer III and N. J. Skelton "Protein NMR Spectroscopy: Principles and Practice" Academic Press. New York (1995)
8. T. L. James and N. J. Oppenheimer (eds.), "Methods in Enzymology", Vol.239, Academic Press., New York (1994)

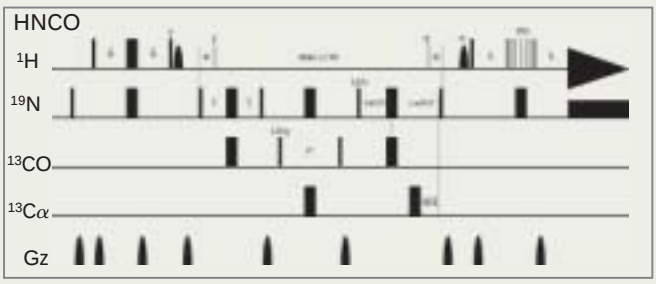

(a) Pulse sequence of HNCO.

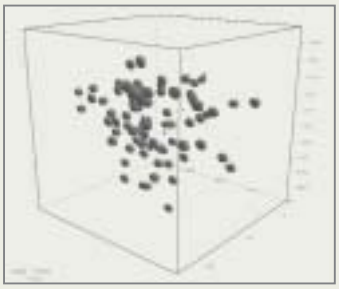

(b) 3D cubic display of HNCO spectrum.

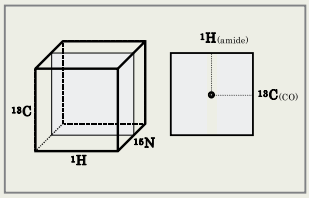

(c) Schematic diagram of HNCO spectrum.

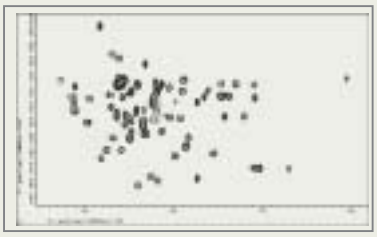

(d)Projection of HNCO spectrum to the XY plane.

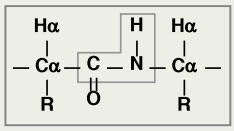

(e) Spin system related to the measurement.

Fig. 12

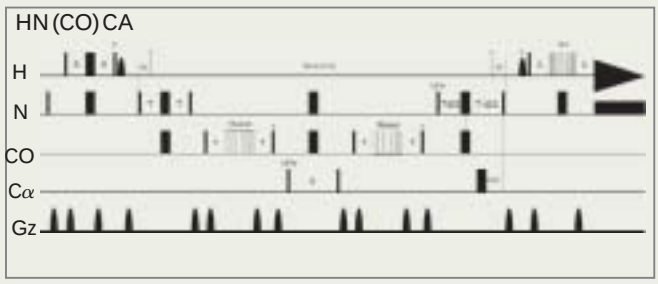

(a) Pulse sequence of HN(CO)CA.

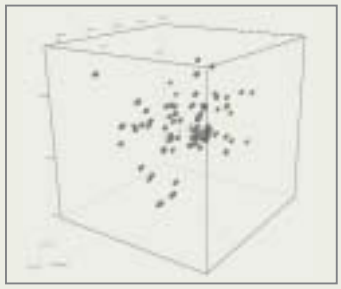

(b) 3D cubic display of HN(CO)CA spectrum.

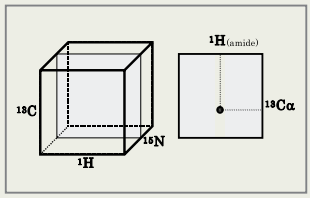

(c) Schematic diagram of HN(CO)CA spectrum.

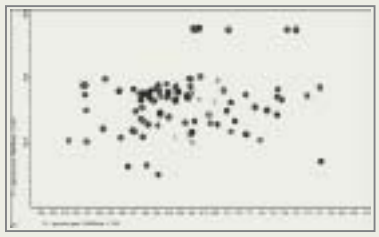

(d)Projection of HN(CO)CA spectrum to the XY plane.

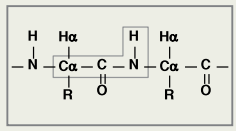

(e) Spin system related to the measurement.

Fig. 14

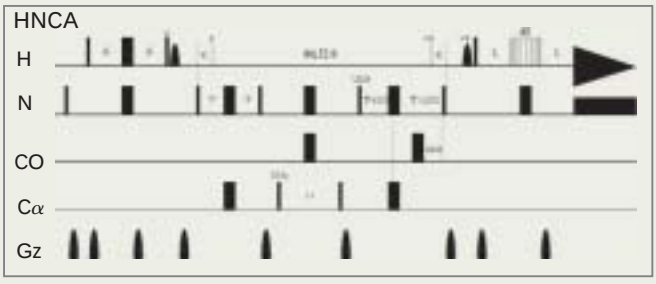

(a) Pulse sequence of HNCA.

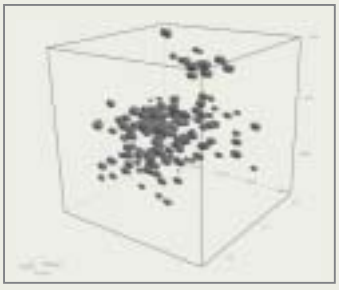

(b) 3D cubic display of HNCA spectrum.

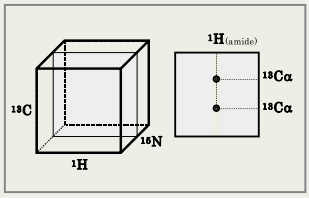

(c) Schematic display of 3D HNCA spectrum.

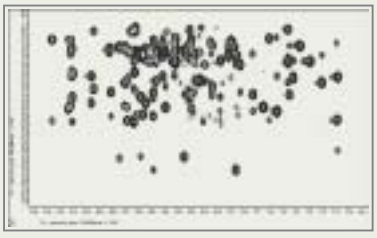

(d)Projection of HNCA spectrum to the XY plane.

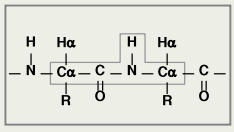

(e) Spin system related to the measurement.

Fig. 13

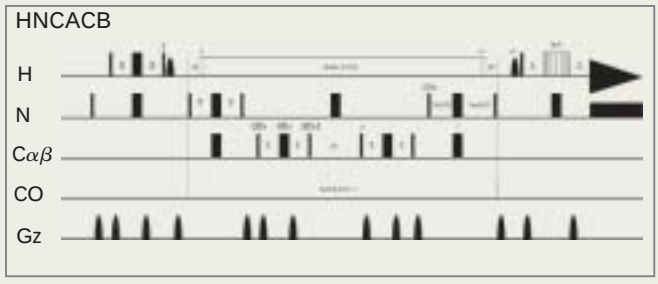

(a) Pulse sequence of HNCACB.

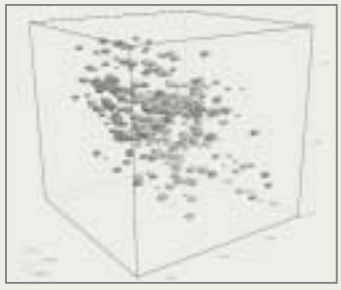

(b) 3D cubic display of HNCACB spectrum.

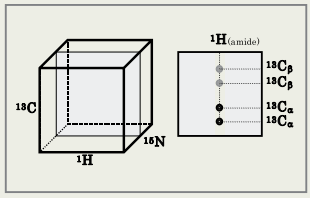

(c) Schematic diagram of HNCACB spectrum.

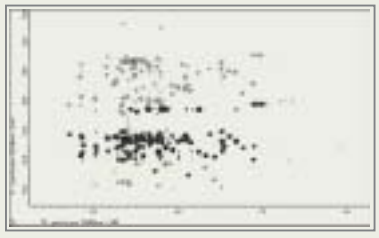

(d)Summation of HNCACB spectrum to the XY plane.

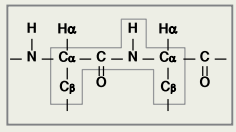

(e) Spin system related to the measurement.

Fig. 15

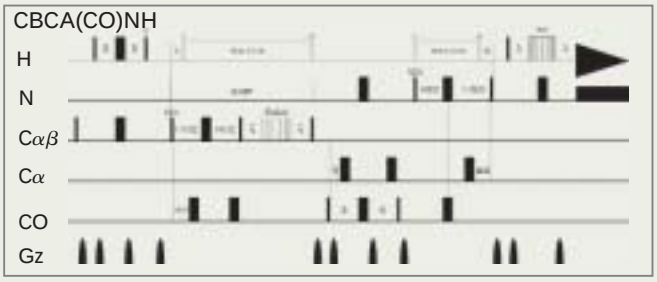

(a) Pulse sequence of CBCA(CO)NH.

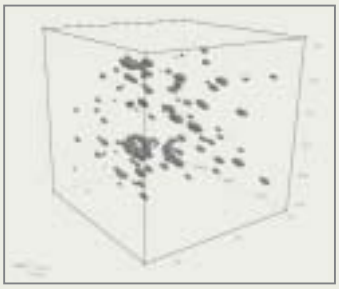

(b) 3D cubic display of CBCA(CO)NH spectrum.

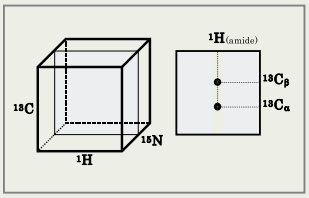

(c) Schematic diagram of CBCA(CO)NH spectrum.

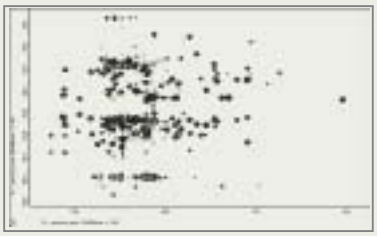

(d)Projection of CBCA(CO)NH spectrum to the XY plane.

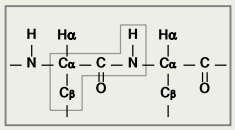

(e) Spin system related to the measurement.

Fig. 16

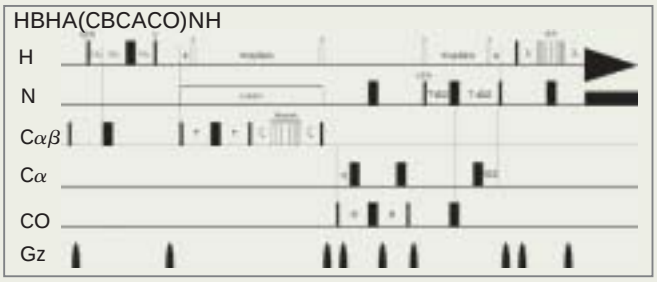

(a) Pulse sequence of HBHA(CBCACO)NH.

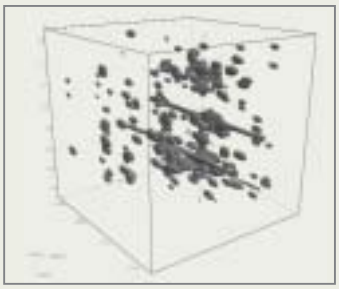

(b) 3D cubic display of HBHA(CBCACO)NH spectrum.

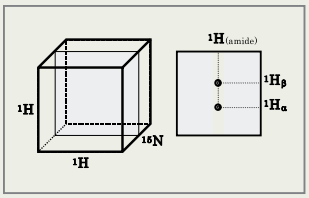

(c) Schematic diagram of HBHA(CBCACO)NH spectrum.

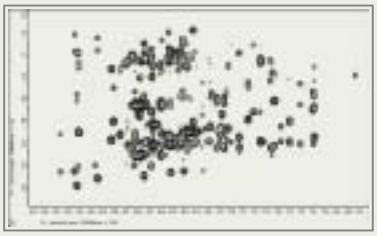

(d)Projection of HBHA(CBCACO)NH spectrum to the XY plane.

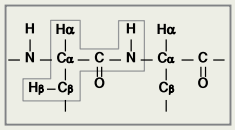

(e) Spin system related to the measurement.

Fig. 17

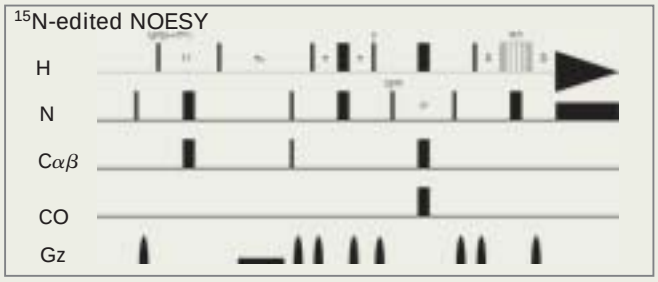

(a) Pulse sequence of ^{15}N-edited NOESY.

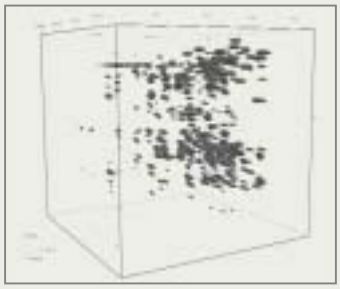

(b) 3D cubic display of ^{15}N-edited NOESY spectrum.

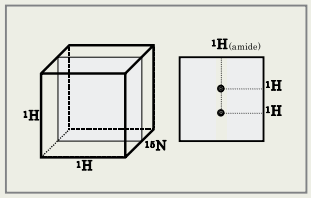

(c) Schematic diagram of ^{15}N-edited NOESY spectrum.

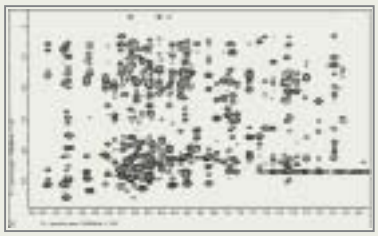

(d)Projection of ^{15}N-edited NOESY spectrum to the XY plane.

Fig. 18

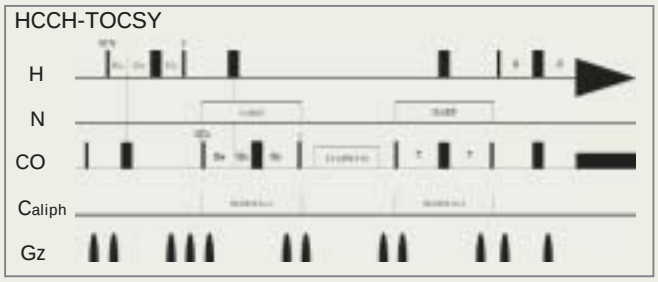

(a) Pulse sequence of HCCH-TOCSY.

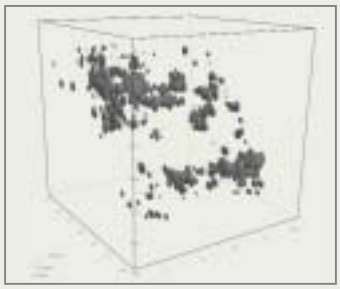

(b) 3D cubic display of HCCH-TOCSY spectrum.

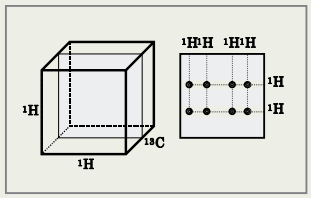

(c) Schematic diagram of HCCH-TOCSY spectrum.

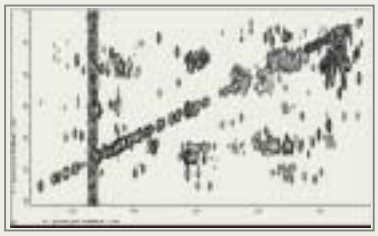

(d)Projection of HCCH-TOCSY spectrum to the XY plane.

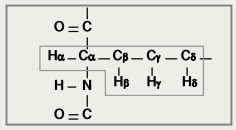

(e) Spin system related to the measurement.

Fig. 19

Development of the JBX-3030MV Mask Making E-Beam Lithography System

Yasutoshi Nakagawa, Tadashi Komagata, Yuichi Kawase and Nobuo Gotoh

Semiconductor Equipment Division, JEOL Ltd.

An advanced electron beam lithography system for reticles production has been developed for the 90 nm technology node. The JBX-3030MV features a variable shaped beam, 50kV accelerating voltage, and a step-and-repeat stage. The tool incorporates new technologies, including a high resolution, high current density electron optical system, a triangle beam system, a high speed electrostatic beam deflection unit, a high accuracy PEC (proximity effect correction) system, and a glass-in glass-out material handling unit.

The system achieves a global CD (critical dimension) accuracy of 4 nm (3σ), and a placement accuracy of ±8 nm, while maintaining an exposure speed up to 3 times faster than the previous model.

Introduction

According to the 2002 ITRS (International Technology Roadmap for Semiconductors) Update, reticles for the 100 to 90 nm technology node require pattern accuracies of 21 to 19 nm (image placement) and 8 to 4.2 nm (CD uniformity). E-beam mask writers need to achieve this strict CD uniformity without compromising the writing speed. This is a significant engineering challenge in designing the system. JEOL has developed a new electron beam mask writing system, JBX-3030MV, needed for production of masks for 100 to 90 nm technology node through substantial improvements to the existing JBX-9000MV[1] series. The improvements incorporated and the results of evaluation will be introduced in this paper.

System Concept and Improvement

Target Specifications

Tables 1 and **2** show the performance specifications and system specifications of the JBX-3030MV. The new system maintains some of the features of the JBX-9000MV series, including a variable shaped beam, 50 kV accelerating voltage, a step-and-repeat stage system.

System Configuration

Figure 1 is the system block diagram of the JBX-3030MV, outlining improvements incorporated in the 9000MV series to support higher accuracies and larger data volume. These improvements will be discussed in the sections below.

Improvements

Electron Optical System

Figure 2 is a ray diagram of the JBX-3030MV electron optical system. The column incorporates an LaB_6 electron gun for 50 kV accelerating voltage, 4 stage electromagnetic lens, rotation lens, blanking electrode, beam shaping deflector, beam positioning deflector, dynamic focus lens, and dynamic astigmatism corrector.

The system has a sub deflector in addition to the single stage beam positioning deflector to enhance the shot cycle speed. As a result, the beam OFF time per shot was reduced to 1/3 of the previous model. This beam OFF time is expected to be reduced further when the DAC/AMP is improved. In addition, the electron optical system was improved to speed up the exposure process, increasing the current density to 20 A/cm² from 10 A/cm². A 45 degree triangle beam shaping system was also incorporated to reduce the number of shots needed to write 45 degree oblique lines.

Improved PEC

The proximity effect correction system of the previous system is designed to map accumulated energy distribution when the pattern is written with a constant shot time and correct the shot time per pattern to cancel the proximity effect per micro area (partition). It does not consider that the backscattered electron energy intensity in a micro area changes according to the shot time correction applied to peripheral areas other than the target micro area. Thus, the proximity effect cannot be fully corrected when the accumulated energy intensity in the area changes due to shot time correction in peripheral areas resulting from proximity correction. We improved the proximity effect correction system by recalculating the accumulated energy intensity of backscattered electrons according to the shot time of the exposed pattern to which proximity correction has been

● CD Accuracy	
CD Uniformity within Plate	8 nm (3σ)
CD Linearity	15 nm p-p
● Field Stitching Accuracy	±10 nm
● Position Accuracy	±12 nm

Note: Field shift writing performed twice

Table 1. Performance specifications of JBX-3030MV.

Beam shape	Variable
Beam deflection	Vector
Stage movement	Step and Repeat
Standard mask size	152 mm
Accelerating voltage	50 kV
Current density	20 A/cm²
Max. beam size	1 um
Field size	1 mm
Beam grid increment	1 nm

Table 2. System specifications of JBX-3030MV.

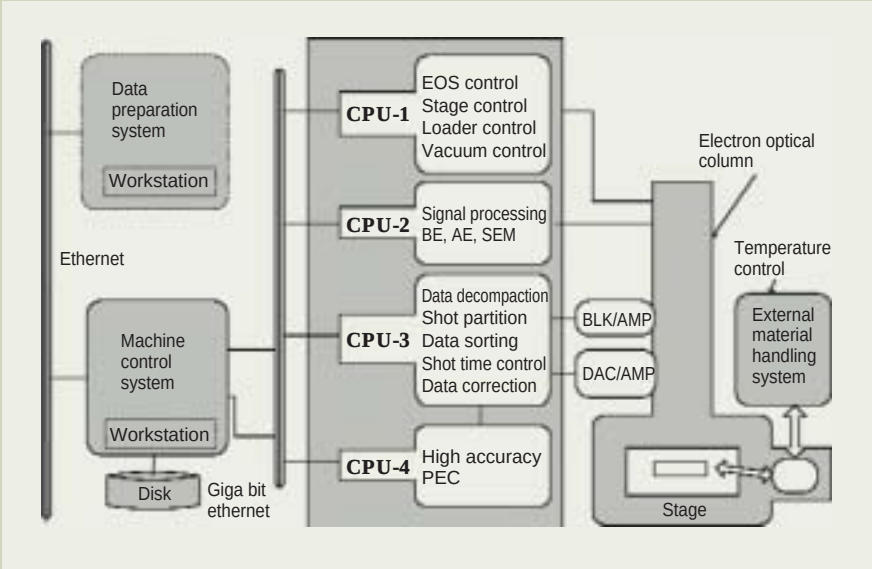

Fig. 1. Block diagram of JBX-3030MV.

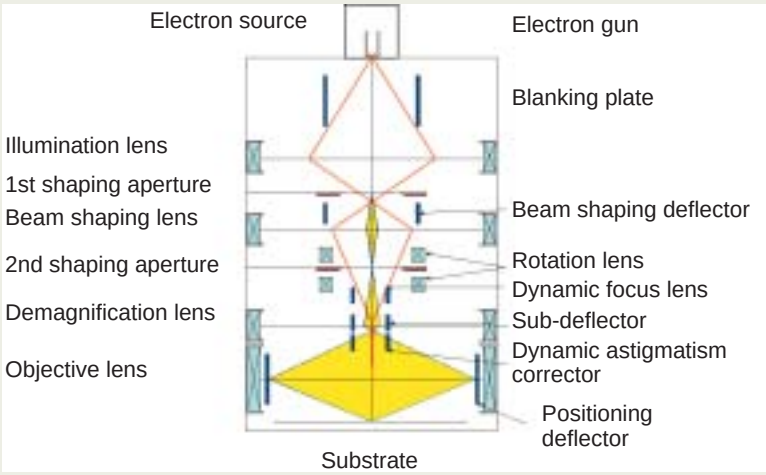

Fig. 2. Electron optical system.

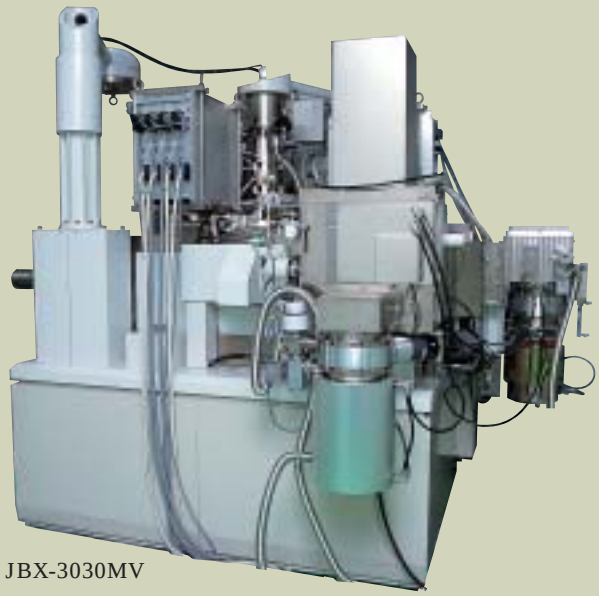

JBX-3030MV

applied.

Enhanced Speed Data Transfer System

The 3030MV supports a new format, JEOL52V3.1, in addition to JEOL52V2.1 and JEOL52V3.0 used in the 9000MV series. JEOL52V3.1 format has reduced the data volume, compared to JEOL52V3.0. Figure 1 shows that the system stores the pattern data to write in the disk of the control workstation, and compacts and saves the data in the data memory (double buffer) of the CPU-3 upon the start of exposure. If the data volume exceeds the memory size, the system will store the data in units of field. The system unzips and transfers the data to the shot partition unit, where the data is divided into rectangles and trapezoids. The sort circuit will separate the data into shots to determine the shot exposure sequence. Concurrently, the proximity correction unit of the CPU-4 will calculate the energy intensity distribution per field of backscattered electrons and map the proximity effect correction data.

The system will calculate the shot time for the data forwarded from the sort unit in the order of exposure, taking into consideration proximity correction and fogging correction (in mm). The shot time thus determined for each shot will be forwarded to the blanking amplifier. The system will further apply various correction data, including the size, position, dynamic focus, and dynamic astigmatism, to the data from the sort unit, and forward the corrected data to the DAC/AMP.

New Material Handling Unit

One of the factors that degrade the global placement accuracy is temperature fluctuation of the mask blank being exposed. To minimize this error, the 3030MV incorporates a loading system designed to handle mask blanks without cassettes. Mask blanks are stored in a mask stocker where the temperature fluctuation is controlled to $\pm 0.01^{\circ}$, and will be loaded to the exposure chamber through the mask exchange chamber by the exposure program.

Evaluation Results

Resolution

Figure 3 shows two SEM photos demonstrating pattern fidelities of 240 nm-Line/Space and 240 nm-Holes on FEP171 resist (400 nm thick).

CD Accuracy

Local CD Accuracy

Figure 4 shows the CD uniformity in a writing field 1mm by 1 mm. 3-sigma value was within 3 nm. An LWM was used for measurement.

Global CD Accuracy

Figure 5 shows the CD uniformity of isolated lines (resist image) within a mask plate. 3-sigma value was within 4 nm. A CD metrology SEM was used for measurement.

CD Linearity

Figure 6 shows the CD linearity for isolated clear lines 200 nm to 1500 nm wide. The CD linearity was 7 nm peak to peak. A CD metrology SEM was used for measurement.

Pattern Placement Accuracy

Local Placement Accuracy

Figure 7 shows the local placement accuracy within an area of 1.1 mm × 1.1 mm including the field boundary when field shift writing was performed twice. An LMSIPRO was used for measurement. Accuracies were measured at 5 locations in the mask blank and overlapped in the figure. The maximum error was less than 6 nm.

Figure 8 is a histogram of the field gain and rotation error calculated on the positional data on the field boundary alone. The field stitching accuracy was ±5 nm.

Global Placement Accuracy

Figure 9 shows the global placement accuracy within an area of 133 mm × 133 mm when field shift writing was performed twice. An LMSIPRO was used for measurement. The placement accuracy was ±8 nm.

Overlay Accuracy

To evaluate the overlay accuracy, the positional accuracy within an area of 133 mm × 133 mm was measured on two masks, and the difference was calculated. The placement accuracy was ±7 nm.

Writing Speed

Figure 10 compares the writing speed between the 3030MV and 9000MV systems. The writing speed of the 3030MV was three times faster than the 9000MV series, thanks to the settling time of the DAC amplifier reduced by the sub deflector, the higher current density, and the enhanced data transfer system.

Summary

JEOL developed a new electron beam mask writing system, JBX-3030MV, for production of masks for 100 to 90 nm technology node. Improvements were applied to the proximity effect correction system, glass-in glass-out material handling system, and the electrostatic beam deflection system.

The system achieved a CD uniformity within a plate of 8nm (3σ), a CD linearity of 15nm p-p, a field stitching accuracy of ±10 nm, and an image position accuracy of ±12 nm. Writing accuracies of the system meet the specifications required for the production of 100 to 90 nm node reticles with an extendibility to 70 nm node reticles.

Acknowledgements

Part of this work was performed under the management of ASET supported by NEDO. The authors would like to thank the Mask Division of HOYA Corporation for their generous support in evaluating the system.

References

1. T.Komagata, Y.Nakagawa, H.Takemura, N.Gotoh, K.Tanaka “Development of a Next Generation E-Beam, Lithography System for 1Gbit Dram Masks”, SPIE vol.3331/313,(1998)
2. T.Komagata, Y.Nakagawa, N.Gotoh, K.Tanaka “Performance of improved e-beam lithography system JBX-9000MVII”, SPIE vol.4409/248, (2001)

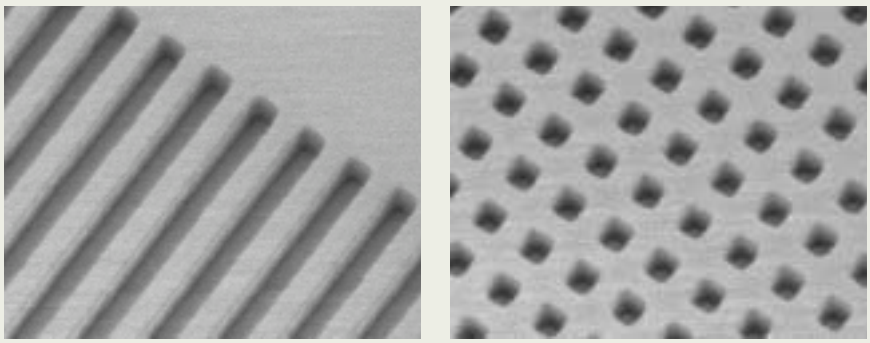

240 nm Line and Space

Pattern Fidelity of 240 nm-Line/Space
(FEP171 resist, 400 nm thick)

240 nm Hole

Pattern Fidelity of 240 nm-Holes
(FEP171 resist, 400 nm thick)

Fig. 3. Pattern fidelity of line/space and holes.

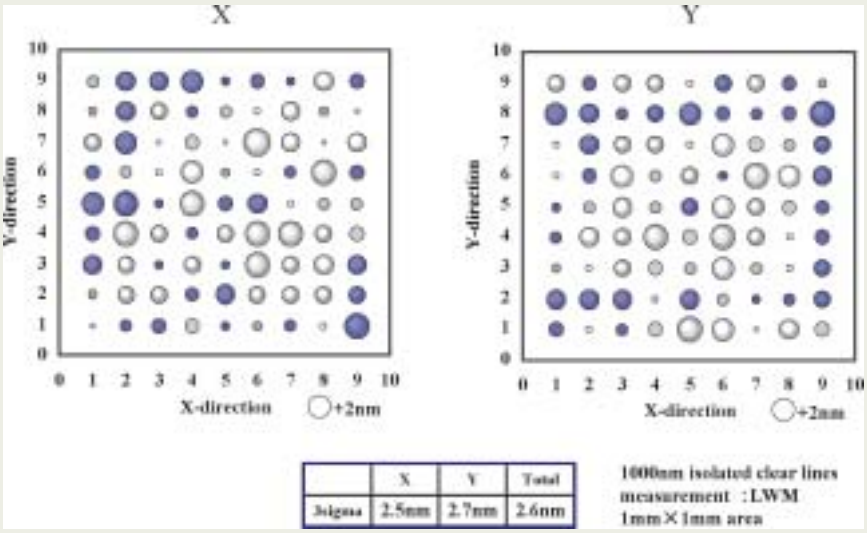

Fig. 4. CD uniformity in writing field.

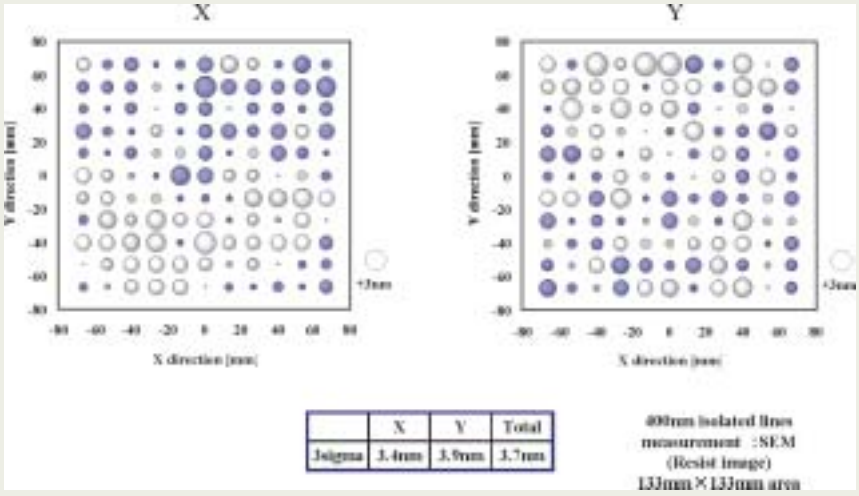

Fig. 5. CD uniformity of isolated lines within mask plate.

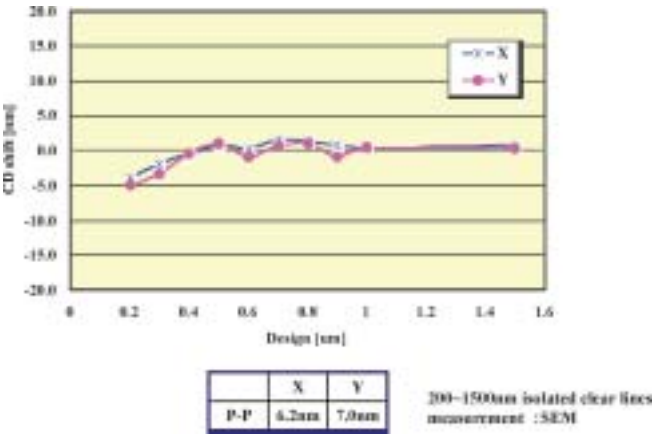

Fig. 6. CD linearity for 200 nm to 1500 nm lines.

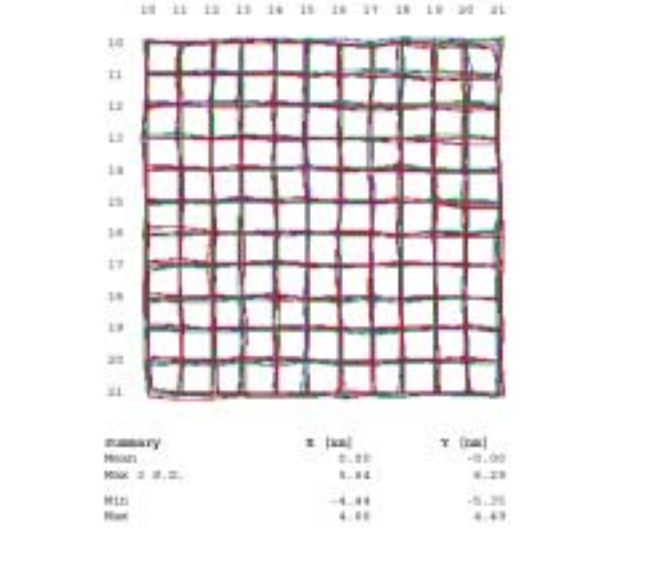

Fig. 7. Local placement accuracy (1.1 mm×1.1 mm area, 5 locations)

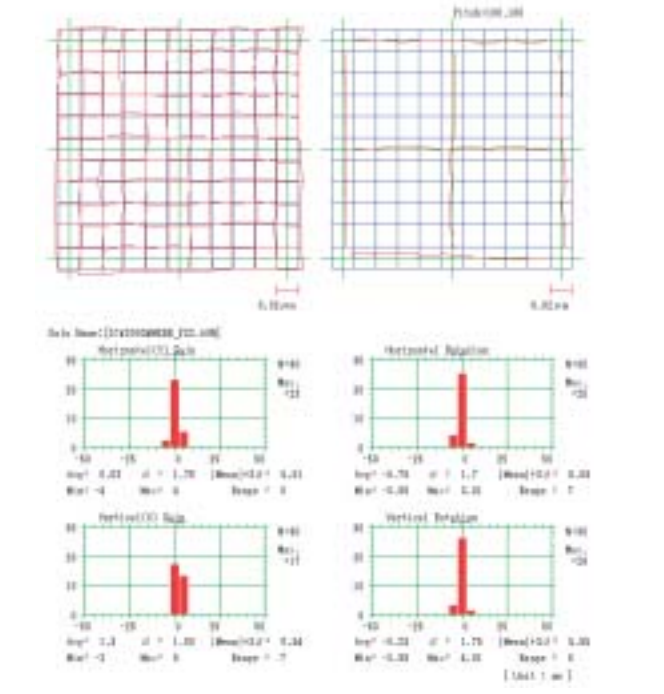

Fig. 8. Field stitching accuracy.

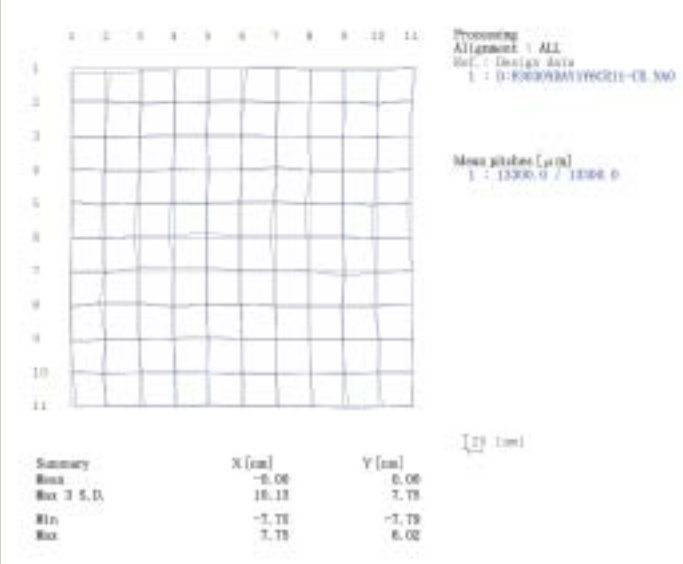

Fig. 9. Global placement accuracy (133 mm×133 mm area)

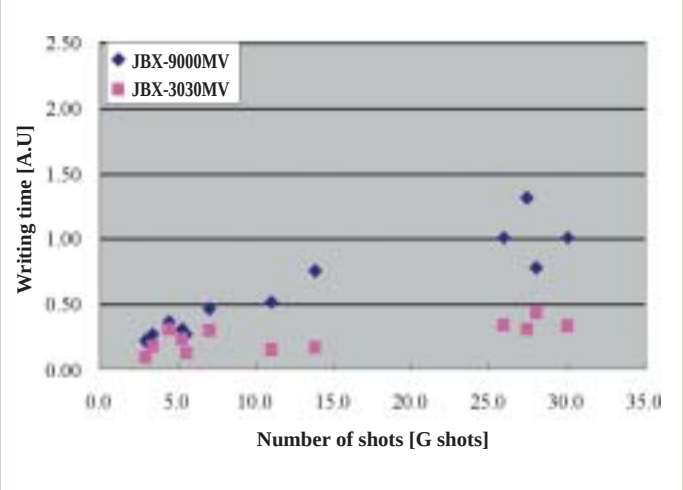

Fig. 10. Writing speed.

Chromatic and Spherical Aberration Correction in the LSI Inspection Scanning Electron Microscope

Kazuhiro Honda[†], **Susumu Takashima**[††]

[†] **Advanced Technology Division, JEOL Ltd.**
[††] **JEOL Technoservice Co., Ltd.**

This paper describes the principle and an experimental result of the chromatic and spherical aberration correction in the scanning electron microscope (SEM) based on the aberration correction method which Zach et al. have developed with a multipole corrector [1][2]. The equipped corrector has been newly developed and designed to suit to the JWS-7555S(JEOL) column, which has been used for the LSI inspection in semiconductor manufacturing. In this use of the SEM, lower acceleration voltage, below 1 keV, has been routinely used nowadays for observing the LSI specimen to minimize the damage from the electron beam collision and the specimen charging-up. In addition to that, the largely-tilted SEM image such as 60 degrees is required to observe boundary microstructures. The objective lens must be conical and has a longer working distance, which increases the aberration coefficients. The aberration correction can be expected to overcome these difficulties.

We have attained a corrected resolution below 2.5 nm at 1 keV acceleration voltage with the newly installed aberration corrector.

Introduction

So far the dominant aberrations, which deteriorate the SEM image, have been the 1st-order chromatic and 3rd-order spherical aberrations of the objective lens. Consequently column engineers have been struggling to "reduce" these aberrations because Scherzer proved theoretically in 1936 that the chromatic and the spherical aberration coefficients are always positive with the rotationally symmetric lens. The aberration reduction technique has been developed such as the magnetic field immersion objective lens, the static electric retarding field objective lens and the compound one of these fields. However, these objective lenses have limitations of the resolution as well as of observing conditions. As for the latter, these are useful only for horizontal images. On the contrary, there are several proposals to "vanish" these aberrations by canceling those positive aberrations with generating negative ones by adapting another non-rotationally symmetric multipole lenses [3]. However sophisticated matters with the multipole have revealed the difficulties against constructing a mechanically-precise and systematically-stable correction system for several tens of years. Zach et al. have overcome these difficulties by using 12-pole-pin multipole computer control system, which can compensate the miss-alignment factor and the residual aberration by composing several multipole fields, di-, quadru-, hexa-, octo-pole fields [1][2].

In the region of the semiconductor manufacturing, the aberration correction is suited well to the LSI inspection, which has to be made with a lower acceleration voltage such as below 1 keV. In order to show the practicality and the efficiency of the aberration correction experimentally, we have developed and constructed a suitable correction system to the JWS-7555S(JEOL), the LSI inspection scanning electron microscope.

Principles of the Chromatic and Spherical Aberration Correction

The principles of the chromatic and spherical aberration correction, which we have employed, are based on the Zach's method [1][2]. In this section, short explanations for some key points of his correction principles are summarized.

Chromatic aberration correction

The 1st-order chromatic aberration in each X- and Y-direction can be compensated independently by using four quadru-pole elements. The electron beam paths, X- and Y-trajectory, in the corrector are shown

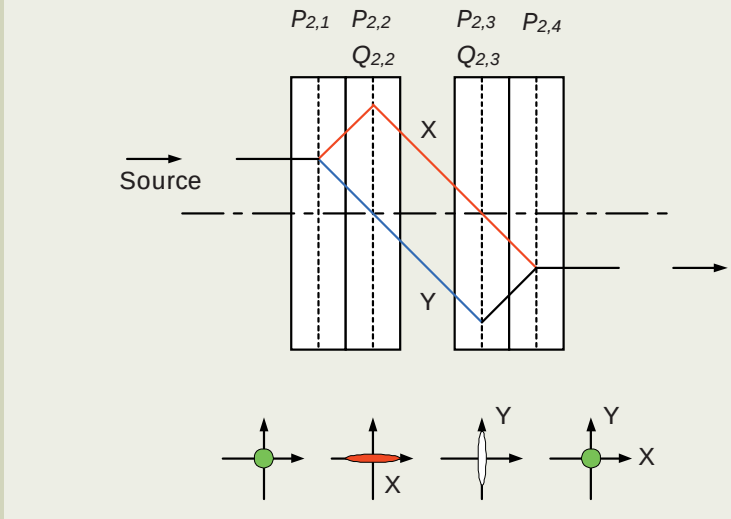

Fig. 1. Schematic image of an electron beam path in the corrector.

schematically in **Fig. 1**. The quadru-pole field acts as focusing in X(Y)-direction and diverting in Y(X)-direction simultaneously. The electron beam having a round shape, entered from the left-hand side to the corrector, is affected by the 1st-stage quadru-pole field and the X-direction beam is diverted and the Y-direction beam is focused, for example, being defined like in Fig. 1. The 2nd-, 3rd- and 4th-stage quadru-pole fields affect the electron beam shape as shown in Fig. 1 in this case.

As for the aberration correction, not only for the chromatic but also for the spherical, it is very important to pass the center of the 2nd-stage quadru-pole field for the electron beam in the Y-direction and to pass the center of the 3rd-stage quadru-pole field in the X-direction. And also important is to keep the stigmatic condition between the X- and Y-direction simultaneously. The reason for keeping these conditions is explained later in this section. In the 2nd- and 3rd-stages, magnetic quadru-pole fields are formed within the static electric quadru-pole fields for the chromatic aberration correction. The 1st-order electron trajectories (x (z), y (z): z means the axial coordinate) are constrained in *eqs*. (1) and (2).

$$x''(z)+\left\{\frac{\eta\, Q_2(z)}{\sqrt{\Phi_0}}-\frac{P_2(z)}{2\Phi_0}\right\}_t x(z)=0 \quad (1)$$

$$y''(z)-\left\{\frac{\eta\, Q_2(z)}{\sqrt{\Phi_0}}-\frac{P_2(z)}{2\Phi_0}\right\}_t y(z)=0 \quad (2)$$

$$\text{where,}\quad Q_2(z)=\sum_{i=1}^{4}Q_{2,i}(z),$$

$$P_2(z)=\sum_{i=1}^{4}P_{2,i}(z),\qquad \eta=\sqrt{\frac{e}{2m_e}}$$

Here, $Q_{2,i}$ and $P_{2,i}$ denote the magnetic and electric quadru-pole field strength respectively and the suffix i denotes the quadru-pole stage number. Φ_0 denotes the specimen potential. e and m_e are the electron charge and the rest mass. In *eqs*. (1) and (2), only if the $\{\ \}_t$ parts are fixed to certain values, it is able to vary P_2 and Q_2 arbitrary with keeping the electron trajectories to certain paths. The 1st-order chromatic aberration coefficients, C_{cx} and C_{cy} in each X- and Y-direction of the corrector, are shown in *eqs*. (3) and (4).

$$Ccx = -(m_o m_x)^2 \int_{corr}\left\{\frac{\eta\, Q_2(z)}{2\sqrt{\Phi_0}}-\frac{P_2(z)}{2\Phi_0}\right\}_c x^2(z)\,dz \quad (3)$$

$$Ccy = +(m_o m_y)^2 \int_{corr}\left\{\frac{\eta\, Q_2(z)}{2\sqrt{\Phi_0}}-\frac{P_2(z)}{2\Phi_0}\right\}_c y^2(z)\,dz \quad (4)$$

Here, m_0, m_x and m_y mean the magnifications of the objective lens, of the total X- and Y-direction quadru-poles on the specimen. Comparing the $\{\ \}_c$ and $\{\ \}_t$ in eqs. (1)-(4), Q_2 part in $\{\ \}_c$ is half of that in $\{\ \}_t$, which means that it is possible to vary C_{cx} and C_{cy} independently and arbitrary with keeping the electron trajectories to certain paths. If the stigmatic trajectory condition is kept as in Fig.1 passing through the center of $Q_{2,2}$ and $P_{2,2}$ in the Y-direction and of $Q_{2,3}$ and $P_{2,3}$ in the X-direction, C_{cx} and C_{cy} are controlled only by changing the combination ratio $Q_{2,2}/P_{2,2}$ and $Q_{2,3}/P_{2,3}$. The total chromatic aberration is corrected by adjusting the 2nd- and 3rd- stage quadru-pole fields to satisfy the condition in *eq*. (5), where C_{co} means the chromatic aberration coefficient of the objective lens.

$$C_{cx}=C_{cy}=-C_{co} \quad (5)$$

Spherical aberration correction

In the ordinal round lens, because of the rotationally symmetric field, the spherical aberration has only to be concerned with the 3rd-order aperture aberration in one direction. In the non-rotationally symmetric lens, however, composed 3rd-order aperture aberrations in the X- and Y-directions appear explicitly. The 3rd-order aperture aberrations in the X- and Y-direction, Δx and Δy, with the corrector and the objective lens are written as *eqs*. (6) and (7).

$$\Delta x=\left(C_{30}x_i'^3+C_{12}x_i'y_i'^2\right)+C_s x_i'\left(x_i'^2+y_i'^2\right) \quad (6)$$

$$\Delta y=\left(C_{03}y_i'^3+C_{21}x_i'^2y_i'\right)+C_s y_i'\left(x_i'^2+y_i'^2\right) \quad (7)$$

Here, x_i' and y_i' are slopes of the electron beam on the specimen in the X- and Y-direction. C_{ij} denotes the 3rd-order aperture aberration coefficient, whose suffixes depend on the x and y composition. C_s means the spherical aberration coefficient of the objective lens. In *eqs*. (6) and (7), The first bracket term comes from the corrector and the second one from the objective lens. Re-written forms of *eqs*. (6) and (7) turn out to be *eqs*. (6a) and (7a) based on the aperture angle composition.

$$\Delta x=(C_{30}+C_s)x_i'^3+(C_{12}+C_s)x_i'y_i'^2 \quad (6a)$$

$$\Delta y=(C_{03}+C_s)y_i'^3+(C_{21}+C_s)x_i'^2y_i' \quad (7a)$$

From *eqs*. (6a) and (7a), the correction condition of the 3rd-order aperture aberration is obtained as *eq*. (8).

$$C_{30}=C_{03}=C_{12}=C_{21}=-C_s \quad (8)$$

Now the electron beam is constraint in the stigmatic trajectory mentioned earlier and shown in Fig. 1 and the chromatic aberration is compensated by four quadru-pole elements. In this condition, quadru-pole fields also generate the 3rd-order aperture aberrations, of which coefficients are defined as C_{ij}^{quad}(i,j=0,1,2,3: i+j=3). Some octo-pole fields are used to compensate not only C_s but also C_{ij}^{quad}, which are available on the 12 pole-pin multipoles, and as in the same way, of which 3rd-order aperture aberration coefficients are defined as C_{ij}^{oct}(i,j=0,1,2,3: i+j=3). Then the *eqs*. (6a) and (7a) can be re-written as *eqs*. (6b) and (7b).

$$\Delta x=\left(C_{30}^{quad}+C_{30}^{oct}+C_s\right)x_i'^3+\left(C_{12}^{quad}+C_{12}^{oct}+C_s\right)x_i'y_i'^2 \quad (6b)$$

$$\Delta y=\left(C_{03}^{quad}+C_{03}^{oct}+C_s\right)y_i'^3+\left(C_{21}^{quad}+C_{21}^{oct}+C_s\right)x_i'^2y_i' \quad (7b)$$

$$\text{where,}\quad C_{ij}^{quad}=\sum_{k=1}^{4}C_{ij}^{quad,k},$$

$$C_{ij}^{oct}=\sum_{k=1}^{4}C_{ij}^{oct,k}\quad (\text{k: stage number})$$

If the stigmatic trajectory is kept, the aberration coefficients $C_{03}^{oct,2}$, $C_{30}^{oct,3}$, $C_{12}^{oct,2}$, $C_{21}^{oct,2}$, $C_{12}^{oct,3}$and $C_{21}^{oct,3}$ are negligible on the same reason as the chromatic aberration correction. Consequently the 3rd-order aperture aberration correction condition turns out to be the conditions (8a-d).

$$C_{30}^{oct,2}=-\left(C_{30}^{quad}+C_{30}^{oct,1}+C_{30}^{oct,4}+C_s\right) \quad (8a)$$

$$C_{03}^{oct,3}=-\left(C_{03}^{quad}+C_{03}^{oct,1}+C_{03}^{oct,4}+C_s\right) \quad (8b)$$

$$C_{12}^{oct,1}+C_{12}^{oct,4}=-\left(C_{12}^{quad}+C_s\right) \quad (8c)$$

$$C_{21}^{oct,1}+C_{21}^{oct,4}=-\left(C_{21}^{quad}+C_s\right) \quad (8d)$$

Strictly speaking, in the stigmatic condition, the following conditions written in *eq*. (9) are to be fulfilled.

$$C_{12}^{quad}=C_{21}^{quad},C_{12}^{oct,1}=C_{21}^{oct,1},C_{12}^{oct,4}=C_{21}^{oct,4} \quad (9)$$

Then the condition (8d) turns out to be of no use. The cross-term aberration coefficient C_{12}^{quad},which is fixed after the chromatic aberration correction being completed, is compensated by the outer octo-pole fields in the condition (8c). Then $C_{30}^{oct,1}$, $C_{03}^{oct,1}$, $C_{30}^{oct,4}$and $C_{03}^{oct,4}$, turn to be static values and the inner octo-pole fields have only to be set to fulfill the condition (8a) and (8b).

Experimental

System configuration

A schematic diagram of the experimental aberration correction system is shown in **Fig. 2**. The corrector is installed in the JWS-7555S(JEOL) scanning electron microscope, which consists of the TFE (thermal field emission) emitter, the probe current control lenses (CL1, CL2), the intermediate acceleration lens (Vint) and the compound

(magnetic and retarding fields) objective lens (OL). The corrector is inserted between the OL aperture and the intermediate acceleration lens in order to maintain the proper dynamic range of the corrector driver unit. Because the column potential is the GND level and the energy potential below the intermediate acceleration is boosted in 8 keV and finally it returns to the original level by the retarding field, setting the corrector driver unit to the lower potential produces better dynamic range compared with setting it to the higher potential. A schematic diagram of the corrector is sown in **Fig. 3**. The corrector consists of 4 stages of 12-pole-pin multipole. In the 2nd- and 3rd-stage multipole especially, coils are wound around poles to generate the quadrupole magnetic field. The correction control software is installed into the host computer, which enables the easy operation of the complicated 12-pole-pin and 4-stage multipole system using the graphical user interface (GUI). The electric and the magnetic potential V(t,p) are assigned to each pole as in **Fig. 4** using trigonometric functions, where Gx and Gy mean the gain to be controlled. Each multipole field is loaded simultaneously based on the linear summation theorem.

A calculated electron beam path is shown in **Fig. 5**. In order to maintain the stable condition of the corrector, the cross-over position of the inlet side to the corrector is fixed to the optimum which brings the optimum aperture angle at approximately 16 mrad on the image plane. In the outlet side from the corrector, the beam path goes through near the center of the intermediate acceleration lens (Vint) so as not to be bent largely by its strong field. The objective lens has such a conical shape as to tilt the specimen up to 60 degrees. So the WD (working distance) is 4 mm and the C_s=7.5 mm, C_c=3.6 mm at 1keV on the original specification of this column (without correction) that limits the resolution to 5 nm at the same acceleration voltage. If the 1st-order chromatic and the 3rd-order spherical aberrations are completely compensated by the corrector on this column, the theoretical resolution limit is estimated of 1.5 nm at 1keV.

Adjustment of the multipole fields of the corrector

The practical adjustment method is also the same as the Zach's method, which is described in his article in detail [1][2]. In the following, main points are briefly summarized.

Correction flow

The correction has to be made in sequence and iteration. The correction flow is shown in **Fig. 6**. Before the "correction start", the electron beam has to be aligned without corrector. Firstly the theoretical correction values are set to the correction control unit, which is very important because the system is so complicated as to lose the SEM image if the values are not properly chosen. Secondly the stigmatic trajectory, which is mentioned previously, has to be completed absolutely. If the line-images in the 2nd- and 3rd-stage are mis-aligned, severe residual aberrations are generated. After that, C_c and C_s correction procedures are followed. Finally the residual aberrations, coma, 45-degree, 3-fold and 4-fold astigmatisms etc. are compensated. Generally the C_s and the residual aberration corrections have to be made iteratively because the 3rd-order aperture aberration system is linked together.

C_c correction

The focusing error Δf, which is induced by the chromatic aberration, can be written in the power series of the beam energy divergence $\kappa=\Delta E/E$ as shown in *eq.* (10), where E denotes the electron beam energy.

$$\Delta f = \kappa C_c + \kappa^2 K_c + \cdots \qquad (10)$$

Here, C_c and K_c are the 1st-order and the 2nd-order chromatic aberration coefficients respectively. Higher order aberrations are

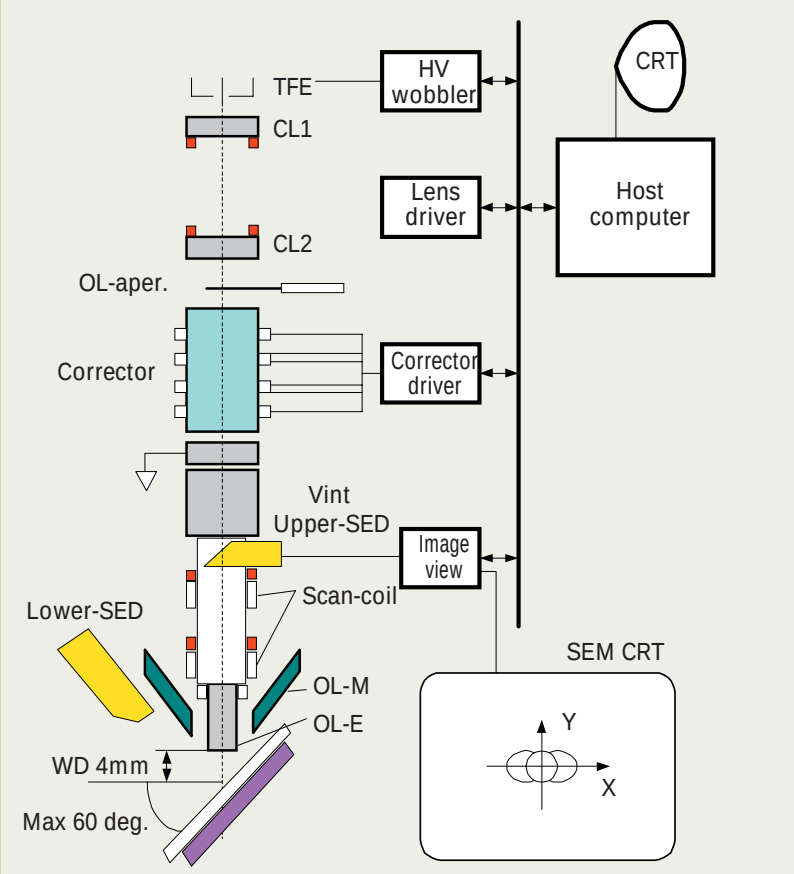

Fig. 2. Schematic diagram of the aberration correction system.

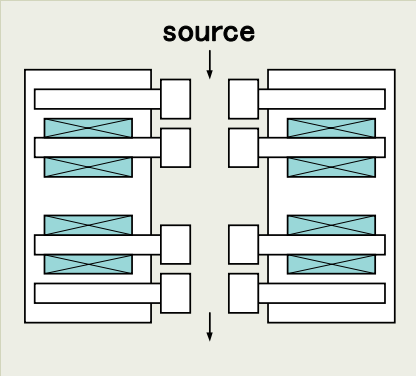

Fig. 3. Schematic diagram of the corrector.

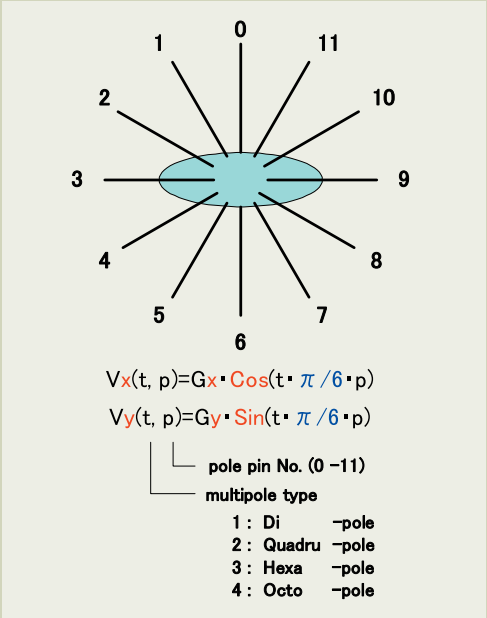

Fig. 4. Pole pin assign method for 12-pole-pin multipole corrector.

negligible in this case because only C_c can be compensated. The graphical representation of *eq.* (10) is shown in **Fig. 7**. Generally the TFE has the energy spread $|\Delta E|$=0.5 to 0.8 eV, which broadens the focusing position by $|\Delta f_c$ (un-corrected)| as shown in the figure. If the C_c vanishes, only the quadratic term remains in *eq.* (10), which means $|\Delta f_c$ (corrected)| becomes negligibly small. In order to make this condition visible, the energy of the electron beam is slightly shifted up and down, that is E2 and E1 respectively. If the system is corrected, the image planes of those energies are on the same position, Δf(E1) = Δf(E2). When observing a round shape particle, by searching Δf which makes the 1-dimensional edge clear at both E1 and E2 as shown in **Fig. 8**, it is possible to detect the corrected condition.

C_s correction

The spherical aberration makes the caustic surface of the electron beam as shown in **Fig. 9**, which shows the case of the under correction, that is $C_s > 0$. The intensity profile of the source side electron beam has two peaks in such a case. And these peaks appear on the

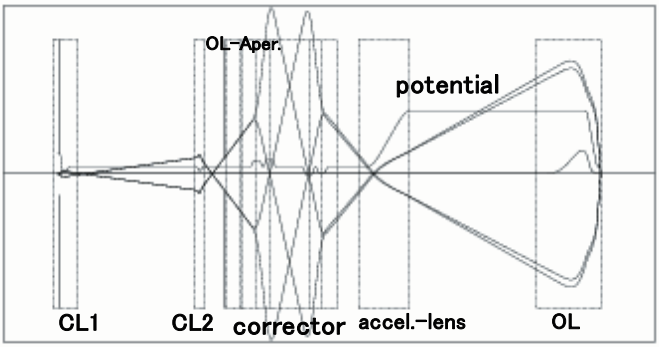

Fig. 5. Calculated electron beam path in the correction system.

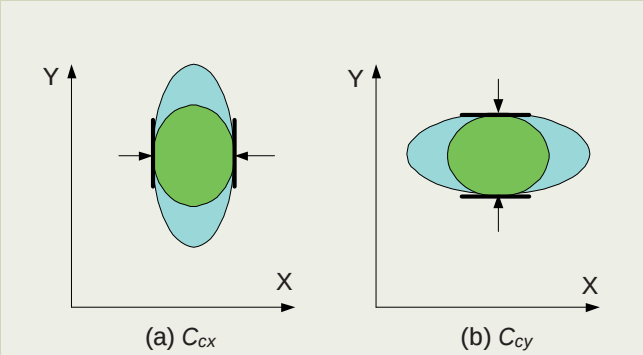

Fig. 8. 1-dimensional focusing image.

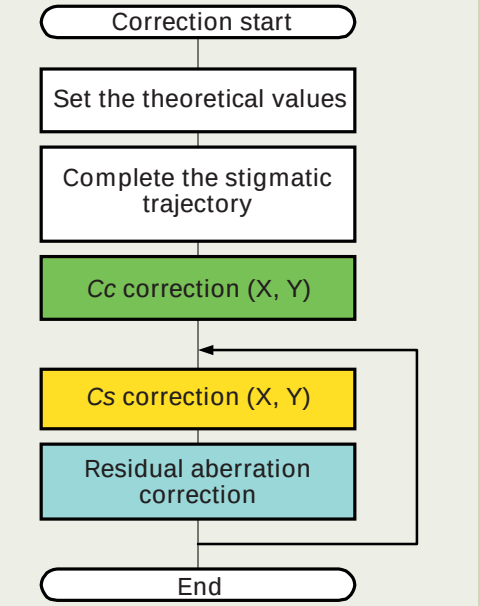

Fig. 6. Correction flow.

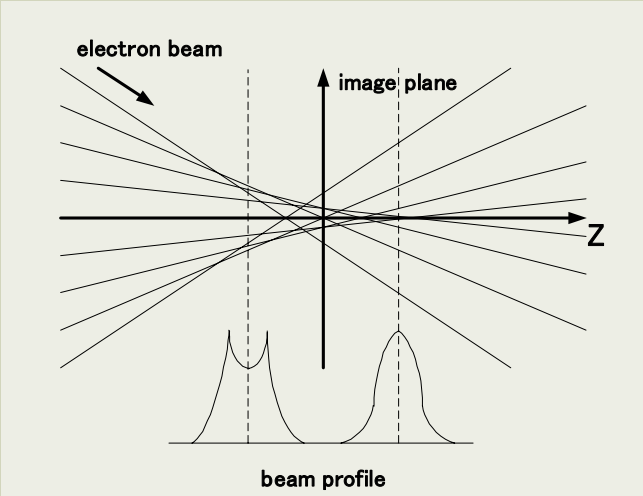

Fig. 9. Un-corrected beam profile.

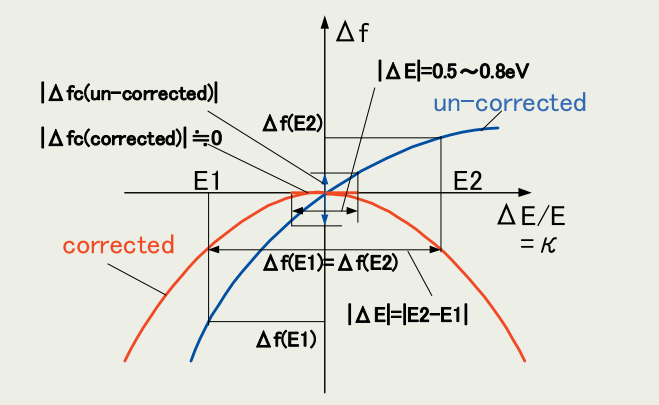

Fig. 7. Chromatic aberration against ΔE/E.

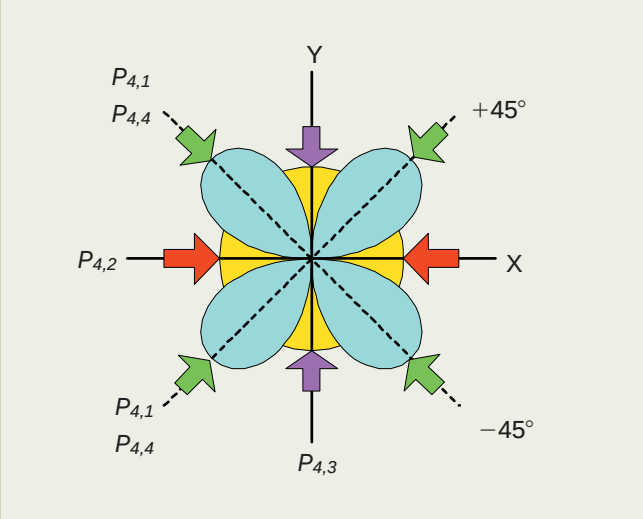

Fig.10. Four-fold astigmatism.

opposite side of the image plane in the case of the over correction, that is $C_s < 0$. These two peaks make a double focused SEM image and the correction condition can be adjusted so as not to appear the double image in both sides, that is $C_s = 0$.

The 3rd-order aperture aberration has not only the isotropic spherical aberration but also the four-fold astigmatism, which are generated in accordance with the composing ratio of $C_{ij}^{quad,\,k}$ and $C_{ij}^{oct,k}$ in *eqs*. (8a-d). A schematic image of the four-fold astigmatism is shown in **Fig. 10**. It resembles four leaves, which spread to ±45-degrees direction. $P_{4,i}$ means the octo-pole field of the i-th stage. After the four-fold astigmatism is compensated by the outer octo-pole fields $P_{4,1}$ and $P_{4,4}$, the spherical aberration must be re-compensated by the inner octo-pole fields $P_{4,2}$ and $P_{4,3}$ iteratively because they are linked together.

Corrected SEM image

An original SEM image (without corrector) and a corrected SEM image (with corrector) of gold particles on carbon substrate are illustrated in **Fig. 11** and **Fig. 12** respectively with 1 keV acceleration voltage and 30 pA probe current. When these two images are compared, the superior image quality and higher resolution are easily observed in the corrected image. The resolution of the corrected image is approximately 2.5 nm.
A tilted image in 45 degrees is shown in **Fig. 13**, which shows 0.5 μm Line & Space resist patterns at 1 keV acceleration voltage. Microstructures on the side-wall of the patterns are clearly visible.

Conclusion

The applied column of the corrector has a long working distance (4 mm) and a conical shape objective lens (60 degrees), which increases the aberration. However the resolution could be reduced to 2.5 nm (corrected) dramatically and stably from 5 nm (un-corrected) at 1 keV acceleration voltage by the chromatic and spherical aberration correction. The present report demonstrates the usefulness and efficiency of the Zach's correction method for such SEMs as those for the LSI inspection in the semiconductor industry.

Acknowledgement

The author would like to thank Dr. Joachim Zach of CEOS GmbH for constructing the corrector and the control system; and Dr. Makoto Kato of JEOL Ltd. for helpful discussions.

Reference

1. J. Zach and M. Haider, "Aberration correction in a low voltage scanning microscope", Nuclear Instruments and Methods in Physics Research (Section A), Vol.363, No.1, 2, pp.316-325, 1995.
2. J. Zach, "Design of a high resolution low voltage scanning electron microscope", Optik, 83, No.1, pp.30-40, 1989.
3. P. W. Hawkes and E. Kasper, "PRINCIPLES OF ELECTRON OPTICS", Vol.2, (Academic Press, London 1989), pp.857-878.

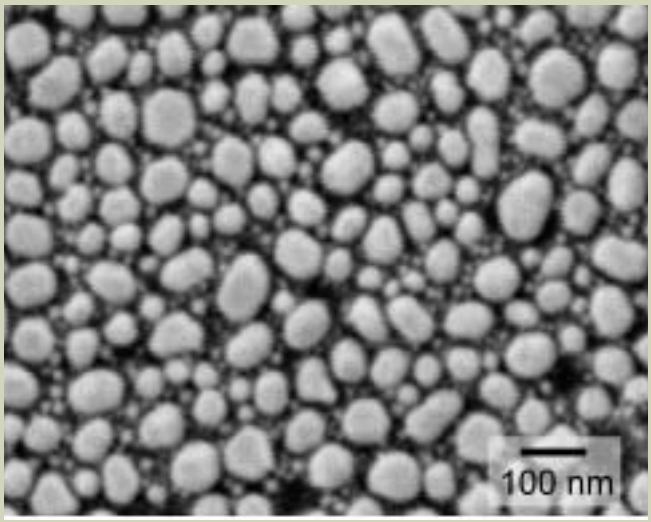

Fig. 11. Un-corrected original SEM image (without corrector).

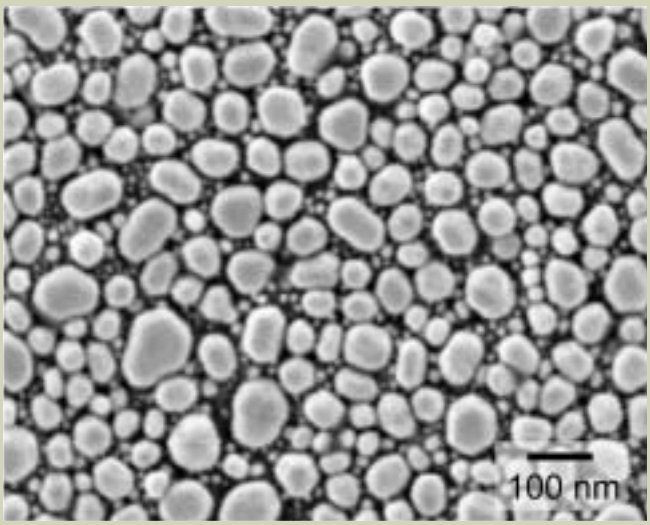

Fig. 12. Corrected SEM image (with corrector).

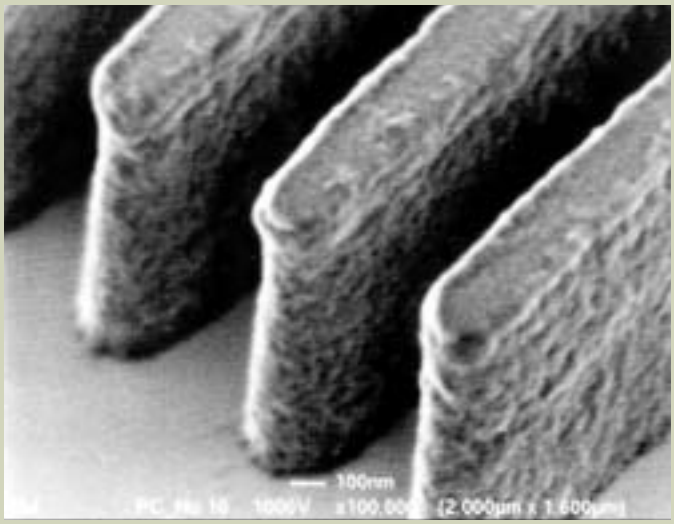

Fig. 13. 45-degree tilted SEM image (0.5 μm Line & Space resist patterns).

Peak Deconvolution Analysis in Auger Electron Spectroscopy II

Kenichi Tsutsumi and Yuji Nagasawa

Application & Research Center, JEOL Ltd.

The Auger electron micro-probe instruments (JAMP-7800 series) have enabled measurement of a spectrum with energy resolution of 0.6% for general use to 0.06% at maximum. This capability has made it possible to clarify not only the characteristics of the main peak of each element but also the fine structures of the spectrum. In the previous report, "Peak Deconvolution Analysis in Auger Electron Spectroscopy" [1][2], the spectral peak deconvolution analysis was shown to be very effective in the chemical state analysis and the qualitative analysis for the Auger spectrum measured with high energy resolution. However, a quantitative analysis using the deconvoluted spectra sometimes contains errors more than 40%, which indicates the necessity of a quantitative analysis taking the matrix effect into consideration.

In this report, a quantitative analysis for a multi-element sample has been made, by considering the matrix effect of the spectra to which the peak deconvolution analysis is applied. The matrix correction calculation is found to be very effective, and it is possible to carry out the quantitative analysis with quantitative error within a few percent.

The Quantitative Correction Calculation Considering the Matrix Effect

Problems in auger quantitative analysis

The quantitative analysis in general has been made using the K-value method based on the intensity ratio between the unknown and standard spectra or the calibration curve method, by referring to a standard spectrum measured with a standard sample. Therefore, precise measurement of the standard spectrum is of primary importance, and its result greatly affects the precision of the quantitative analysis. However it is difficult to evaluate a standard spectrum because the spectral peak intensity and the shape change greatly depending on the difference in physical and chemical condition of the extreme surface (about 6nm deep). This makes Auger quantitative analysis difficult. Furthermore, the reason is divided largely into the following three categories.

Firstly, it is difficult to obtain a standard sample that keeps its composition precisely in the extreme surface region. Even if the composition of the bulk sample is definitely known, it has usually different composition in surface region that is changed by physical or chemical adsorption, oxidation or other processes in the natural atmosphere. In practice, it is widely accepted to employ the ion-sputtering method in order to obtain a clean surface, which can be considered to have the same atomic concentration as bulk. However, in the ion-sputtering method, the composition on the extreme surface may become different from the composition in the bulk sample owing to such effects as selective sputtering and mixing, so attention should be paid to using the sputtered surface as a standard sample.

Secondly, the Auger peak intensity of a certain element is decided by not only its atomic concentration, but also other elements that constitute the matrix part. This is called the matrix effect. For instance, the Auger peak intensity of carbon in the surface area is more detected on the matrix composed of heavy metal elements than light ones, even if the atomic concentration is same. The more backscattered electrons fall back to the surface from the heavy metal matrix, the more Auger electrons are generated. In this case, if the quantitative analysis of carbon is carried out by referring to a standard spectrum of pure carbon with a concentration of 100%, the result usually exceeds 100%. Therefore, when measuring a standard spectrum, the peak intensity changes that depend on the matrix effect of the standard sample should be taken into consideration.

Thirdly, as the Auger electron is a kind of the secondary electron, the yield of Auger electron is also affected by the incident angle of the electron beam and the plane direction (channeling effect). These causes affect the yield of secondary electrons. When measuring a standard spectrum, care should be taken to measure between the unknown sample and the standard sample under conditions as similar as possible.

For the above reasons, the quantitative analysis with the Auger spectrum generally uses the relative sensitivity factor method that offsets and averages errors, The precision depends greatly on the standard spectrum obtaining the relative sensitivity factor, so an appropriate standard sample for the measuring sample should be selected. With this method, however, it is not possible to make a truly meaningful quantitative evaluation of the Auger spectrum, because it cancels out all the physical and chemical information on the sample carried in the spectrum. In order to make a precise evaluation of the Auger spectrum, quantitative analysis should be carried out by estimating the errors correctly.

In this report, a quantitative correction calculation has been made for correcting the matrix effect based on the spectra obtained by the peak deconvolution method, and its possibilities have been studied.

The factors determining the peak intensity of Auger electron

The peak intensity that is measured by using AES, from the UWV Auger transition of *i*-th element contained in a multi-element sample, is expressed by the following equation:

$$I_i(UVW) = I_p \cdot R \cdot \rho(UVW) \cdot T \cdot \phi_i(E_p, E_u) \cdot V_i(E_p, E_u) \cdot n(C_i^s) \cdot \lambda_i(C_i^s) \cdot \gamma_i(E_p, C_i^s) \cdot C_i^s \quad \cdots\cdots\cdots\cdots\cdots (1)$$

I_p :	Primary electron beam current
R :	Surface roughness factor
ρ (UVW) :	UVW Auger transition probability
T :	Analyzer transmittivity
$\phi_i(E_p, E_u)$:	Ionization cross section
E_p :	Primary electron beam energy
E_u :	Ionization energy
$V_i(E_p, E_u)$:	Contribution of the Coster-Kronig transition
$n(C_i^s)$:	Atomic density (Number of atoms per unit volume)
$\lambda_i(C_i^s)$:	Average electron escape depth
$\gamma_i(E_p, C_i^s)$:	Backscattered electron correction
C_i^s :	Atomic concentration of i-th element

On the other hand, the Auger peak intensity I_i^0

(UVW) from the *i*-th element under the same condition is expressed by the following equation:

$$I_i^0(UVW) = I_p \cdot R^0 \cdot \rho(UVW) \cdot T \cdot \phi_i(E_p, E_u) \cdot V_i(E_p, E_u) \cdot n_i^0 \cdot \lambda_i^0 \cdot \gamma_i^0(E_p) \quad \cdots (2)$$

where, the super script 0 indicates it corresponds to the standard sample.

Now, if we divide Eq. (1) by Eq. (2), the terms intrinsic to the element are canceled out, and it becomes

$$\frac{I_i(UVW)}{I_i^0(UVW)} = \frac{R \cdot n(C_i^s) \cdot \lambda_i(C_i^s) \cdot \gamma_i(E_p, C_i^s) \cdot C_i^s}{R^0 \cdot n_i^0 \cdot \lambda_i^0 \cdot \gamma_i^0(E_p)} \quad \cdots (3)$$

where, by setting

$$\beta(C_i^s, E_p) = \frac{n_i^0 \cdot \lambda_i^0 \cdot \gamma_i^0(E_p)}{n(C_i^s) \cdot \lambda_i(C_i^s) \cdot \gamma_i(E_p, C_i^s)} \quad \cdots (4)$$

and if the surface roughness factors are assumed to be equal for the standard sample and the analysis object sample (R^0=R), Eq. (3) becomes [3]

$$C_i^s = \beta(C_i^s, E_p) \cdot \frac{I_i(UVW)}{I_i^0(UVW)} \quad \cdots (5)$$

Here, $\beta(C_i^s)$ is the correction factor for the matrix effect and we call it the matrix correction function. In the system where the matrix effect is small, it becomes $\beta(C_i^s) \cong 1$, and then the Eq. (5) becomes as follows, making the peak intensity ratio equal to the concentration.

$$C_i^s \cong \frac{I_i(UVW)}{I_i^0(UVW)} \quad \cdots (6)$$

However, in most cases, the matrix effect cannot be neglected and a correction calculation is required. In the next section, the matrix correction function will be described.

Matrix function

The matrix function is, as shown in the Eqs. (4) and (5), the correction function that is required to obtain the concentration from the peak intensity ratio of the Auger electron. The meaning of the correction is considered by expanding it to a system of *m* elements. Expanding Eqs. (4) and (5), the concentration of the *i*-th element is expressed by the following equation.

$$C_i = \beta(E_p, C_1, C_2, \cdots, C_m) \cdot \frac{I_i(UVW)}{I_i^0(UVW)} \quad \cdots (6)$$

where

$$\beta(E_p, C_1, C_2, \cdots, C_m) = \frac{n_i^0}{n(C_1, C_2, \cdots, C_m)} \cdot \frac{\lambda_i^0}{\lambda_i(C_1, C_2, \cdots, C_m)} \cdot \frac{\gamma_i^0(E_p)}{\gamma_i(E_p, C_1, C_2, \cdots, C_m)} \quad \cdots (7)$$

The terms comprising the matrix function $\beta(E_p, C_1, C_2, \cdots, C_n)$ perform the atomic density correction, the average escape depth correction and the backscattered electron correction in left to right order. Each correction factor is explained below.

Atomic density correction $n_i^0/n(C_1, C_1, \cdots C_n)$

The relative intensity of the Auger peak is proportional to the atomic density. The atomic density of the standard sample n_i^0 is obtained by the following equation.

$$n_i^0 = \frac{\rho_i \cdot N_A}{A_i} \quad \cdots (8)$$

ρ_i : Density (g/cm^3)

N_A : Avogadro's number (6.02×10^{23})

A_i : Atomic weight

On the other hand, assuming the average atomic density of the multi-element sample $n(C_1, C_1, \cdots C_m)$ is proportional to the concentration of each composition element, it is expressed as follows:

$$n(C_1, C_2, \cdots, C_m) = \sum_{i=1}^{m} C_i \cdot n_i^0 \quad \cdots (9)$$

Average escape depth correction $\lambda_i^0/\lambda_i(C_1, C_2, \cdots C_m)$

The average escape depth, where the Auger electron can escape without losing energy, is determined by the kinetic energies of the Auger electrons and the electron densities (collision cross sections) of the substances that constitute the matrix. It is equal to the mean free path of electron. The average escape depth is 0.5 to 10 nm, because the Auger electron energy of any elements is so low; 30 to 3000 eV, that the interaction of electrons in the solid is large. **Figure 1** shows a graph of the average escape depth. The average escape depth explains the reason why the Auger analysis is called a surface analysis.

Here, the average escape depth of the Auger electron generated from element *i* with energy E_i(eV) when it escapes from the matrix composed of element *j* is obtained. It is given by Tanuma et al. [4][5] with the following formula λ_j^i, where Es_j, β_j, γ_j, a_j, b_j are constants intrinsic to a material.

$$\lambda_i^j = \frac{E_i \times 10^{-10}}{Es_j^2 \left\{\beta_j \cdot 1n(\gamma_j \cdot E_i) - (a_j/E_i) + (b_j/E_i^2)\right\}} \quad \cdots (10)$$

The constants in this equation are defined as follows:

$$n_i^v = \frac{\rho_j \cdot N_v}{A_j} \quad \cdots (11)$$

$$Es_j = 28.8 \times \sqrt{n_j^v} \quad \cdots (12)$$

$$\beta_j = -0.0216 + \frac{0.944}{\sqrt{Es_j^2 + E_g^2}} + 7.39 \times 10^{-4} \cdot \rho_j \quad \cdots (13)$$

$$\gamma_j = \frac{0.191}{\sqrt{\rho_j}} \quad \cdots (14)$$

$$a_j = 1.97 - 0.91 \cdot n_j^v \quad \cdots (15)$$

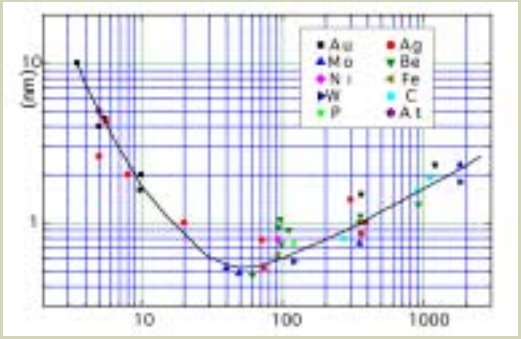

Fig. 1. The average escape depth (≒ mean free path) of electrons from the solid surface.

Table 1. The number of valence electron (N_v) and the plasmon energy (Es_j) for each element.

Element	N_v	Es_j(eV)	Element	N_v	Es_j(eV)	Element	N_v	Es_j(eV)
Li	1	8.0	Fe	8	30.6	In	3	12.6
Be	2	18.4	Co	9	33.6	Sn	4	12.7
B	3	23.4	Ni	10	35.5	Sb	5	15.1
C	4	22.3*	Cu	11	35.9	Te	6	15.6
N	5		Zn	12	33.0	I	7	
O	6		Ga	3	14.5	Cs	1	3.4
F	7		Ge	4	15.6	Ba	2	6.5
Na	1	5.9	As	5	17.8	La	3	10.5
Mg	2	10.9	Se	6	17.4	Hf	4	15.7
Al	3	15.8	Br	7		Ta	5	19.5
Si	4	16.6	Rb	1	3.8	W	6	22.9
P	5		Sr	2	7.0	Re	7	25.6
S	6		Y	3	11.2	Os	8	28.1
Cl	7		Zr	4	15.4	Ir	9	29.7
K	1	4.3	Nb	5	19.5	Pt	10	30.2
Ca	2	8.0	Mo	6	23.0	Au	11	29.9
Sc	3	12.9	Ru	8	28.5	Hg	12	
Ti	4	17.7	Rh	9	30.0	Tl	3	12.0
V	5	22.3	Pd	10	30.6	Pb	4	13.5
Cr	6	26.2	Ag	11	29.8	Bi	5	13.9
Mn	7	28.0	Cd	12	27.7			

*Amorphous carbon (density: 1.8g/cm^3).

$$b_j = 53.4 - 20.8 \cdot n_j^v \quad \cdots\cdots (16)$$

ρ_j : Density of matrix atom j (g/cm^3)

N_V : Number of valence electrons of matrix atom j

A_j : Atomic weight

Es_j : Plasmon energy (eV)

E_g : Band gap of matrix atom (eV)

The information on the valence electron, plasmon energy and band gap of the matrix atom is shown in **Tables 1** and **2**.

In the multi-element system, the average escape depth is given by the following equation by assuming that each composition element determines it in proportion to its density:

$$\frac{1}{\lambda_i(C_1, C_2, \cdots, C_m)} = \sum_{j=1}^{m} \frac{C_j}{\lambda_i^j} \quad \cdots\cdots (17)$$

In the actual calculation, when correcting the intensity of Auger peak with energy E_i, the $\lambda_i(C_1, C_2, \cdots, C_m)$ is obtained by averaging it using Eq. (17), after calculating the escape depths of electron with energy E_i in all the composition elements using Eg. (10). The average escape depth correction is also made by obtaining the escape depths λ_i in the standard sample of element i, and then calculating their ratios. In addition to this equation, some other equations that give the average escape depth of electron have also been proposed [6][7].

Backscattered electron correction $\gamma_i^0(E_p)/\gamma_i(E_p, C_1, C_2, \cdots, C_m)$

There are two kinds of Auger electrons, depending on the generating processes; one is excited by incident electron, the other is excited by the high-energy backscattered electron escaping from the surface. The influence from the backscattered electron increases as the accelerating voltage Ep of the incident electron and the atomic number of the element of the matrix part increase. Ichimura, Shimizu et al. quantitatively summarized the influence of these effects [8]. Referring to their work, the backscatter coefficient γ of the element of atomic number Z for the incident electron, which irradiates the sample at normal incidence, is expressed as

$$\gamma_i^0(E_p) = 1 + (4.35 - 3.93Z^{0.1})u^{-0.25} + 4.85Z^{0.1} - 5.45 \quad \cdots\cdots (18)$$

Here, u is the over-voltage ratio and is defined by

$$u = \frac{E_p}{E_b} \quad \cdots\cdots (19)$$

where E_p is the incident electron beam energy and E_b is the ionization energy of the element i necessary to scatter out the U shell electrons that is required to excite the UVW Auger electrons. **Figure 2** shows the graph of the backscattering coefficient γ.

In a multi-element system, we define the average atomic number as

$$\overline{Z} = \sum_{i=1}^{m} C_i Z_i \quad \cdots\cdots (20)$$

and substitute $\overline{Z}$ in Ep. (18) instead of Z, we can obtain the $\gamma_i(E_p, C_1, C_2, \cdots, C_m)$ in the same manner as for a pure element.

Table 2. The band gap E_g(eV) of the insulator and semiconductor at room temperature.

Material	E_g(eV)	Material	E_g(eV)	Material	E_g(eV)
Al_2O_3	9.0	InSb	0.165	ZnSb	0.50
$Si0_2$	9.1	ZnO	3.2	CdSb	0.45
LiF	11.8	ZnS	3.54	Bi_2S_3	1.3
TiO	3.03*1	ZnSe	2.58	Bi_2Se_3	0.27
C	5.4*2	ZnTe	2.26	Bi_2Te_3	0.13
Si	1.107	CdO	2.5 ± 0.1	Mg_2Sn	0.21
Ge	0.67	CdS	2.42	Zn_2As_2	0.93
Te	0.33	CdSe	1.74	Cd_2As_2	0.55
AlAs	2.2	CdTe	1.44	GaSe	2.05
AlSb	1.6	HgSe	0.30	GaTe	1.66
GaP	2.24	HgTe	0.15	InSe	1.8
GaAs	1.35	PbS	0.37	TlSe	0.57
GaSb	0.67	PbSe	0.26	Ga_2Te_3	1.1
InP	1.27	PbTe	0.25	α-In_2Te_3	1.1
InAs	0.36				

*1 at Absolute temperature 0 K. *2 Diamond.

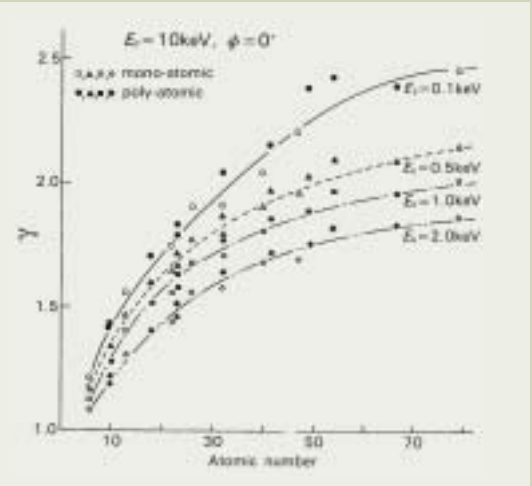

Fig. 2. Atomic number and backscattering coefficient (S. Ichimura, R. Shimizu et al. [8]).

Correction calculation involving matrix effect

Here, the procedure to perform the correction calculation involving the matrix effect is actually described.

Firstly, the peak deconvolution of a measured spectrum for a sample is made using the standard spectra of pure elements (with concentration of 100%). Then the concentration of each element (E_p,C_1, C_2,···, C_m) is obtained by the K-value method, from the ratio with the each standard spectrum intensity (I_i^0), which is supposed to be 1. This is the basic concentration used in the correction calculation.

$$C_1 = \frac{I_1}{I_1^0},\ C_2 = \frac{I_2}{I_2^0},\ \cdots,\ C_m = \frac{I_m}{I_m^0} \quad \cdots\cdots (21)$$

Next, we calculate the matrix functions (β_1 to β_m) by using the concentrations obtained above.

$$\beta_1(E_p, C_1, C_2, \cdots, C_m) = \frac{n_1^0}{n(C_1, C_2, \ldots, C_m)} \cdot \frac{\lambda_1^0}{\lambda_1(C_1, C_2, \ldots, C_m)} \cdot \frac{\gamma_1^0(E_P)}{\gamma_1(E_p, C_1, C_2, \ldots, C_m)} \quad \cdots (22)$$

$$\beta_2(E_p, C_1, C_2, \cdots, C_m) = \frac{n_2^0}{n(C_1, C_2, \ldots, C_m)} \cdot \frac{\lambda_2^0}{\lambda_2(C_1, C_2, \ldots, C_m)} \cdot \frac{\gamma_2^0(E_P)}{\gamma_2(E_p, C_1, C_2, \ldots, C_m)} \quad \cdots (23)$$

$$\vdots$$

$$\beta_m(E_p, C_1, C_2, \cdots, C_m) = \frac{n_m^0}{n(C_1, C_2, \ldots, C_m)} \cdot \frac{\lambda_m^0}{\lambda_m(C_1, C_2, \ldots, C_m)} \cdot \frac{\gamma_m^0(E_P)}{\gamma_m(E_p, C_1, C_2, \ldots, C_m)} \quad (24)$$

Using these correction functions, we correct the concentrations as follows:

$$C_1^{NEW} = \beta_1(E_p, C_1, C_2, \cdots, C_m) \cdot \frac{I_1}{I_1^0} \quad \cdots\cdots (25)$$

$$C_2^{NEW} = \beta_2(E_p, C_1, C_2, \cdots, C_m) \cdot \frac{I_2}{I_1^0} \quad \cdots\cdots (26)$$

$$\vdots$$

$$C_m^{NEW} = \beta_m(E_p, C_1, C_2, \cdots, C_m) \cdot \frac{I_m}{I_m^0} \quad \cdots\cdots (27)$$

The obtained results, C_1^{NEW}, C_2^{NEW},···,C_m^{NEW} cannot be fully corrected. Substituting these C_1^{NEW}, C_2^{NEW},···,C_m^{NEW} again in Eqs. (22) to (24) instead of C_1, C_2, ···,C_m the β_1, β_2,···,β_m are newly obtained, and then the newly corrected concentrations are obtained. By per-

forming these iteration calculations self-consistently until the differences between the values of C_1^{NEW}, C_2^{NEW},···,C_m^{NEW} and C_1, C_2, ···, C_m become small enough.

The concentrations obtained by the above procedures are the corrected concentrations involving the matrix effect. In the next section, some application examples of the quantitative correction calculation are presented.

Examples of Quantitative Analysis Considering Matrix Effect

Quantitative analysis of Fe_2B sample

Beginning with the quantitative analysis considering the matrix effect, Fe_2B built on the surface of Fe is analyzed. The results of the secondary electron image and the Auger spectra on the analyzed sample are shown in **Figs. 3** and **4**.

As a pre-processing, Ar sputtering at 3 keV is carried out for 30 seconds to remove the contaminations from the surface. After that, Auger spectra are measured using the 10 keV and 50 nA incident electron beam with a 0.6% energy resolution. It is found that Fe2B is built up at point-1 and that the region where some portion of the Fe_2B is replaced with carbide is present at point-2. **Figure. 5** shows the Auger mapping for the same image field.

Next, the peak deconvolution of the differential spectrum for the Auger spectra shown in Fig. 4 is carried out using the non-negative constrained least squares fitting method with the standard spectra of pure element. As a result, **Table 3** shows the contribution rates of standard spectra for each Auger spectra. These are equal to the atomic concentration for quantitative analysis.

Based on this result, the matrix-effect correction is carried out. The results of corrected atomic densities, and the calculated correction coefficients for atomic density, average escape depth and backscattered electron are shown in **Tables 4** and **5**, respectively.

From the results in Table 4, when the correction is made, the atomic density has been improved by 16%, 5% and 0.5% for point-1, point-2 and point-3, respectively, and all the sums of the quantitative results are within errors of a few percent. Looking at the amount of the matrix effect, it is found that each element requires a few to 20% correction, which cannot be neglected.

Now, if the compositions are considered from the atomic ratio of each element, they are shown as

(point-1) B:C:Fe = 3 : 0.2 : 7 →Fe_2B
(point-2) B:C:Fe = 1 : 1.5 : 7.5 →$Fe_2B_{0.5}C_{0.5}$
(point-3) C:Fe = 1 : 22 →Fe

Then the composition at each region is found. At point-2, in particular, the composition is found by making the matrix correction to be Fe_2BC containing C and B, roughly 1:1.

In order to check these analysis results, quantitative analyses at point-1 and 2 are carried out using the EPMA. The results are shown in **Table 6**.

Looking at the results of Table 6, the AES quantitative analysis results after the matrix correction are found to be close to the quantitative analysis results of EPMA. It is shown that this matrix correction is very important and effective in the quantitative analysis of Auger spectra.

Next, in order to study the validity of this correction to fine particles, unlike bulk sample

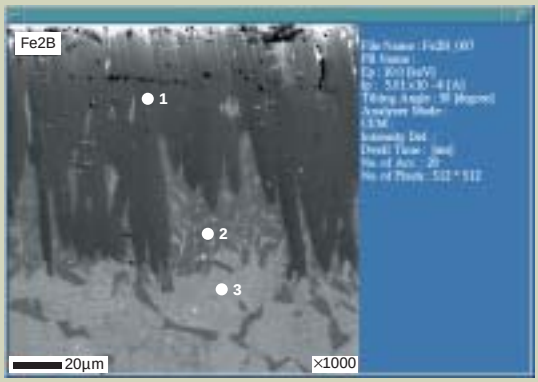

Fig. 3. Secondary electron image of Fe_2B and Auger analysis points (point-1 to 3).

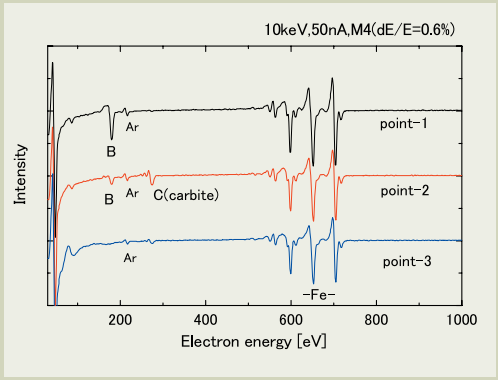

Fig. 4. Auger spectra in Fe_2B sample (point-1 to 3).

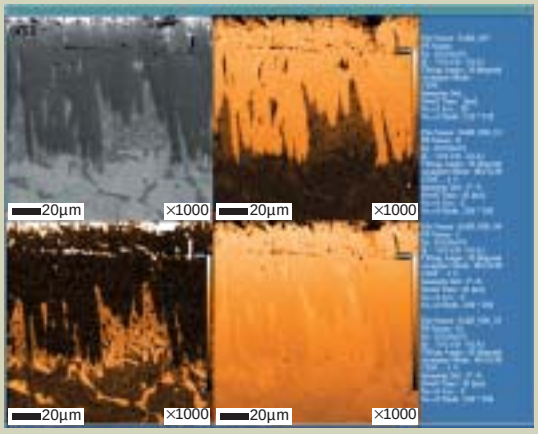

Fig. 5. Auger maps for Fe_2B (B, C, Fe).

Table 3. Ratio of each standard spectrum by peak deconvolution (I_i/I_i^0).

Element	Point-1	Point-2	Point-3
B	0.3478	0.09065	0
C	0.02618	0.1601	0.04086
Fe	0.8472	0.8146	0.8762
Sum	1.221	1.065	0.9170

Incident electron beam:10 keV, 50 nA, Tilt=30°, M4 (dE/E=0.6%).

Table 4. Atomic concentrations after matrix-effect correction at each point ($\beta \cdot I_i/I_i^0$).

Element	Point-1		Point-2		Point-3	
	Initial value	Corrected value	Initial value	Corrected value	Initial value	Corrected value
B	0.3478	0.3161	0.09065	0.0892	0	0
C	0.02618	0.0209	0.1601	0.1389	0.04086	0.0380
Fe	0.8472	0.7243	0.8146	0.7590	0.8762	0.8843
Sum	1.221	1.063	1.065	0.9871	0.9170	0.9223
(Sum-1)%	(+22.1)	(+6.3)	(+6.5)	(–1.2)	(–8.3)	(–7.8)

Table 5. Correction coefficients for each element.

Correction coefficients	Point-1			Point-2			Point-3		
	B	C	Fe	B	C	Fe	B	C	Fe
Atomic density (n_i/n_i^0)	1.30	1.04	0.783	1.52	1.22	0916	1.78	1.42	1.07
Average escape depth (λ_i/λ_i^0)	1.07	1.09	1.03	0.993	1.02	0.968	0.928	0.957	0.919
Backscattered electron (γ_i/γ_i^0)	0.655	0.704	1.06	0.651	0.700	1.05	0.634	0.683	1.03
Matrix function (β)	0.909	0.799	0.855	0.984	0.867	0.932	1.05	0.930	1.03

such as Fe_2B, quantitative analyses of the precipitated particles on lead-free solder are carried out.

Analysis of the precipitated material on lead-free solder

The analysis of the precipitated material on lead-free solder was made in the previous report, "Peak Deconvolution Analysis in Auger Electron Spectroscopy" [1][2]. The Cu-Ag-Sn-Bi based solder is not a uniform substance but is precipitated divided into a particle of Ag, Sn and Bi, and a particle of Cu and Sn. The quantitative analysis of each of these particles was previously carried out, by using peak deconvolution. However, the errors for the quantitative analysis results reached 40% at maximum, because the correction calculation of the matrix effect was not done. Now, the quantitative analysis is carried out again by making the matrix correction calculations. **Figs. 6** and **7** show the SEM image and Auger spectra of the Cu-Ag-Sn-Bi based solder.

For the spectrum at each point shown in Fig. 7, the matrix correction calculation is made using the ratio of the spectrum, which is obtained by peak deconvolution and standard spectrum as the initial value. **Table 7** shows the results.

Looking at Table 7, the quantitative correction values deviate more than 20% for point-1 and point-2, but for point-3, the errors in the matrix part are only 3.4%.

The reasons why the correction calculation did not work properly may be due to the following two causes.

Firstly, the effect of the surface roughness is pointed out. In the calculation process, the surface roughness for the standard sample and the sample in question is regarded roughly the same, and the ratio for the surface roughness factors (R/R_0) is assumed to be 1. However, the secondary electron image of Fig. 6 clearly shows that the particle surfaces at point-1 and point-2 are more rugged than the surface of the matrix part.

Secondly, the difference of the crystal state of the particles between the standard sample and the sample in question is pointed out. The intensity of the Auger spectrum differs for places with the different channel contrast, for example, even measuring the same standard Fe sample. Generally, the intensity of the Auger spectrum differs for places with different contrasts in the secondary electron image. Thus, the Auger spectrum includes information on not only the peak position but also the intensity that makes its interpretation difficult.

In the future, this matrix correction will be applied to the quantitative analysis of thin films or other particles as the measurement objects, and the Auger spectra will be analyzed theoretically and experimentally in more detail.

Table 6. Comparison with the analysis results by EPMA (the standardless quantitative analysis).

Element	Point-1			Point-2		
	EPMA* (wt%)	EPMA* (at%)	AES correction (at%)	EPMA* (wt%)	EPMA* (at%)	AES correction (at%)
B	7.729	29.6062	31.61	3.007	12.6379	8.92
C	0.996	3.4342	2.09	3.723	14.0855	13.89
Fe	90.311	66.9597	72.43	90.066	73.2766	75.90
Sum	99.036	100.0000	106.3	96.796	100.0000	98.71

*Incident electron beam:15 keV, 45.6 nA

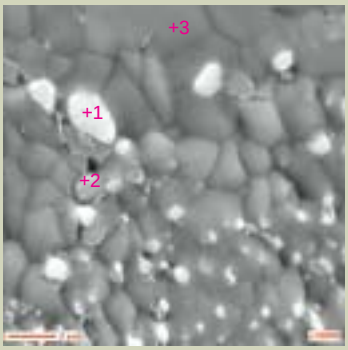

Fig. 6. SEM image of the Cu-Ag-Sn-Bi based solder and the analysis points.

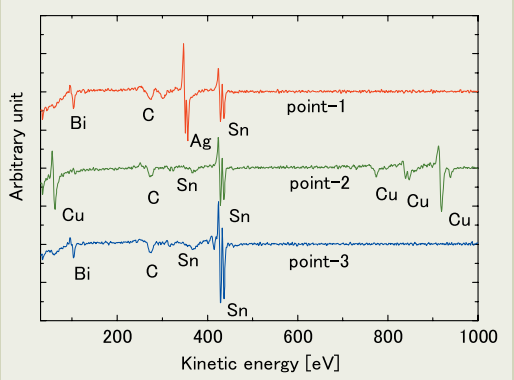

Fig. 7. Auger analysis result of the Cu-Ag-Sn-Bi based solder (Incident electron beam 10 keV, 10 nA, M4 (dE/E=0.6%).

Table 7. Atomic concentrations after matrix-effect correction at each point.

Element	Point-1		Point-2		Point-3	
	Initial value	Corrected value	Initial value	Corrected value	Initial value	Corrected value
C	0.464	0.418	0.479	0.399	0.528	0.459
Cu	0.0298	0.0291	0.681	0.607	0.0112	0.0103
Ag	0.487	0.352	0	0	0	0
Sn	0.355	0.236	0.436	0.267	0.658	0.418
Bi	0.302	0.177	0	0	0.248	0.8843
Sum	1.638	1.212	1.596	1.273	1.455	1.0336
(Sum-1)%	(+63.8)	(+21.2)	(+59.6)	(+27.3)	(+44.5)	(+3.4)

Incident electron beam:10 keV, 50 nA, M4 (dE/E=0.6%).

Conclusions

The quantitative analysis with Auger spectrum generally uses the relative sensitivity factor method that offsets and averages errors. As the precision depends greatly on the standard spectrum obtaining the relative sensitivity factor, the appropriate standard sample for the measuring sample should be selected. With this method, however, it is not possible to make a truly meaningful quantitative evaluation of the Auger spectrum, because it cancels out all the physical and chemical information on the sample carried in the spectrum. Thus, in this report, the quantitative analysis of Auger spectrum has been made correcting the matrix effect for the peak-deconvoluted Auger spectrum by using the K-value method, which is usually performed in EPMA or a similar instrument.

The obtained results enable the quantitative analysis of Fe_2B with errors of a few percent, and agree well with the results of EPMA. On the other hand, the quantitative analysis of the Cu-Ag-Sn-Bi based lead-free solder is also made with the similar condition obtaining the quantitative analysis with errors of 3% for matrix part. However, for the precipitated substance on the lead free solder, the errors become as large as 30%. For coping with this circumstance the uncertain factors such as the surface roughness factor should be investigated that will help to enhance the quantitative analysis precision further.

As mentioned above, the Auger spectrum analyses have some unknown areas to study yet, and studying and developing these areas will bring us new insight into the Auger electron spectroscopy.

References

1. Tsutsumi K., Ikeo N. and Nagasawa Y.: JEOL EPMA and Surface Analysis User's Meeting Material (AP92) (in Japanese).
2. Tsutsumi K., Ikeo N. and Nagasawa Y.: *JEOL news*, **37E**, 66 (2002).
3. Sekine T., Hirata K. and Mogami A.: *Surface Science*, **125,** 391 (1983).
4. Tanuma S., C. J. Powell and D. R. Penn: *Surface Interface Analysis* **11,** 577 (1988).
5. Tanuma S., C. J. Powell and D.R. Penn: *J. Vac. Sci. Technol.* **A8,** 2213 (1990).
6. P. M. Seah and W. A. Dench: *Surface and Interface Analysis* **1,** 2 (1979).
7. J. C. Ashley and N. W. Williams: *Radiation Res.* **81,** 364 (1980).
8. Ichimura S., Shimizu R. and J. P. Langeron: *Surface Science* **124,** 49 (1983).

Applications of Micro-Area Analysis Used by JPS-9200 X-ray Photoelectron Spectrometer

Yoshitoki Iijima

Application & Research Center, JEOL Ltd.

Introduction

Recently, with advances in the development of nanotechnology, the analysis materials, such as semiconductor device, are increasingly thinner and smaller. Moreover, without obtaining precise information on the chemical bonding on the surfaces of these newly developed materials, the progress of research and development of newly developed materials or products might be seriously affected.

The X-ray Photoelectron Spectrometer (XPS) is very useful surface analysis method since XPS provided the chemical bonding state information for the material surface analysis method. However, because the photoelectron intensity obtained by micro analysis for an analysis region less than 100 µm in diameter is very weak, the objective analysis positions are difficult to identify, or other reasons, the micro XPS analysis has seen little demand until a few years ago. As the technology has progressed recently, these problems are being solved, and micro XPS has now become widely used for practical purposes. Unfortunately, because the various measurement data in the micro XPS are exclusively used for troubleshooting analyses, useful analysis examples or data on materials showing the effectiveness of the micro XPS are not widely known except for a few measurements by limited number of researchers. So, many researchers are asking themselves, "What can we do by using the micro XPS ?"

JEOL Ltd., has dedicated great efforts to research and development of the micro XPS for many years, and beginning in fiscal year 2000, we have started to deliver the JPS-9200, which is a micro XPS instrument for researchers and those who engage in the material analysis. In this paper, some application examples of micro analysis measured by the JPS-9200 are introduced. We hope that these application data will contribute to the progress of the application research of XPS using the micro XPS from now on.

Purpose of micro-area analysis by using XPS

The purposes of micro-area analysis by using XPS are as follows;

1) Analysis of the composition and/or chemical bonding state of faintly discolored or abnormal parts
2) Analysis area is small less than several hundred µm square.

In general, the above reasons, micro-area surface measurement are done by using micro-area analysis XPS. However, some XPS analyses require also analyzing the changes in the local chemical state on the surface of a polymer or segregation of a compound. Actually, such sample analyses are frequently carried out in the XPS. In many cases, those samples have the same color for the main body and the chemically changed parts. These situations allow conducting only a macro analysis for a region few µm in diameter, because it is usually not possible to locate the position to analyze. In some cases, however, it is not enough to analyze the surface chemical changes with macro analysis. Chemical bonding information of microscopic region must be obtained.

Figure 1 shows a wide scan spectrum of a fuel cell electrode measured in macro-area analysis (6 mm in diameter). As shown in the figure, the only elements detected are F and C, which are constituents of the Teflon-family high-polymer and carbon black, the materials of the electrode. **Figure 2** is the photograph of fuel cell electrode observed using optical microscope. In this photograph, no chemical changes (such as discoloration or segregation) can be observed. Consequently, micro analysis of such a sample is not allowed, but macro analysis of a region a few mm in diameter yields average information on the sample surface. **Figure 3** shows the concentration ratios of C-F bonding, whose peak is caused by the Teflon-family polymer, and C, whose peak is caused by the carbon black, measured at analysis areas of 6 mm, 1 mm, 200 µm and 30 µm in diameter. As shown in the Fig. 3, the concentration ratio is found to increase as the analysis size decreases. From this result, it is supposed that the Teflon-family polymer is localized on the surface of the sample. **Figures 4**, **5** and **6** show the photoelectron images by the photoelectron peak of C-F bonding in the regions of 6 mm × 6 mm, 2 mm × 2 mm and 400 µm × 400 µm, respectively. In the photoelectron image shown in Fig. 4, the distribution of C-F bonding state on the fuel cell electrode can hardly be observed. On the other hand, the distribution of C-F

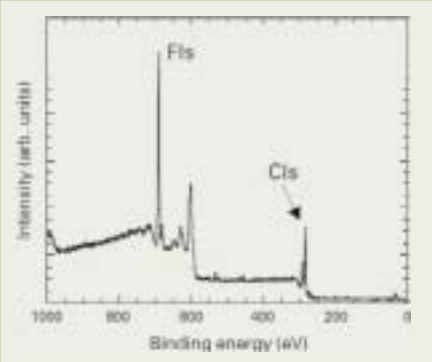

Fig. 1. Wide scan spectrum on the surface of an electrode.
Analyzing area: 6 mm in diameter.

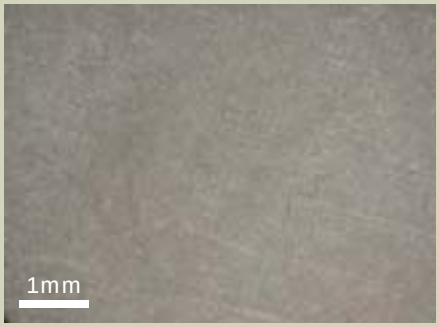

Fig. 2. Photograph of the central of the electrode observed using the optical microscope (The surface color is black and the shape changes are not observed).

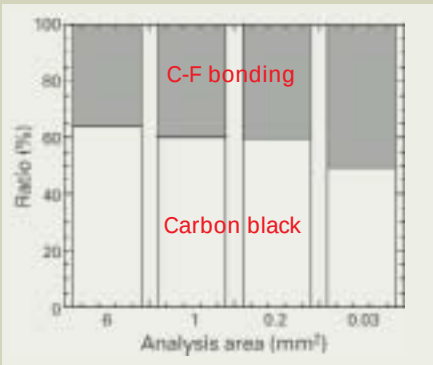

Fig. 3. Component ratio for C-F bonding state and carbon black in C_{1s} spectrum for each analysis region.

bonding begins to be observed in the 2 mm × 2 mm region, and it is clearly observed for the 400 µm × 400 µm region. These results proved that the distribution of the Teflon polymer, which cannot be observed using an optical microscope, is segregated on the surface of the electrode.

These results suggested that the micro analysis gives us different chemical bonding information on the surface for a substance whose chemical bonding information has so far been obtained only by the macro analysis. Therefore, micro analysis can also be effective for even a substance whose segregation positions cannot be identified by using an optical microscope or a similar apparatus as described above.

Summarizing the above discussions, the micro-area analysis using XPS can be useful not only for analyzing a tiny discolored part or troubleshooting of products, but also for properly grasping the segregation of a surface that appears to be uniform, and developing new materials.

Application of micro-area analysis using by XPS, JPS-9200

Example of corrosion analysis

The micro XPS analysis is mainly carried out for troubleshooting of a product. **Figure 7** shows an optical photomicrograph of Cu alloy lead frame. In this photograph, it is found that the surface is discolored. This sample, which is Ag plated on Cu, has become discolored due to some cause. This discoloration is different from position to position on the sample, and analysis of the causes is requested for XPS. The discolored places indicated by Points A, B and C are measured by using micro XPS. **Figure 8** shows a wide energy spectrum measured at Point A with a region 200 µm in diameter. The elements detected in the region 200 mm in diameter are Ag, Cu, O, S and C. As the analysis region at Point A occupies 2 mm × 1 mm, an analysis diameter of 200 µm is good enough for ordinary analysis. **Figures 9**, **10** and **11** show wide scan spectra measured for analysis regions 50 µm in diameter at

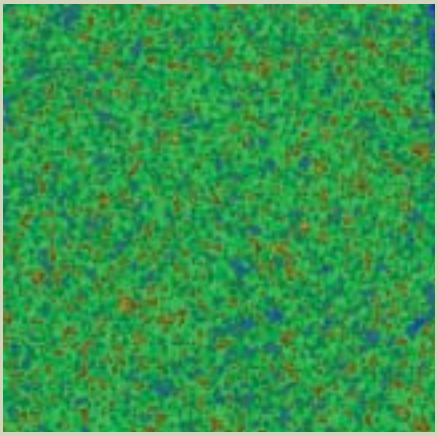

Fig. 4. Photoelectron image of C-F bonding. Scan region is 6 mm × 6 mm.

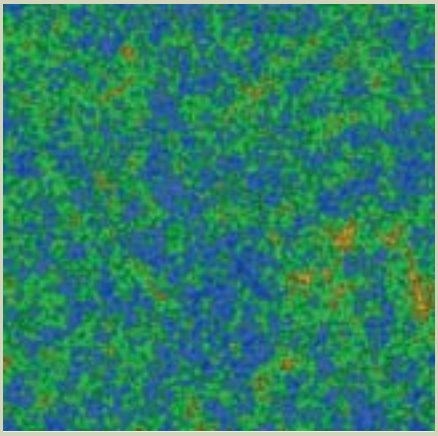

Fig. 5. Photoelectron image of C-F bonding. Scan region is 2 mm × 2 mm.

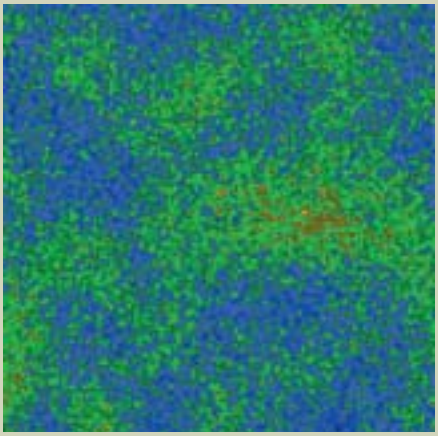

Fig. 6. Photoelectron image of C-F bonding. Scan region is 400 µm × 400 µm.

Fig. 7. Photograph of Cu alloy lead frame observed by optical microscope. A, B and C are analyzed points by XPS.

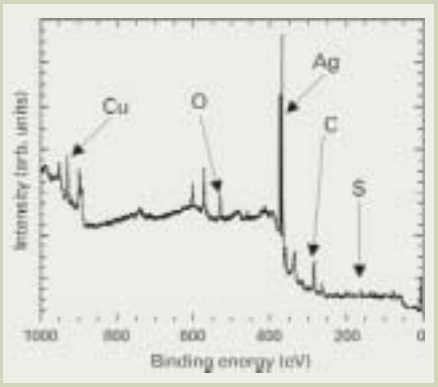

Fig. 8. Wide scan spectrum measured with analysis region 200 µm in diameter at Point A.

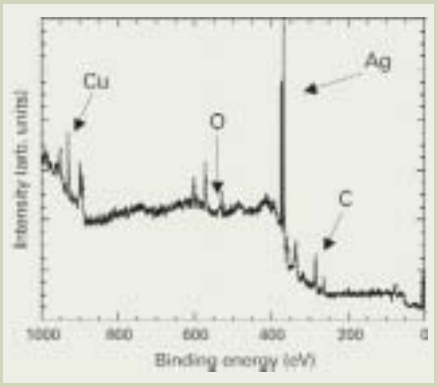

Fig. 9. Wide scan spectrum measured with analysis region 50 µm in diameter at Point A.

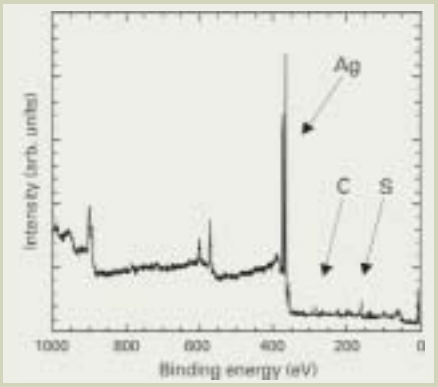

Fig. 10. Wide scan spectrum measured with analysis region 50 µm in diameter at Point B.

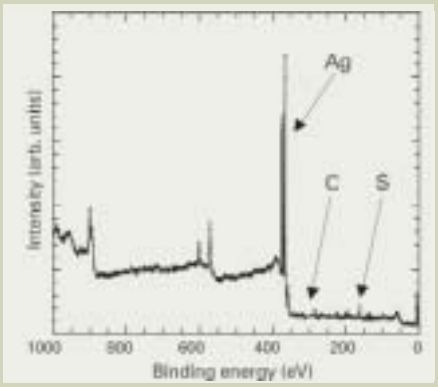

Fig. 11. Wide scan spectrum measured with analysis region 50 µm in diameter at Point C.

Points A, B, and C, respectively. The measurement conditions for these photoelectron spectra are as follows: x-ray used is MgKα, x-ray radiation power is 300 W, and analyzer pass energies are 50 eV and 10 eV for wide scan spectrum and narrow scan spectrum (energy resolutions are 1.8 eV and 0.9 eV), respectively.

The detected elements from each point are as follows:

Measurement point	Detected elements
A	Ag, Cu, O, C
B	Ag, O, C, S
C	Ag, O, C, S

From the above results, the element S, which is detected in Fig. 8 (200 µm in diameter), is only detected at Points B and C, and not detected at Point A, in the analysis region 50 µm in diameter. These results are caused by the difference of element distribution near point A observed in the visual field of the optical microscope, and suggest that the analysis researchers must be carried out in a region as small as possible for such samples.

Furthermore, in Figs. 10 and 11, the amounts S detected at Points A and B are different from each other. The amount of S at Point B is found to be slightly larger than that at Point C. **Figure 12** shows the curve-fitting spectrum of S_{2p} spectrum at point B. The $S_{2p3/2}$ peak position is 161.9 eV, and $Ag_{3d5/2}$ peak position is 368.3 eV from the narrow scan spectrum. Hence, the chemical bonding state of S at Point A is assigned to be Ag_2S. Based on this result as well as the measured wide scan spectrum at each point, the photoelectron images at the $Ag_{3d5/2}$ peak and S_{2p}(the energy position is adjusted to the peak belonging to Ag_2S) are shown in **Figs. 13** and **14**, respectively. These imaging results indicate that Ag is abundant in the same discolored region that contains Point B. Similarly, S is also abundant in the same discolored region that contains Point B. Moreover, it is also found from these imaging results that the region that contains Point B consists of Ag_2S.

For the reason stated above, the chemical bonding information on the discolored part can be properly obtained by measuring with the analysis region as small as possible.

Example of surface analysis discolored part on polymer

Polymers are among the most frequently measured samples in XPS. Generally, XPS analysis for the surface of a polymer is useful for clarifying the differences in wetting ability, causes of discoloration, and other phenomena. In some cases, however, it is useful for clarifying the chemical changes in the surface bonding state after irradiated with laser light or an ion beam.

We made the sample by sputtering Ar ion randomly on the surface of PET (polyethylene terephthalate) film, and investigated how to find the sputtered position and analyze the sample using XPS. **Figure 15** shows the O_{1s} photoelectron image on the 7 mm × 7 mm region around the position on which the Ar ions seem to have been sputtered. The analysis region is 30 µm in diameter for each position. Generally, when Ar ions are sputtered on the surface of a PET-like polymer, it releases oxygen from the C-O or COO bond, which is present in the constituent functional group. Hence, a photoelectron spectrum with reduced oxygen intensity can be observed. In Fig. 15, it is shown that the position with reduced oxygen intensity corresponds to the position sputtered by the Ar ion beam.

Figure 16 shows line spectra (C_{1s} and O_{1s} spectra) between the two points, a and b, indicated in Fig. 15. In this figure, the bottom and top lines correspond to the points a and b, respectively. Although the CH peak position is observed at 285.0 eV, it shifts to 284.0 eV as the measuring position moves to point b. Also, C-O and COO groups intensities decrease markedly as the measuring position moves from point a to point b. Similar phenomena are also observed for O_{1s} spectra.

Figure 17 shows the concentration distributions of O and C (in atomic%) when these line scans are carried out. As shown in the figure,

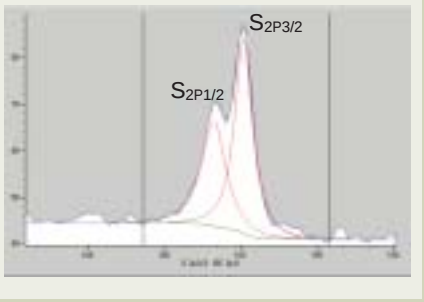

Fig. 12. S_{2p} curve-fitting spectrum measured at Point B.
$S_{2p3/2}$ peak position is 161.9 eV.

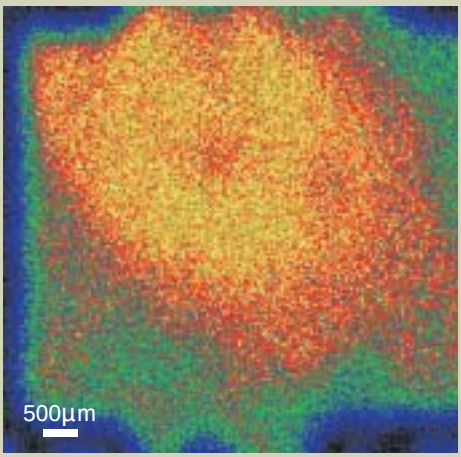

Fig. 13. Photoelectron image of Ag.

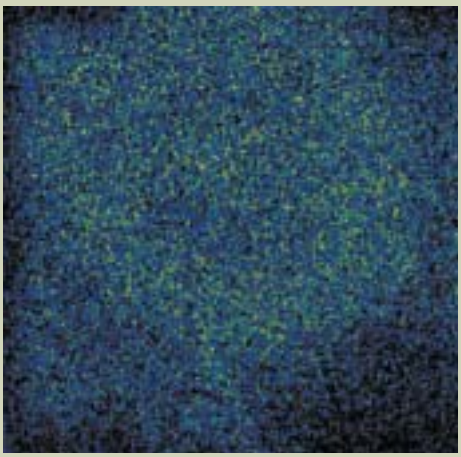

Fig. 14. Photoelectron image of S (energy value is adjusted to the peak of Ag_2S.

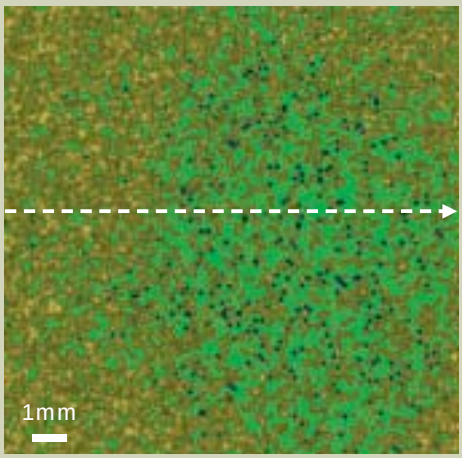

Fig. 15. O_{1s} photoelectron image (after Ar-ion sputtering on the PET film).

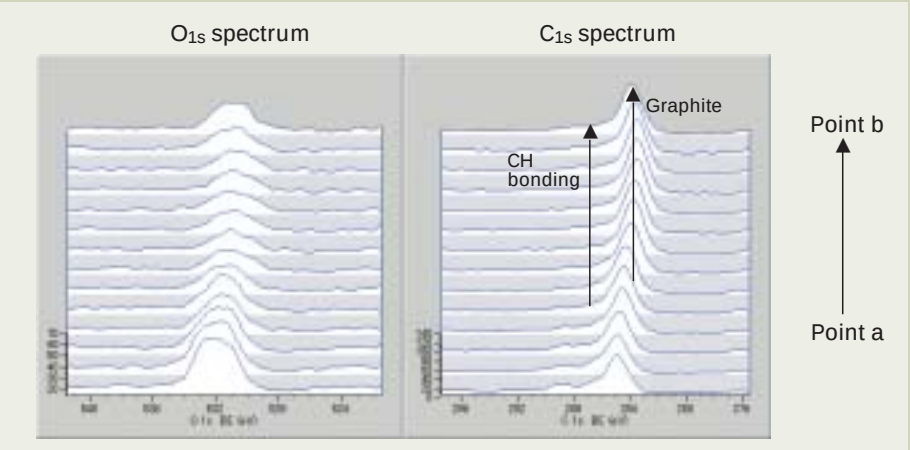

Fig. 16. O_{1s} and C_{1s} line scan spectra between point a and point b.

conspicuous decrease in the oxygen amount and accompanying increase in the carbon amount can be observed at the measuring positions 2 mm or farther from the point a indicated in Fig. 15.

For the sample mentioned above, it is found that the region sputtered by the Ar ion beam is 3 to 4 mm in the direction of the X-axis (wide) and 6 mm in the direction of the Y-axis (long), and that the most strongly sputtered position is at 3.5 mm from point a on the a-b line.

Thus, in the micro analysis of a sample whose analysis position is difficult to identify, it is possible to carry out the measurement at a precise analysis position by identifying the appropriate analysis position using macro-area imaging measurement as well as line measurement or other similar ones, and finally making the photoelectron spectrum measurement at the goal.

Example of electrode surface analysis

Although fuel cell have been developed since several decades ago, interest in them has increased recently due to environmental problems. The fuel cell is a direct power-generation system with ideal energy transformation efficiency of nearly 100%, and classified as follows by the kind of fuel, electrolyte and method.

- Hydrogen-oxygen fuel cell: fuel
- Solid electrolyte fuel cell: electrolyte
- Gas-diffusion fuel cell: method

Fuel cells are used mainly for space projects such as space shuttle, submarine operation boat, electric automobiles, and central power stations.

One of the most serious problems in using fuel cells is deterioration, or lifetime of the electrode. Since the fuel cell makes chemical reactions that occur on the surface of the electrode, material changes on the electrode cannot be avoided. Hence, it is possible to enhance the performance of the fuel cell by analyzing in detail how the surface of the electrode changes with chemical reactions (discharges). For this purpose, electrode are widely evaluated and analyzed by using various analytical instruments.

Figure 18 shows the electrode part of the gas-diffusion fuel cell, which is used for the present measurement. The surface structure of the electrode is diagrammed schematically in **Fig. 19**. The Teflon-family polymer used in this measurement has no CF_3 bonding at the ends, but has abundant CF bonding at the side chains. Therefore, unlike ordinary Teflon, it is a high polymer with peaks in the spectrum indicating the presence of CF_2 and CHF bonding. Such a Teflon-family polymer mixed with carbon black constitutes the substance of the electrode.

The purpose of analyzing such an electrode surface by using XPS is to analyze the changes (clarifying deterioration mechanism) of the Teflon-family polymer before and after the chemical reaction as well as the changes of added catalyst. By considering the photograph of Fig. 2 and the surface structure of the electrode shown in Fig. 19, the analysis region generally takes up a wide area a few mm in diameter from which the average information is obtained. However, as described in previous section, the Teflon-family polymer is evidently segregated on the surface. Consequently, by analyzing the chemical bonding state of the segregated Teflon-family polymer, information on the state changes of the electrode accompanying its reaction (after discharge) can be obtained.

The electrode shown in Fig. 18 is made by mixing the Teflon-family polymer and carbon black first, putting it between Al plates, and then pressing it at high temperature (380°C). Three electrode samples were used in the present micro analyses: (1) after mixing, (2) after pressing, and (3) after discharging. **Figures 20**, **21** and **22** show the results of imaging measurement of the CF bonding (F_{1s} photoelectron) in the 400 µm × 400 µm region on these electrode surfaces. The distribution of F on the electrode sample surface after mixing extends over the whole sample surface. After

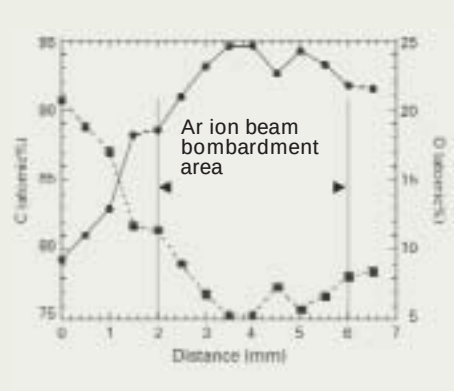

Fig. 17. Concentration distributions of O and C between two points, a and b.

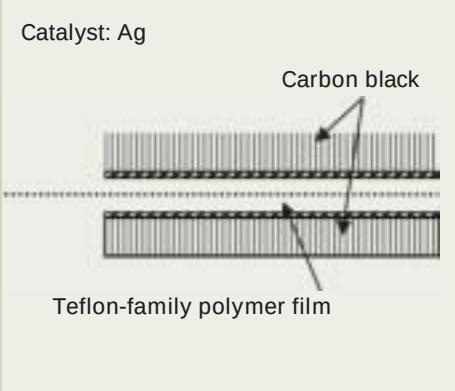

Fig. 18. Structural diagram of fuel cell electrode.

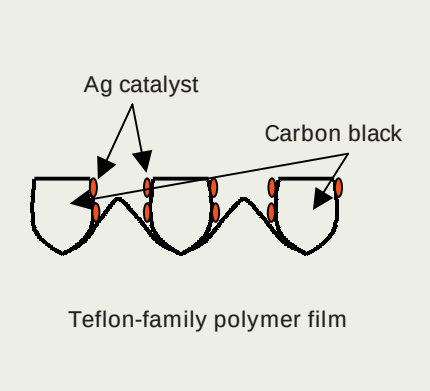

Fig. 19. Structural diagram of electrode surface.

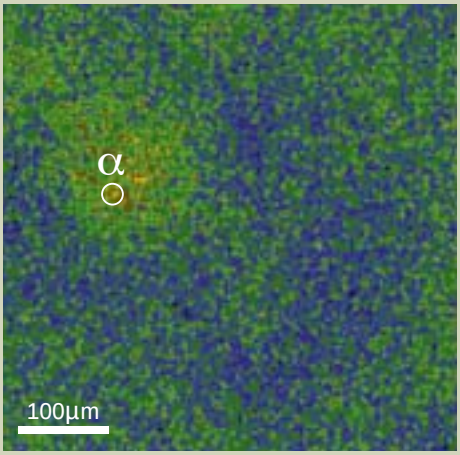

Fig. 20. C-F bonding state image after mixing (1).

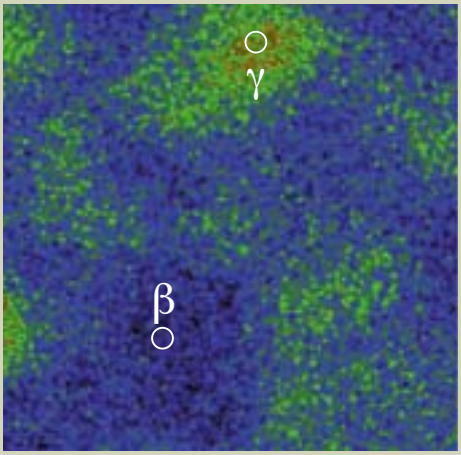

Fig. 21. C-F bonding state image after pressing at high temperature (2).

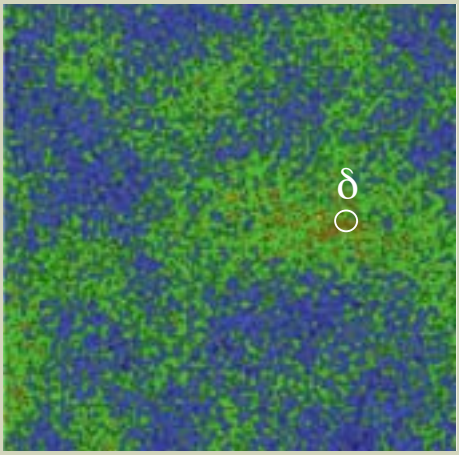

Fig. 22. C-F bonding state image after discharging (3).

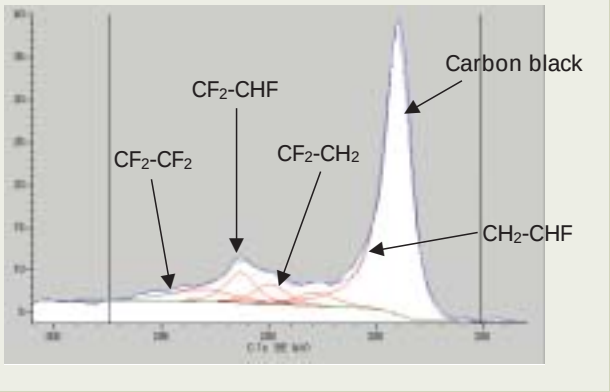

Fig. 23. C_{1s} spectrum at point α (after mixing) (curve-fitting spectrum).

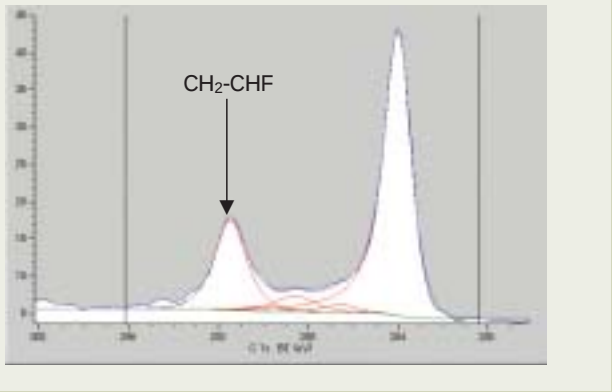

Fig. 24. C_{1s} spectrum at point β (after pressing at high temperature) (curve-fitting spectrum).

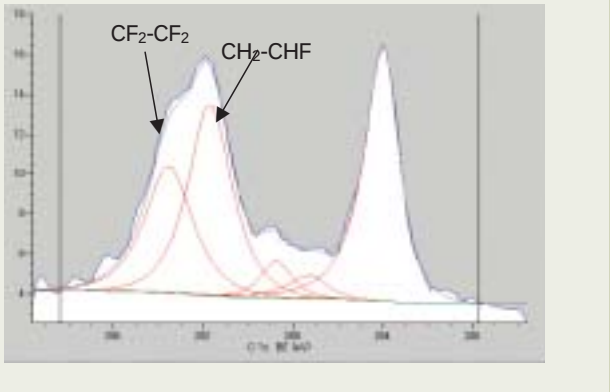

Fig. 25. C_{1s} spectrum at point γ (after high temperature) (curve-fitting spectrum).

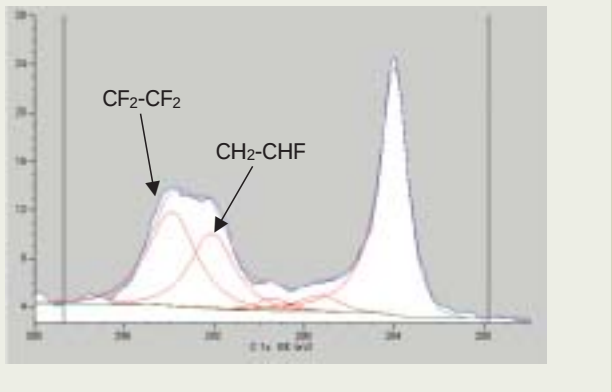

Fig. 26. C_{1s} spectrum at point δ (after discharging) (curve-fitting spectrum).

pressing at high temperature, segregation in regions less than or equal to 100 μm in diameter can be observed. After discharging, however, the distribution of F begins to spread similarly like after mixing (1). In order to investigate the chemical bonding states in these distributions of F, the C1s spectrum measurement was carried out at every point shown in the **Fig. 23**. The analysis diameter at each point was 30 μm.

Figure 23 shows the result at the electrode (point α) after mixing. As shown in the **Fig. 24**, a strong peak at 284.0 eV caused by carbon black is observed, and other peaks related to the C-F bonding are found to be minor. By using spectrum curve fitting, the observed peaks caused by the Teflon-family polymer are identified as CF_2-CF_2, CF_2-CHF, CF_2-CH_2 and CHF-CH_2. From the peak intensities of these peaks obtained by the spectrum curve fitting, the main component is found to be CF_2-CHF bonding state, whose peak corresponds to the side-chain functional group in the Teflon-family polymer.

Figure 24 shows the analysis of C_{1s} spectrum of the electrode surface after pressing at high temperature. At the position with lower F concentration (point β), the CHF-CF_2 bonding is observed to be the main component. Conversely, at the position with higher F concentration (point γ), both CHF-CF_2 and CF_2-CF_2 are observed to be the main components (**Fig. 25**). These two bonding components are considered to be the main components constituting the Teflon-family polymer. Hence, it is found that pressing at high temperature after mixing localizes the Teflon-family polymer on the electrode surface.

Figure 26 shows the analysis of C_{1s} spectrum of the electrode surface (point δ) after discharging. As shown in the Fig. 26, both CHF-CF_2 and CF_2-CF_2 are observed to be the major components as observed at point γ after pressing at high temperature. Of these two components, the amount of the CF_2-CF_2 bonding is observed to be higher than that of CHF-CF_2. Moreover, the amounts of the components caused by the Teflon-family polymer are conspicuously lower compared with those of the point γ after pressing at high temperature, and the surface distributions of these components are spread more widely than after pressing at high temperature.

Iijima, et al. reported that the side-chain components in the Teflon-family polymer decompose and change to CF_2-CF_2 bonding after discharging [1,2]. Moreover, from SEM observation of the electrode after discharge, it is reported that fibers are produced locally by the decomposition of the Teflon-family polymer [1,2].

The above results suggest that after discharging, the Teflon-family polymer decomposes and distributes on the surface a compound with CF_2-CF_2 bonding as the main component.

Conclusions

In the present investigation, various materials have been analyzed by using micro-area analysis XPS. The results obtained are different from the macro-area analysis results that had been obtained so far. For XPS analysis of materials, in particular, such as an electrode, whose analysis position cannot be identified by surface shape or a difference of color using optical microscopy, the micro-area XPS analysis can clearly show the difference of the chemical-bonding state in their images or spectra.

The JPS-9200 can carry out imaging measurements at scales ranging from macro area to micro area, and thus enables us to make proper XPS analyses for surface segregation, difference of chemical-bonding states between parts having the same color, and so forth.

From now on, with the progress of application research for various materials by micro-area analysis XPS, we hope that more useful chemical information about the local surface can be obtained.

References

1. Y. Iijima, T. Tazawa and N. Furuya.: *J. Korean Vacuum Society*, **9**, *S2*, 71(2000).
2. Y. Iijima, T. Tazawa and N. Furuya.: The 3rd Korea-Japan International Symposium on Surface Analysis, Kyongju, 16 (2000).

Introduction of New Products

Field Emission Electron Microscope

JEM-2100F

The field-emission electron gun (FEG), which provides an electron beam with high brightness and high coherence, is essential for high-resolution observation and nano-area analysis. The JEM-2100F, featuring advanced digital operation, is an integrated TEM that gives full play to its various functions.

- Point resolution : 0.19 nm
- Accelerating voltage : 160, 200 kV
- Magnification : 50 to 1,500,000

Scanning Electron Microscope

JSM-6060LV/JSM-6060

JSM-6060 is the high performance general purpose SEM with the optics and the operation software basically same as the one developed for JSM-6460. JSM-6060 is packaged in a small console to allow more freedom in layout. The completely automated electron gun and the JEOL unique zoom condenser lens, which allow optimization of the optics quickly, make the operation comfortable.
Also, a low vacuum (LV) version JSM-6460LV and an analytical SEM version JSM-6460A/JSM-6460LA are available.

- Resolution : 3.5 nm (LV : 4.0nm)
- Accelerating voltage : 0.5 to 30 kV
- Magnification : 5 to 300,000

Electron Beam Lithography System

JBX-3030MV

The JBX-3000MV is an electron beam lithography system for mask/reticle fabrication that meets the design rule of 100 to70 nm. This system features pattern writing with high speed, high accuracy and high reliability, achieved by high-end technology

- Accelerating voltage : 50 kV
- Electron gun emitter : LaB_6 single crystal
- Workpiece dimension : up to 178 mm square
- Field stitching accuracy : ±9 nm
- Overlay accuracy :±12 nm

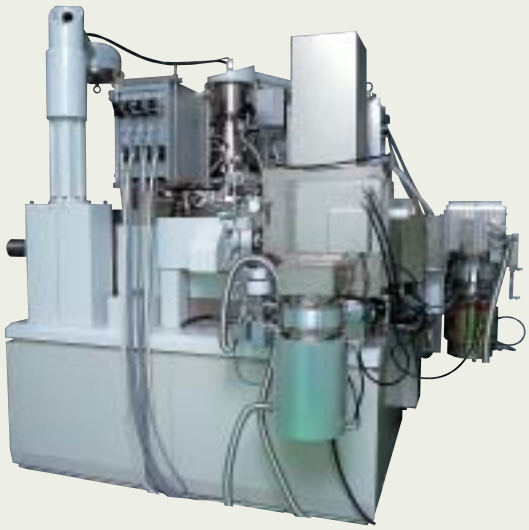

Certain products in this brochure are controlled under the "Foreign Exchange and Foreign Trade Law" of Japan in compliance with international security export control. JEOL Ltd. must provide the Japanese Government with "End-user's Statement of Assurance" and "End-use Certificate" in order to obtain the export license needed for export from Japan. If the product to be exported is in this category, the end user will be asked to fill in these certificate forms.

ISO 9001:2000 & 14001:1996 REGISTERED FIRM
DNV Certification B.V., THE NETHERLANDS
ISO 9001 Certificated
ISO 14001 Certificated

http://www.jeol.co.jp/

JEOL Ltd. 1-2 Musashino 3-chome Akishima Tokyo 196-8558 Japan Sales Division ☎(042)528-3353 FAX(042)528-3386

ARGENTINA
COASIN S. A. C. I. yF.
Virrey del Pino 4071,
1430 Buenos Aires, Argentina
Telephone: (11) 4552-3185
Facsimile: (11) 4555-3321

AUSTRALIA & NEW ZEALAND
JEOL (AUSTRALASIA) Pty. Ltd.
Unit 9, 750-752 Pittwater Road,
Brookvale, N. S. W. 2100, Australia
Telephone: (02) 9905-8255
Facsimile: (02) 9905-8286

AUSTRIA
LABCO GmbH
Dr.-Tritremmel-Gasse 8,
A-3013 Pressbaum, Austria
Telephone: (43) 2233-53838
Facsimile: (43) 2233-53176

BANGLADESH
A.Q. CHOWDHURY & CO. Pvt. Ltd.
Baridhara Central Plaza 87, Suhrawardy Avenue
2nd Floor Baridhara,
Dhaka-12129 Bangradesh
Telephone: 880 (2) 9862272, 9894583
Facsimile: 880 (2) 9880790

BELGIUM
JEOL (EUROPE) B. V.
Zaventem/Ikaros Business Park,
Ikaroslaan 7A, 1930 Zaventem, Belgium
Telephone: (2) 720 05 60
Facsimile: (2) 720 61 34

BRAZIL
FUGIWARA ENTERPRISES
INSTRUMENTOS CIENTIFICOS LTDA.
Avenida Itaberaba,3563
02739-000 Sao Paulo, SPI
Telephone: (11) 3983-8144
Facsimile: (11) 3983-8140

CANADA
JEOL CANADA, INC.
(Represented by Soquelec, Ltd.)
5757 Cavendish Boulevard, Suite 540,
Montreal, Quebec H4W 2W8, Canada
Telephone: (514) 482-6427
Facsimile: (514) 482-1929

CHILE
TECSIS LTDA.
Avenida Holanda 1248,
Casilla 50/9 Correo 9, Providencia, Santiago, Chile
Telephone: (2) 205-1313
Facsimile: (2) 225-0759

CHINA
JEOL Ltd., BEIJING OFFICE
Room No. B2101/2106,
Vantone New World Plaza,
No. 2 Fuwai Street, Xicheng District,
Beijing 100037, P. R. China
Telephone: (010) 6804 6321/6322/6323
Facsimile: (010) 6804 6324

JEOL Ltd., SHANGHAI OFFICE
Sanhe Building 11F2, Yan Ping Road,
No. 121,Shanghai 200042, P.R. China
Telephone: (021)6246 2353
Facsimile: (021)6246 2836

JEOL Ltd., GUANG ZHOU OFFICE
(South Power) World Trade Center Building
371-375, Huang Shi East-Road, Guang Zhou,
510095, P,R. China
Telephone: (020) 8778 7848
Facsimile: (020) 8778 4268

CYPRUS
MESLO Ltd.
Scientific & Laboraty Division,
P.O.Box 27709, Nicosia Cyprus
Telephone: 357-2-666070
Facsimile: 357-2-660355

EGYPT
JEOL SERVICE BUREAU
3rd Fl. Nile Center Bldg.,
Nawal Street, Dokki, (Cairo), Egypt
Telephone: (2) 3357220
Facsimile: (2) 3384186

FRANCE
JEOL (EUROPE) S. A.
Espace Claude Monet,
1, allee de Giverny 78290
Croissy-sur-Seine, France
Telephone: (1) 3015-3737
Facsimile: (1) 3015-3747

GERMANY
JEOL(GERMANY)GmbH
Oskar-Von-Miller-Strasse 1,
85386 Eching Germany
Telephone: (08165) 77346
Facsimile: (08165) 77512

GREAT BRITAIN & IRELAND
JEOL (U.K.) Ltd.
JEOL House, Silver court, Watchmead, Welwyn
Garden City, Herts AL7 1LT., England
Telephone: 01707-377117
Facsimile: 01707-373254

GREECE
N. ASTERIADIS S. A.
56-58, S. Trikoupi Str. P.O.Box 26140
GR-10022 Athens, Greece
Telephone: (1) 823-5383
Facsimile: (1) 823-9567

HONG KONG
FARMING LTD.
Unit 1009, 10/F., MLC Millennia Plaza
663 King's Road, North Point, Hong Kong
Telephone: (852) 2815 7299
Facsimile: (852) 25814635

INDIA
Blue Star Ltd. (HQ)
Analytical Instruments Department,
'Sahas'414/2 Veer Savarkar Marg,
Prabhadery Mumbai 400 025
Telephone: 91-22-5666 4065
Facsimile: 91-22-5666 4001

Blue Star Ltd.
Analytical Instruments Department,
E-44/12 Okhla Industrial Area,
Phase-11, New Delhi 110 020
Telephone: 91-11-5143 4000
Facsimile: 91-11-5149 4004

Blue Star Ltd.
Analytical Instruments Department,
7, Hare Street Calcutta 700 001
Telephone: 91-33-2248-0131
Facsimile: 91-33-2248-1599/

Blue Star Ltd.
Analytical Instruments Department,
Lakshmi Neela Rite Choice Chambers, 5,
Bazullah Road, 3rd Floor T. Nagar Chennai 600 017
Telephone: 91-44-2815/8846
Facsimile: 91-44-2815/8015

INDONESIA
PT. TEKNOLABindo PENTA PERKASA
J1. Gading BukitRaya,
Komplek Gading Bukit Indah Blok I/11,
Kelapa Gading Jakarta 14240, Indonesia
Telephone: (21) 45847057/58/59
Facsimile: (21) 45842729

IRAN
IMACO Ltd.
No. 141 Felestin Ave.,
P. O. Box 13145-537, Tehran, Iran
Telephone: (21) 6402191/6404148
Facsimile: (21) 8978164

ITALY
JEOL (ITALIA) S.p.A.
Centro Direzionale Green Office Via Dei Tulipani,
1, 20090 Pieve, Emanuele (MI), Italy
Telephone: (2) 9041431
Facsimile: (2) 90414353

KOREA
JEOL KOREA LTD.
Sunmin Bldg. 6th F1.,218-16, Nonhyun-Dong,
Kangnam-Ku, Seoul, 135-010, Korea
Telephone: (02) 511-5501
Facsimile: (02) 511-2635

KUWAIT
YUSUF I. AL-GHANIM & CO. (YIACO)
P.O. Box 435, 13005 - Safat, Kuwait
Telephone: 965-4832600/4814358
Facsimile: 965-4844954/4833612

MALAYSIA
JEOL (MALAYSIA) SDN. BHD.(359011-M)
205, Block A, Mezzanine Floor,
Kelana Business Center97,
Jalan SS 7/2, Kelana Jaya,
47301 Petaling Jaya, Selangor, Malaysia
Telephone: (3)-7492-7722
Facsimile: (3)-7492-7723

MEXICO
JEOL DE MEXICO S.A. DE C.V.
Av. Amsterdam #46 DEPS. 402
Col. Hipodromo Mexico 06100 D.F
Telephone: (5) 211 0672
Facsimile: (5) 211 0720

PAKISTAN
ANALYTICAL MEASURING SYSTEM (PVT) Ltd.
(AMS Ltd.)
F-8/1-5, KDA Scheme No. 1,
Main Tipu Sultan Road,
P.O. Box 10604, Karachi-75350, Pakistan
Telephone: (21) 4525185/4525186
Facsimile: (21) 4525187/4536406

PANAMA
PROMED S.A.
Parque Industrial Costa del Este
Urbanizacion Costa del Este
Apartado 6281, Panama, Panama
Telephone: (507) 269 0044
Facsimile: (507) 263 5622

PHILIPPINES
PHILAB INDUSTRIES INC.
7487 Bagtikan Street, SAV Makati, 1203 Metro,
Manila Philippines
Telephone: (2) 896 7218
Facsimile: (2) 897 7732

PORTUGAL
LABOMETER-SOC TECNICA DE
EQUIPAMENTO DE LABORATORIO. LDA.
Rua Duque de Palmela, 30-1°,
G, 1200 Lisboa, Portugal
Telephone: 00351 21 351 0180
Facsimile: 00351 1 352 5066

SAUDIARABIA
ABDULREHMAN ALGOSAIBI G.T.B.
Algosaibi Bldg., Airport Rd., P. O. Box 215,
Riyadh 11411, Saudi Arabia
Telephone: (01) 479-3000
Facsimile: (01) 477-1374

SCANDINAVIA
JEOL (Skandinaviska) A.B.
Hammarbacken 6 A, Box 716
191 27 Sollentuna, Sweden
Telephone: (8) 28 2800
Facsimile: (8) 29 1647

SERVICE & INFORMATION OFFICE
JEOL Norway
Ole Deviks vei 28, N-0614 Oslo, Norway
Telephone: 2264 7930
Facsimile: 2265 0619

JEOL Finlane
Ylakaupinkuja 2, FIN-02360 Espoo, Finland
Telephone: (9) 812 903 50
Facsimile: (9) 812 903 51

JEOL Denmak
Naverland 2, DK-2600 Glostrup, Denmak
Telephone: 4345-3434
Facsimile: 4345-3433

SINGAPORE
JEOL ASIA PTE. Ltd.
29 International Business Park,
#04-02A Acer Building,
Tower B Singapore 609923
Telephone: (65) 6565-9989
Facsimile: (65) 6565-7552

SOUTH AFRICA
ADI Scientific (Pty) Ltd.
109 Blandford Road, North Riding,Randburg
(PO box 71295 Bryanston 2021)
Republic of South Africa
Telephone: (11) 462-1363
Facsimile: (11) 462-1466

SPAIN
IZASA. S.A.
Aragoneses, 13,
28100 Alcobendas,
(Polígono Industrial) Madrid, Spain
Telephone: (91) 663-0500
Facsimile: (91) 663-0545

SWITZERLAND
JEOL(GERMANY)GmbH
Oskar-Von-Miller-Strasse 1,
85386 Eching Germany
Telephone: (08165) 77346
Facsimile: (08165) 77512

TAIWAN
JIE DONG CO., Ltd.
7F, 112, Chung Hsiao East Road, Section 1, Taipei,
Taiwan 10023, Republic of China
Telephone: (02) 2395-2978
Facsimile: (02) 2322-4655

THAILAND
BECTHAI BANGKOK EQUIPMENT
& CHEMICAL CO., Ltd.
300 Phaholyothin Rd. Phayathai,
Bangkok 10400, Thailand
Telephone: (2) 615-2929
Facsimile: (2) 615-2350/2351

THE NETHERLANDS
JEOL (EUROPE) B.V.
Tupolevlaan 28-A, 1119 NZ Schiphol-Rijk,
The Netherlands
Telephone: (20) 6533088
Facsimile: (20) 6531328

TURKEY
TEKSER KOLL. STI.
Acibadem Cad. Erdem Sok, Baver Art, N°6/1,
81010, Uskudar, Istanbul, Turkey
Telephone: 216-3274041
Facsimile: 216-3274046

UAE
Business Communications LLC.
P.O.Box 2534, Abu Dhabi UAE
Telephone: 971 2 6348495
Facsimile: 971 2 6316465

USA
JEOL USA, INC.
11 Dearborn Road, Peabody, MA. 01960, USA
Telephone: (978) 535-5900
Facsimile: (978) 536-2205/2206

JEO USA, INC. WEST OFFICE
5653 Stoneridge Drive Suite
#110 Pleasanton, CA. 94588
Tel: (925) 737-1740
Fax: (925) 737-1749

VENEZUELA
MITSUBISHI VENEZOLANA C. A.
Avenida Francisco de Mirande Los Palos Grandes,
Carecas, Venezuela
Telephone: (212) 209-7402
Facsimile: (212) 209-7496

(Ser. No. 119)

No. 01501F336C Printed in Japan, Kp